Galactic Gas Flows from Halo to Disk: Kinematics and Tomography in the Milky Way's Low-Velocity Circumgalactic Medium

Hannah V. Bish

A dissertation
submitted in partial fulfillment of the
requirements for the degree of

Doctor of Philosophy

University of Washington

2022

Reading Committee:

Jessica Werk, Chair

Mario Jurić

Matthew McQuinn

Program Authorized to Offer Degree:

Astronomy

University of Washington

Abstract

Galactic Gas Flows from Halo to Disk:
Kinematics and Tomography in the Milky Way's
Low-Velocity Circumgalactic Medium

Hannah V. Bish

Chair of the Supervisory Committee:
Professor Jessica Werk
Astronomy

The evolution of galaxies is closely linked to the exchange of gas between their disk and the circumgalactic medium (CGM) – the massive, extended, diffuse halo of gas in which galaxies are embedded. Recent advances in high-resolution spectroscopy have enabled observers to firmly establish the key role played by the CGM in the life cycle of galaxies: it is the hiding place of at least half of all galactic baryons, acting as a massive reservoir that replenishes the supply of fuel for star formation via gas accretion onto the disk. However, this nearly-invisible halo gas is challenging to observe, and we are still missing a complete picture of its distribution, kinematics, and multiphase structure. In this thesis, I use the Milky Way as a case study to shed light on the nature of cool and warm CGM gas flows, taking advantage of the abundance of quasar and stellar sightlines which probe the Galactic CGM. In particular, I focus on the behavior of low-velocity gas, which is often overlooked by CGM studies because it is difficult to measure in isolation. I show that local CGM gas is predominantly inflowing, place constraints on the inflowing cloud sizes, and determine that these clouds lie close to the disk. I use a novel spectral differencing technique to correct for foreground absorption along sightlines through the Galactic halo, and present the first unobscured measurements of the Milky Way's extended low-velocity CGM. The results demonstrate that either the warm CGM does not have a spherical morphology, as is often assumed for star-forming galaxies, or

that the Milky Way is not a typical star-forming galaxy. Finally, I find that inflow velocities are higher for warmer gas, suggesting a picture in which warm accreting gas slows down and cools as it approaches the disk. The mass accretion rates of these inflows indicate that a significant fraction of star-formation fuel may accrete onto the disk at low velocities.

TABLE OF CONTENTS

LIST OF FIGURES

LIST OF TABLES

ACKNOWLEDGMENTS

This dissertation is a reflection not only of my own work, but also of all the people around me who have provided their mentorship, camaraderie, support, and encouragement along the way. Words are inadequate to express my deep gratitude for all these people have given me.

To my advisor, Jess Werk: thank you for being a wonderful mentor and source of support for me during my time in grad school. I've grown as both a scientist and a person through our work together, and I feel fortunate that I've had the chance to work with you. I could always count on your encouragement to push through the most challenging or confusing parts of a project, your enthusiasm for the science, and your hands-on guidance. You've been my cheerleader and my advocate at times when I really needed one, and I owe so much to your support and understanding.

I'd also like to thank the coauthors and collaborators whose ideas and advice have been valuable to my growth as a scientist. I'm grateful to Xavier Prochaska, John O'Meara, Enrico DiTeodoro, and Alis Deason for improving the quality of my papers and helping me reach a deeper understanding of my science. Thank you to Kate Rubin for your positivity and encouragement, Mary Putman for the science chats and insightful feedback, and Yong Zheng for your encouraging and instructive guidance throughout the span of my graduate career. Thanks to Josh Peek, whose boundless enthusiasm never fails to rub off on me. I look forward to working with you next year. And of course, I would not be in graduate school in the first place if not for the guidance of my mentors during my time as an undergrad. Charles Liu, thank you for seeing something in me during that public observing night and believing in me enough to give me a research internship on the spot. Thanks also to Viviana Acquaviva for being a model of a scientist that I wanted to emulate, and for the humor and

warmth that made me feel more at home in our research group. And special thanks to Eric Gawiser, my undergraduate research mentor at Rutgers University, for pushing me out of my comfort zone and having confidence that I would succeed there. I learned so much from you, and you are the reason I believed I could apply to graduate school. The opportunities you gave me to develop and learn as a young scientist played an important role in my success.

Thanks to my mentoring committee – Jess Werk, Mario Jurić, and Andy Connelly – for the advice and encouragement you provided during my final push of grad school. Thanks also to Jess Werk, Mario Jurić, Matt McQuinn, and GSRs Ellen Covey and Jerry Seidler for serving on my thesis committee. And thank you to my own mentees and students for reminding me why I wanted to be an astronomer in the first place. It has been my great joy to see you blossom into accomplished scientists.

I've been so very lucky to find myself among the wonderful community of astronomy graduate students at the University of Washington. Thank you for learning, venting, and celebrating with me, for your collaboration on coursework, the long study sessions, the stress relief provided by many raucous foosball games, W(h)ine Times and drunken planetarium karaoke nights, and the countless impromptu chats in your offices. I'm so grateful for all of you who have helped make this department feel like a place where we welcome and support each other. And especially, most deeply, thank you to those among you who have become my dear friends. I appreciate you all so much and I have no idea how I would have made it through this time without you. I'm especially indebted to the grads in the Old Fogey crew – Diana, Nicole, and Trevor – for being my second family these last few years, especially during the pandemic. Diana Windemuth, your unfailing support and friendship have been so meaningful to me, and I am full of admiration for your wisdom and thoughtfulness. Thank you for being there to drive me to the hospital in the middle of the night, keeping me sane through the pandemic, being the best listener I know, and for 880 days of meditation in a row (and counting). Nicole Sanchez, I can't tell you how grateful I am to you for bringing

so much friendship and light into my life. Thank you for inspiring me with your endless ambition and energy, showing me what it means to be both soft and strong, being my support and venting buddy during postdoc apps and thesis writing, and bringing us together in various ways to celebrate the good things in life. Trevor Dorn-Wallenstein, thank you for your solidarity, your quiet generosity, and all the terrible puns. I also want to thank my longtime officemates, Dave Fleming and Margaret Lazzarini. Dave, you made my time here lighter with your good cheer and patience as we slogged away on all those grueling problem sets. Margaret, it's been such fun to navigate this time with you and watch you achieve the success you have earned. Thank you for all the good life chats and always being a warm and happy presence in our office. Thanks to Jake Lustig-Yaeger, Dave Fleming, and Kolby Weisenburger, the other grads in my cohort, for experiencing the trial by fire of first year alongside me, and for the trauma bonding of all those hours in the reading room studying for the dreaded written qual. Steven Stetzler, thank you for your presence, friendship, humor, and our many long conversations about nothing and everything, all of which have brought me immeasurable comfort. You have made me feel so much less alone over the last five years, and I can't imagine grad school without you. Matt Wilde, thanks for your unwaveringly positive and friendly energy, always letting me nap on your office couch, convincing me to come out and play when I needed a break, and understanding my struggles in those dark moments. John Ruan, thanks for all the sage advice, our painting and creativity get-togethers, and the memorable Montreal visits. Debby Tran, thank you for our long heartfelt talks, your deep sense of justice, always being there to lend a hand, and all the citrus fruit. Brianna McKay, thank you for your sisterhood, the relaxing painting sessions, and for being there to commiserate with me during our time as the Bad Back Babes. Nell Byler, thank you for taking an interest in connecting with me when I was just a baby grad, and for touching me with your kindness and understanding. You didn't know it at the time, but that meant everything to me. And thank you to Grace Telford, Kathryn Neugent, Iryna Butsky, Myles McKay, and Phoebe Upton Sanderbeck for your friendship, collaboration, and support.

Lastly, thank you to my family, especially my parents, Tom Bish and Deborah Lasher. You have always fostered my curiosity, made my education a priority, and patiently supported me no matter what direction my path took. Thank you for dropping your lives in the middle of a global pandemic and driving across the country to help me with my health so that I could finish my degree. Thank you for all the things you've done over the years to help me get here; there are far too many to name. I'm incredibly fortunate to have the unconditional love and support that I do.

The research in this dissertation was conducted at the University of Washington in Seattle, which sits on the unceded ancestral land of the Duwamish People (Dkhw Duw'Absh) past and present. I honor with gratitude the Duwamish Tribe and the land itself. Additionally, as part of my dissertation work I have had the privilege of using the Keck telescope at Mauna Kea Observatory, which is on the stolen land of the Kānaka ʻŌiwi people. I stand in solidarity with the Pu'uhonua o Pu'uhuluhulu Maunakea in their effort to preserve this sacred space for native Hawaiʻians.

Chapter 1

INTRODUCTION

Imagine a galaxy in your mind's eye. You might see majestic spiral arms dotted with innumerable stars, the shadows of intricate dust lanes, or a bright core illuminating the center. But the part of galaxies that is visible to us does not tell the story. The disk of a star-forming galaxy comprises just a fraction of its total mass – the rest sits in a diffuse, nearly-invisible halo that is at least as massive as the disk and occupies at least 1000 times as much volume. This halo and its contents are known as the circumgalactic medium (CGM). Over the past decade or so, astronomers have firmly established that this elusive hidden component of galaxies plays a central role in galactic evolution over cosmic time: it serves as a massive reservoir of gas that regulates and replenishes the supply of fuel for star formation in the disk, allowing galaxies to maintain star formation for billions of years rather than fizzling out in just a few million. The physics which governs the exchange of gas between the halo and disk is complex, and so too is the structure and kinematics of that gas. While we can be certain that these gas flows play an important role in shaping galaxies, we have extremely limited ability to observe them, which leaves us with only a murky understanding of how this occurs. Crystallizing a comprehensive interpretation of the physical properties of gas flows in the CGM remains one of the biggest challenges in astronomy today. To this end, the aim of the work I present here is to address this challenge by strategically observing and characterizing these gas flows so that we may understand their contents, distribution, kinematics, origin, fate, and their significant influence on galaxy evolution over cosmic time.

1.1 The Galactic Fountain

Galaxies like the Milky Way grow via complex processes balancing the supply, consumption, and removal of gas in star-forming regions. Observations of the baryons involved in this cycle are consistent with gas moving in a "galactic fountain" (Bregman, 1980), in which stellar winds, supernovae, and/or AGN continually drive gas into the galactic halo, where it either escapes the galaxy entirely or cools, condenses, and falls back to the disk to trigger new star formation (see Figure 1.1; Shapiro & Field, 1976; Savage & Sembach, 1994; Sembach et al.,

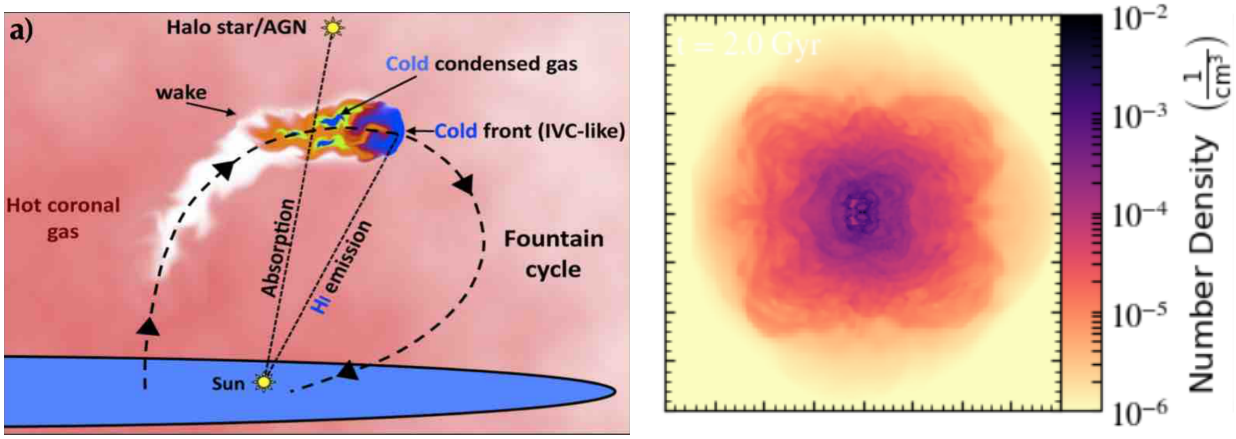

Figure 1.1: The galactic fountain model. *Left:* A cartoon from Fraternali (2017) illustrating the cycle of galactic fountain gas. Stellar winds, supernovae, and/or AGN continually drive gas into the galactic halo, where it cools, condenses, and falls back to the disk to trigger new star formation. These clouds of halo gas can be observed directly in HI 21-cm emission, or in absorption along a line of sight to a bright background source. *Right:* The simulated CGM of a Milky Way-like galaxy from Li & Tonnesen (2020). The image shows a 800 kpc-wide slice of the galaxy, with the galactic disk in the x-direction. The galaxy ejects plumes of gas which extend out to, and sometimes beyond, the virial radius of the galaxy.

2003; Bordoloi et al., 2011; Marinacci et al., 2011; Armillotta et al., 2016; Gronke & Peng Oh, 2018). As a result, the contents of a galaxy's gaseous halo and the star formation occurring within the disk are closely interdependent. The continual cycling of baryons between the halo and disk plays a crucial role in regulating the supply of fuel for star formation and consequently has a major influence on galaxy evolution.

The varied and complex dynamic mechanisms which drive Galactic baryon cycling are not fully understood, but may be key to answering long-standing questions about how galaxies sustain star formation, why they become quenched, and the baryons and metals that are 'missing' from the disks of star-forming galaxies (Tumlinson et al., 2017). The relative contributions of star-formation driven winds in the disk, a biconical wind from Galactic center (Su et al., 2010), tidal stripping of satellites, and inflowing gas from the intergalactic medium (Brooks et al., 2009) are still widely debated (Bordoloi et al., 2014a; Fox et al., 2015b).

The timescales on which this material accretes, and the phase structure of the clouds themselves, are two of the physical properties that can best constrain models of the galactic fountain. However, detecting and characterizing these galactic fountain gas flows is not a trivial task.

1.2 Observational Methods

The most significant barrier to our understanding of the CGM is the difficulty of observing it. CGM gas can be anywhere from ten to a million times less dense than the ISM (Stocke et al., 2013; Werk et al., 2014; Stern et al., 2016) and is therefore extremely challenging to detect for galaxies at all epochs (Stocke et al., 2013; Werk et al., 2014). Early evidence for its existence emerged when Münch & Zirin (1961) identified NaI and CaII absorption in the spectra of high-latitude Milky Way stars and interpreted these signatures as originating from extraplanar gas. In the following years, other astronomers began using similar spectroscopic techniques to detect halo gas in other galaxies (e.g., Bahcall & Spitzer, 1969; Bergeron, 1986; Steidel & Sargent, 1992; Lanzetta et al., 1995; Chen et al., 1998).

Only the highest-density clouds can be observed directly in emission with deep HI-21cm maps. Ionized metals – key tracers of star formation – are not dense enough to be observed in emission. Instead, they are typically detected in absorption along lines of sight to background sources like quasars or bright halo stars. Absorption spectra encode a wealth of information about CGM gas, including kinematics, temperature, abundances, density structure and distribution. Such measurements provide clues about the origin and ultimate fate of CGM gas, and can help to distinguish between models of baryon cycling in galaxies. One thing absorption measurements do not provide, however, is information about the distance of the gas from the host galaxy – a barrier which I attempt to circumvent with techniques presented in Chapters 2 and 3 of this dissertation.

Within the last decade or so, significant advances have been made with improved spectral analysis techniques and the installation of the Cosmic Origins Spectrograph (COS) on the Hubble Space Telescope (HST), which marked a thirtyfold increase in sensitivity to diffuse

gas compared existing UV instruments (Osterman et al., 2010). Groundbreaking work with COS has allowed astronomers to piece together most of what we currently understand about the CGM's role in galaxy evolution. In this dissertation I have also made use of the Keck HIRES optical spectrograph, which provides exquisite resolution at optical wavelengths, and HI 21-cm surveys created using several different radio telescopes. Observations with spectrographs like COS and Keck rely on the use of bright background sources to identify absorption features from foreground gas. These background sources may be quasars observed through the CGM of foreground galaxies (e.g., Werk et al., 2013; Zheng et al., 2019) or halo stars behind Milky Way CGM gas (e.g., Savage & Wakker, 2009; Lehner & Howk, 2011; Fox et al., 2015b). Additionally, the "down-the-barrel" technique measures a galaxy's CGM in absorption using its own starlight as a background source, and has been used to study outflows and accretion (e.g., Rubin et al., 2012; Heckman et al., 2015).

Gas absorption surveys are often conducted with UV spectrographs because this part of the spectrum is particularly rich in information. The UV regime encompasses the absorption features of many ions tracing a range of temperatures, which is crucial for understanding such a dynamic medium which exists simultaneously in multiple phases. In this dissertation, unless otherwise stated, I will refer to ions tracing gas at $T \lesssim 10^4$ K as cool, $T \sim 10^4 - 10^5$ K as warm, $T \sim 10^5 - 10^6$ K as warm-hot, and $T \gtrsim 10^6$ K as hot. In my investigations of CGM gas I look at a range of ions including H I , H II , Na I , Ca II , S II , C II* ,Ni II , Si IV , C IV , and N V . The C IV doublet in particular is a useful probe of warm ionized gas in galaxy halos because of its strong oscillator strength (Savage & Wakker, 2009) and high covering fraction in the CGM of external galaxies (Keeney et al., 2013; Liang & Chen, 2014).

1.3 The Milky Way

Extragalactic absorption-line studies are useful for investigating average global properties of the CGM, but the limited availability of quasar sightlines means we can rarely make more than one or two measurements within a single galaxy halo outside the Local Group. Studies of the Milky Way in particular provide the unique advantage of probing a single halo with

densely sampled sightlines and distance information, providing a 3-dimensional empirical picture of the CGM. Because of our vantage point and proximity to this gas, we can glean more information about gas flows in the Milky Way than in any other galaxy in the universe, making the Milky Way an ideal case study for understanding the CGM in all star-forming galaxies.

In the Milky Way, observations of CGM gas reveal a complex structure and distribution which can be explained by various physical models. On the largest scales, the CGM may be distributed spherically with a steeply declining density profile (e.g. Liang & Chen 2014; Werk et al. 2014); it may form a thick, rotating, toroidal structure (e.g. Stewart et al. 2011; Bregman et al. 2018); or it may be composed of large shocked sheets of material flowing through the halo (McQuinn & Werk, 2018). The Northern and Southern Galactic skies are quite different in their known CGM components, which may indicate an overall asymmetry (Putman et al., 2012; Bordoloi et al., 2017). Additionally, smaller-scale structures, such as clouds and thin filaments are known to populate the CGM (e.g. Ben Bekhti et al., 2009; Saul et al., 2012; Stocke et al., 2013; McCourt et al., 2015; Stern et al., 2016; Bish et al., 2019).

1.4 The Disk-Halo Interface

Any gas flowing into the galaxy must pass through both the CGM and the disk-halo interface, a transitional boundary layer where halo gas is integrated into the disk as it cools (Norman & Ikeuchi, 1989; Ford et al., 2010; Putman et al., 2012), potentially colliding with hot gas that is being forcefully ejected from the galaxy by stellar winds and supernovae (Joung & Mac Low, 2006; Hill et al., 2012; Putman et al., 2012; Creasey et al., 2013; Li et al., 2017). The disk-halo interface, also referred to as extraplanar gas, is rich in information about material which has cycled through the CGM and presents an opportunity to observe gas in the final stages of accretion as it fragments, mixes with the disk and interacts with outflowing material. The properties of such gas remain poorly constrained, but a clear picture of the content, kinematics, and thermodynamics of inflowing and outflowing gas is essential for understanding its origin, the link between star formation and the CGM, and by extension galaxy evolution as a whole.

Gas at the disk-halo interface is complex and dynamic. It experiences changes in density, ionization state, and velocity as it moves in and out of the disk and interacts with ambient material. In general the disk-halo interface exhibits decreasing rotational velocity as z-height increases, known as "lag," and shows a clear temperature gradient that changes from cool near the disk to hot in the lower halo (Putman et al., 2012). Gas observed close to the disk of the Milky Way sits mostly in a dense, cold layer of HI, ranging in thickness from < 100 pc near Galactic center, to $\sim$1 kpc near the Galactic warp, to > 6 kpc in the outermost reaches of the disk (Dickey & Lockman, 1990; Levine et al., 2006). At higher z-heights of $\sim$1-2 kpc, this cool ($T \lesssim 10^4$ K) layer gives way to a more diffuse, warm ($T \sim 10^4$ K) component of inhomogeneous ionized gas called the Reynolds Layer, or warm ionized medium (WIM), which has been observed in Hα and a number of other emission and absorption lines (Reynolds, 1993; Haffner et al., 2003; Gaensler et al., 2008; Savage & Wakker, 2009). Above the WIM, even more diffuse, higher temperature warm-hot ($T \sim 10^5$ K) and hot ($T \gtrsim 10^5$ K) gas has been detected in absorption extending into the Galactic halo out to $\sim$3-5 kpc (Savage & Wakker, 2009; Sembach & Savage, 1992; Shull & Slavin, 1994; Miller & Bregman, 2013; Miller & Bregman, 2015).

1.4.1 HVCs and IVCs

In the Milky Way, full-sky HI 21-cm emission maps reveal a population of high-velocity clouds (HVCs; $v > 90$ km/s relative to the local standard of rest) in the halo at typical distances of 5-15 kpc (Wakker & van Woerden, 1997; Wakker et al., 2007; Wakker et al., 2008; Thom et al., 2006, 2008; Lehner et al., 2022), and intermediate-velocity clouds (IVCs; $25 < v < 90$ km/s) out to $\sim$3 kpc (Kuntz & Danly, 1996; Wakker, 2001; Smoker et al., 2011). Both HVCs and IVCs are well-studied, and have been defined and grouped into complexes using HI 21-cm emission data (Wakker & van Woerden, 1991; Wakker et al., 2007; Wakker et al., 2008; Westmeier, 2018). Neutral, weakly- and highly-ionized gas associated with these clouds has also been detected in absorption along sightlines to quasars (Murphy et al., 1995; Sembach et al., 2003; Shull et al., 2009; Ben Bekhti et al., 2012; Lehner et al., 2012; Richter,

2017; Clark et al., 2022) and halo stars (Lehner & Howk, 2010; Lehner & Howk, 2011; Bish et al., 2019; Werk et al., 2019; Lehner et al., 2022).

HVCs are found farthest from the disk. These complexes of neutral and ionized gas extend across 65-90% of the sky (Fox et al., 2006; Collins et al., 2009; Shull et al., 2009; Lehner et al., 2012; Richter, 2017), but likely constitute only a small fraction of the Milky Way's total halo mass (Putman et al., 2012). The largest HVCs include the Magellanic System, Complex C, and Complex A. IVCs are found closer to the disk at z-heights of $\sim 0.5 - 3$ kpc (Kuntz & Danly, 1996; Wakker, 2001; Smoker et al., 2011). HVCs have lower metallicities of 0.1–1.0 $Z_{\odot}$ and velocities inconsistent with Galactic rotation, and are therefore often assumed to have an origin external to the disk (Putman et al., 2012). Some evidence suggests they may form from cooling CGM gas (Thom et al., 2006; Peek et al., 2007).

IVCs are found at predominantly negative velocities (Wakker, 2001), and like high-velocity clouds in the halo, their gas is multi-phase (Albert & Danly, 2004; Richter, 2017; Lehner & Howk, 2011; Fox et al., 2014). They are thought to contain material that once originated in the Galaxy's disk because their metallicities are consistent with that of Milky Way ISM gas, and because ISM simulations find that IVC morphology and kinematics are reproduced by ISM ejecta (Bregman, 1980; de Avillez, 2000; Ford et al., 2010; Richter, 2017).

1.5 Science Drivers

This dissertation aims to address the following science questions:

1.5.1 What are the contents and morphology of the CGM?

In order to understand how CGM gas flows are connected to the broader context of galaxy evolution, we must first be able to answer the fundamental question of what its contents are, and what form they take. While order-of-magnitude estimates can be made as to the total mass and metal content of the CGM, a detailed picture of its contents remains elusive because of the limited spatial information provided by individual lines of sight which probe gas in absorption. The morphology of ionized gas clouds and their spatial and kinematic

alignment with neutral gas clouds in the CGM is still unclear. The contents and spatial extent of this gas can ultimately point to its origin and the dominant physical mechanisms which propel the galactic fountain.

1.5.2 How do galaxies get their fuel for star formation?

Star-forming galaxies do not have nearly enough fuel in their ISM to sustain star formation on long timescales, and much of galaxies' star-forming fuel must come from elsewhere (Lehner & Howk, 2011). It is not yet clear how much of this additional fuel originates from fountain flows close to the disk ($R < 10$ kpc), from infalling CGM gas at larger radii ($R > 10$ kpc), or from outside galaxies via the intergalactic medium ($R > R_{vir}$).

1.5.3 How do CGM inflows shape the course of galaxy evolution?

CGM properties are unambiguously tied to the sizes and star-formation histories of galaxies (Tumlinson et al., 2011; Borthakur et al., 2015; Wilde et al., 2021), but how does this relationship drive galaxy evolution? If CGM flows are instrumental in triggering star formation, then the evolutionary fate of galaxies likely rests on the regularity with which gas feeds the disk from the CGM. Sub-L* galaxies tend to have extended, bursty star-formation histories, while L* galaxies typically have more constant levels of star formation, suggesting their divergent evolutionary path may be due to differences in the availability of fuel for star formation.

1.5.4 How are metals recycled into new stars?

The CGM contains a significant fraction of the metals "missing" from galaxies (Tumlinson et al., 2011), but details of the feedback mechanisms transporting metals to and from galactic disks are still not fully understood. Are sources of star-formation fuel dominated more by pristine gas from the intergalactic medium, or by metal-enriched gas recycled from the disk? If enriched inflows do precipitate star formation, are the metals incorporated into those stars or do they simply enrich the surrounding ISM?

1.6 Dissertation Outline

This dissertation covers three distinct yet closely-related projects addressing open questions about the nature of CGM gas flows within the Milky Way's halo and disk-halo interface. In this work, I capitalize on observations of Milky Way halo gas to constrain its properties, examining the 3-D spatial distribution, structure, and kinematics of both ionized and neutral gas, with the ultimate goal of discerning the prevalence and role of metals and gas flows in the galactic fountain.

In chapter 2, I use background stars at varying distances in the Milky Way's halo to create a 3-dimensional map of low-ionization gas flows (tomography) at the Milky Way's local disk-halo interface. This 3-dimensional spatial and kinematic information is typically not available because distances cannot be obtained from individual absorption spectra. I use these maps to constrain typical cloud sizes and the distance of the gas from the disk, and examine a velocity gradient as evidence for a galactic fountain.

In chapter 3, I apply a novel spectroscopic differencing technique, which builds on the 3-dimensional tomography approach used in chapter 2 by pairing halo star and quasar sightlines at small angular separation in order to subtract out foreground absorption. This method can isolate low-velocity halo gas which is normally badly blended with foreground disk gas, and allows me to make the first isolated measurements of the Milky Way's extended CGM. The resulting column density measurements of warm-hot gas do not align with predictions of simulations and observations of external galaxies, and I discuss the implications of this surprising finding for the morphology of the Milky Way's CGM.

In chapter 4, I follow up on the results described in chapter 3 by developing kinematic models to test various CGM morphologies that might explain the surprising observational results. I also compare these models with observations of gas absorption tracing a range of temperatures and discover that accretion velocities differ as a function of ionization energy – a proxy for temperature. I consider what this differential accretion means for our physical understanding of how gas in the CGM is transferred to the disk.

Chapter 2

TOMOGRAPHY AND KINEMATICS AT THE MILKY WAY'S DISK-HALO INTERFACE

Portions of this chapter were originally published in collaboration with Jessica K. Werk, J. Xavier Prochaska, Kate H.R. Rubin, Yong Zheng, John M. O'Meara, and Alis J. Deason in the September 2019 edition of the Astrophysical Journal (Bish et al., 2019, ApJ*, Vol. 906, 120; 2021 © American Astronomical Society, DOI: 10.3847/1538-4357/abccca), and are reproduced below with the permission of the American Astronomical Society.*

Chapter Summary

We present a novel absorption line survey using 54 blue horizontal branch stars (BHBs) in the Milky Way halo as background sources for detecting gas flows at the disk-halo interface. Distance measurements to high-latitude ($b > 60°$) background stars at 3.1 - 13.4 kpc, combined with unprecedented spatial sampling and spectral resolution, allow us to examine the 3-dimensional spatial distribution and kinematics of gas flows near the disk. We detect absorption signatures of extraplanar CaII and NaI in Keck HIRES spectra and find that their column densities exhibit no trend with distance to the background sources, indicating that these clouds lie within 3.1 kpc of the disk. We calculate covering fractions of $f_{\rm CaII} = 63\%$, $f_{\rm NaI} = 26\%$, and $f_{\rm HI} = 52\%$, consistent with a picture of the CGM that includes multi-phase clouds containing small clumps of cool gas within hotter, more diffuse gas. Our measurements constrain the scale of any substructure within these cool clouds to < 0.5 kpc. CaII and NaI absorption features exhibit an intermediate-velocity (IV) component inflowing at velocities of -75 km/s $< v < -25$ km/s relative to the local standard of rest, consistent with previously-studied HI structures in this region. We report the new detection of an inflow velocity gradient $\Delta v_z \sim 6 - 9$ km/s/kpc across the Galactic plane. These findings place constraints on the physical and kinematic properties of CGM gas flows through the disk-halo interface, and support a galactic fountain model in which cold gas rains back onto the disk.

2.1 Introduction

Galaxies like the Milky Way grow via complex processes balancing the supply, consumption, and removal of gas in star-forming regions. Observations of the baryons involved in this cycle are consistent with gas moving in a "galactic fountain" (Bregman, 1980), in which hot gas is ejected from the disk via supernovae, stellar winds, and/or AGN, then cools and rains back down onto the disk to trigger new star formation (Shapiro & Field, 1976; Savage & Sembach, 1994; Sembach et al., 2003). This continual cycling of baryons between the halo and disk plays a crucial role in regulating the supply of fuel for star formation and consequently has a major influence on galaxy evolution.

The varied and complex dynamic mechanisms which drive Galactic baryon cycling are not fully understood, but may be key to answering long-standing questions about how galaxies sustain star formation, why they become quenched, and the baryons and metals that are 'missing' from the disks of star-forming galaxies (Tumlinson et al., 2017). The relative contributions of star-formation driven winds in the disk, a biconical wind from Galactic center (Su et al., 2010), tidal stripping of satellites, and inflowing gas from the intergalactic medium (Brooks et al., 2009) are still widely debated (Bordoloi et al., 2014a; Fox et al., 2015b).

The diffuse halo extending from the roughly-defined boundary of a galaxy's disk out to its virial radius – the circumgalactic medium (CGM) – is host to the galactic fountain and serves as a massive reservoir of gas ($> 10^{10}$M$_\odot$ for L^* galaxies) (Werk et al., 2014; Prochaska et al., 2017; Stern et al., 2016; Stocke et al., 2013). However, observations of the CGM are challenging because the gas it contains is approximately a million times less dense than the ISM and therefore difficult to detect in emission for single L^* Milky Way-like galaxies at all epochs (Stocke et al., 2013; Werk et al., 2014). Early evidence for its existence emerged when Münch & Zirin (1961) identified NaI and CaII absorption in the spectra of high-latitude Milky Way stars as a signature of extraplanar gas.

Subsequent work identified halo gas absorption in external galaxies using quasars as background sources (Bahcall & Spitzer, 1969; Bergeron, 1986). More recently, deep HI-21cm observations of gas at the disk-halo interface of both the Milky Way and other external, edge-on spiral galaxies have found a so-called halo lag (Putman et al., 2012, e.g.). The approximate rate of halo gas rotation decreases with z-height, with a typical velocity drop-off of $15 - 30$ km/s/kpc (Fraternali et al., 2002; Sancisi et al., 2008; Heald et al., 2011, e.g.). This observed halo lag has been offered as evidence of an infalling gaseous component of the disk-halo interface (Fraternali & Binney, 2006).

Gas at the disk-halo interface is of particular interest because of the rich physical information it contains about material which has cycled through the CGM. Constraints on the content, kinematics, and spatial extent of this material can ultimately point to its origin, but direct detection via emission is possible only for the densest material in the Milky Way halo. Full-sky HI 21-cm emission maps reveal a population of neutral intermediate-velocity clouds (IVCs, $25 < |v| < 90$ km/s relative to the local standard of rest) at heights of $\sim$0.5-3 kpc above the disk (Kuntz & Danly, 1996; Wakker, 2001; Smoker et al., 2011). IVCs are found at predominantly negative velocities (Wakker, 2001), and like high-velocity clouds in the halo, their gas is multi-phase (Albert & Danly, 2004; Richter, 2017; Lehner & Howk, 2011; Fox et al., 2014). They are thought to contain material that once originated in the Galaxy's disk because their metallicities are consistent with that of Milky Way ISM gas, and because ISM simulations find that IVC morphology and kinematics are reproduced by ISM ejecta (Bregman, 1980; de Avillez, 2000; Ford et al., 2010; Richter, 2017).

The timescales on which this material accretes, and the phase structure of the clouds themselves, are two of the physical properties that can best constrain models of the galactic fountain. However, isolating halo gas from disk gas at the interface is challenging because line-of-sight observations themselves do not provide distance information about the gas, and the two components may overlap partially in velocity space.

Within the last decade, significant advances have been made with improved spectral analysis techniques and the installation of the Cosmic Origins Spectrograph (COS) on the

Hubble Space Telescope, which increased the sensitivity of diffuse gas detections by an order of magnitude (Osterman et al., 2010). Today, the technique most sensitive to low-density gas along individual sightlines uses spectra of background sources to identify absorption features from foreground gas. These background sources may be quasars observed through the CGM of foreground galaxies (e.g., Werk et al., 2013; Zheng et al., 2019) or halo stars behind Milky Way CGM gas (e.g., Savage & Wakker, 2009; Lehner & Howk, 2011; Fox et al., 2015b). Additionally, the "down-the-barrel" technique measures a galaxy's CGM in absorption using its own starlight as a background source, and has been used to study outflows and accretion (e.g., Rubin et al., 2012; Heckman et al., 2015).

We present an absorption-line survey designed to examine the kinematics, spatial extent, and cloud characteristics of gas at the Milky Way's disk-halo interface. We have analyzed CaII ($\lambda\lambda$ 3934, 3969) and NaI ($\lambda\lambda$ 5891, 5897) transitions in absorption along 54 sightlines to blue horizontal branch (BHB) stars with well-constrained heights 3.1 - 13.4 kpc above the disk. Because they are approximate standard candles, BHBs provide distances which we use to describe the 3-D spatial extent of the gas. The sightlines are limited to high Galactic latitudes ($b > 60°$) so that radial velocity measurements place the greatest possible constraints on gas inflow/outflow velocities. The excellent resolution of Keck HIRES spectra and the unprecedented 3-dimensional spatial sampling of this survey allow us to place empirical constraints on the physical and kinematic properties of CGM gas flows through the disk-halo interface.

This chapter is organized as follows: in §2.2, we describe the survey design and observations. In §2.3 we describe our methods for line profile fitting and define subsamples for analysis. In §2.4 we present the column density and velocity measurements of the gas absorbers in this sample. In §2.5 we examine how these measurements can place constraints on cloud size and distribution and the implications of our findings for potential origins of the gas we see. In §2.6 we summarize our findings.

2.2 Observations

2.2.1 Survey Design & Sample Selection

Our absorption line survey uses blue horizontal branch stars in the Milky Way halo (hereafter referred to as BHBs) as background sources to study diffuse foreground gas. BHBs are well-suited for this purpose because they have bright, relatively featureless spectra ideal for absorption-line analysis, and as approximate standard candles they have measured distances to within ±10% (Kinman et al., 1994; Sirko et al., 2004; Clewley & Jarvis, 2006; Xue et al., 2008; Deason et al., 2011). We have taken advantage of these properties to obtain kinematic information and distance constraints for gas along sightlines which probe the disk-halo interface of the Milky Way. We observed 56 out of 83 stars meeting the selection criteria described in this section, and ultimately excluded two from our analysis. Figure 2.3 shows the Galactic coordinates of the sightlines on an all-sky map, along with the approximate boundaries of several large intermediate-velocity HI complexes (van Woerden et al., 2005). A full list of these targets and their properties can be found in Table 2.1.

The sample of background sources was selected from >4,500 BHB stars with accurate distances and velocities in the SDSS SEGUE catalog (Xue et al., 2011). To verify that we are using the best available distance measurements for the BHBs, we checked the SEGUE distances against the Gaia DR2 catalogue. We found that for all but one BHB, SEGUE distances were more precise because the stars are close to or beyond the ∼5 kpc limiting distance for accurate parallax measurement (Luri, X. et al., 2018). Since the distance measurements we use only set an upper limit on the distance to the absorbing gas, and most of the gas likely sits close to the disk at small distances (see §2.4.1), the error on BHB distance measurements does not significantly affect our analysis.

Figure 2.1 shows the distribution of SEGUE BHBs from an edge-on view of the Milky Way. The full set of BHBs in the catalog is marked by small black points, and blue stars show the location of BHBs selected for this study. A subset of these sightlines, shown in yellow, have also been observed with HST COS in the UV and data will be presented in Werk

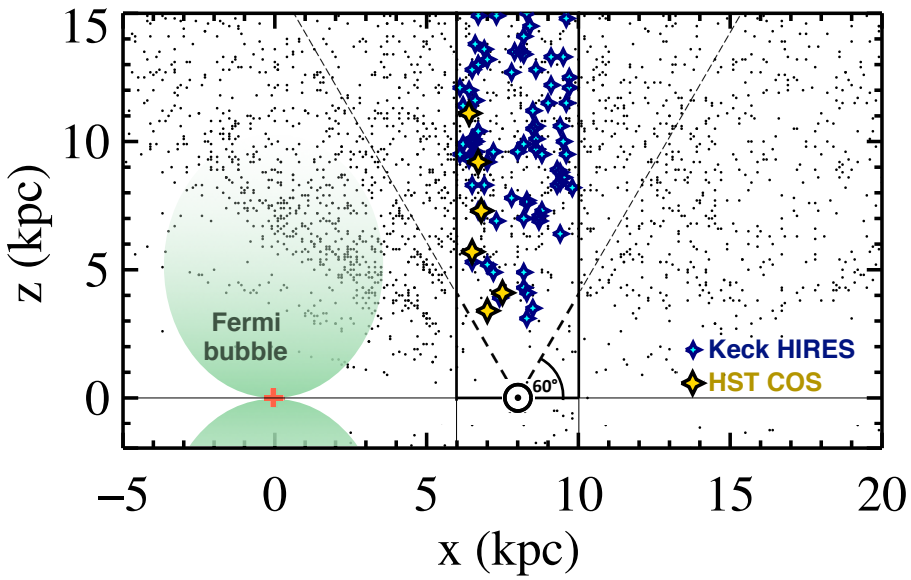

Figure 2.1: SURVEY GEOMETRY. Spatial distribution of BHB stars in the northern Milky Way halo, shown in the x-z projection. The full BHB catalog from SEGUE (Xue et al., 2011) is displayed with black points. Targets observed with Keck HIRES for this study are highlighted with star symbols, and were selected to fall at high Galactic latitudes within a cylinder 2 kpc in radius centered on the Sun. Yellow stars indicate BHBs which have also been observed with HST COS as part of a complementary program to study highly-ionized gas in this regime. The red cross marks the Galactic center, and the Sun is marked by the solar symbol. Green shading indicates the approximate extent of Fermi bubbles formed by winds emanating from the Galactic center (Su et al., 2010). The three targets at $b > 60°$ are included here, but do not appear below the dashed line at $b = 60°$ as viewed from this particular angle.

et al. 2019 (in prep). The Galactic center is indicated with a red cross, and the approximate extent of the Fermi Bubble is shown in green (Su et al., 2010). The Fermi bubble has been probed in absorption by Bordoloi et al. (2017) using halo stars with known distances, and other work has examined the Fermi Bubble as a potential source of recycled gas observed elsewhere in the Milky Way (Fox et al., 2015b; Karim et al., 2018).

This sample meets several selection criteria. First, targets are bright enough to reach S/N $\geq$ 10 with Keck/HIRES in less than $\sim$ 1 hr so that absorption features of interest can be detected. This constraint imposes a g-band magnitude cut of $m_g < 16.5$. Figure 2.2 shows the distribution of g-band magnitudes for background sources in this work and their distances from the Sun. The distance calibrations are dependent on both g magnitude and $(g - r)$ color (Xue et al., 2008). Recently, Lancaster et al. (2018) found that roughly 10%

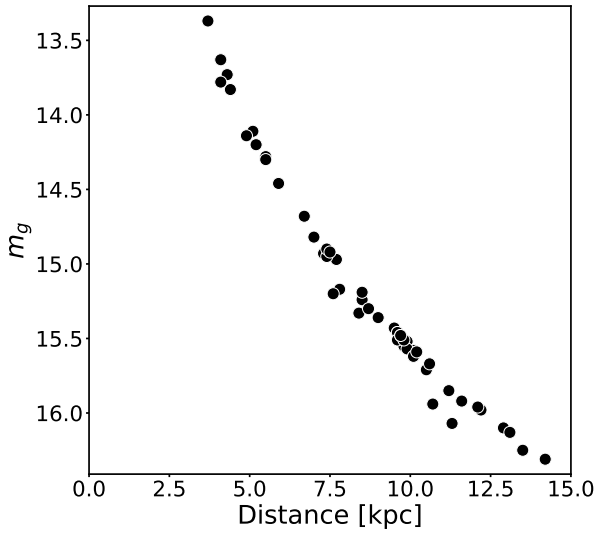

Figure 2.2: BACKGROUND SOURCE MAGNITUDES. The SDSS apparent g-band magnitude of each background source and its distance from the Sun. The sources are blue horizontal branch (BHB) stars, which are approximate standard candles and can be used to constrain the distance to foreground gas along each sightline. Distance calibrations are dependent on both g magnitude and $(g-r)$ color (Xue et al., 2008).

of stars in the SDSS BHB sample were contaminant Blue Straggler stars, which are fainter than BHBs and would lead to overestimated distances. We have applied their color cut to the BHB catalog to remove these contaminants.

Second, we excluded background BHBs with radial velocities -80 km/s $< v_{\rm star} < 0$ km/s so that absorption features of the background star and foreground gas would not overlap. This constraint was determined after an initial pilot study showed that virtually all foreground gas fell within that velocity range (see §2.4.2 for discussion of these results).

To place robust constraints on the kinematics of gas inflows/outflows, we selected high-latitude sightlines so that measured radial velocities will best constrain the motion of this gas. High-latitude sightlines provide a window into the dynamics of extraplanar gas flows because we can examine the component of line-of-sight velocities normal to the disk. The target BHB sightlines lie at Galactic latitudes $b > 60°$, with the exception of three from the initial pilot study at $b = 51.4°, 55.2°, 57.5°$.

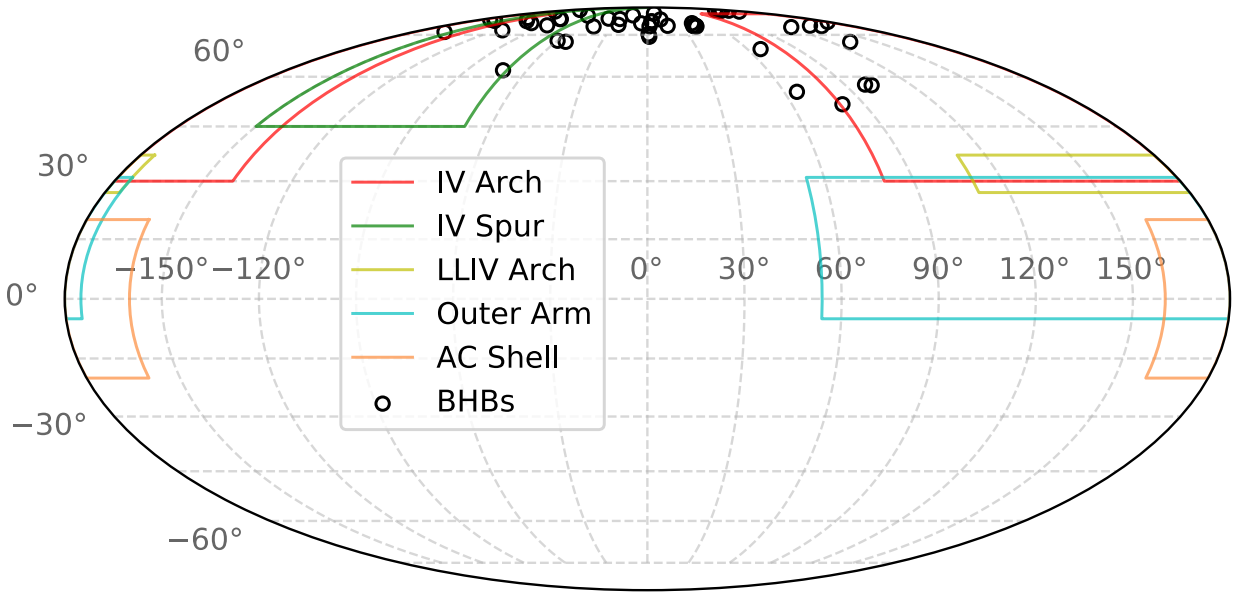

Figure 2.3: BHB SIGHTLINES & NEARBY IVCs. Galactic coordinates of the observed BHB sightlines on an all-sky map, along with the approximate boundaries of several large intermediate-velocity HI complexes (van Woerden et al., 2005). The plane of the Milky Way extends horizontally, with Galactic center at l=0°, b=0°. The sightlines probe the boundaries of the high-latitude IVCs known as the IV Arch and the IV Spur.

Finally, we defined a uniform sampling region in projected x-y space across the disk to allow for comparison of extraplanar gas properties at different heights. Since the disk area spanned by BHBs at $b > 60°$ increases with distance, spatially uniform sampling requires that the radius of this cylinder is limited by the number of available sightlines at small heights above the disk. To achieve this uniform sampling, we chose sightlines which lie within a cylinder 2 kpc in radius, centered on the Sun and extending 15 kpc into the halo (Figure 2.1).

2.2.2 Coordinate System

BHB distance measurements allow us to adopt 3-dimensional coordinates, rather than sky coordinates, to map the distribution of gas. A 3-D coordinate system is useful for studying flows in the frame of the Milky Way and is typical for Milky Way dynamical measurements,

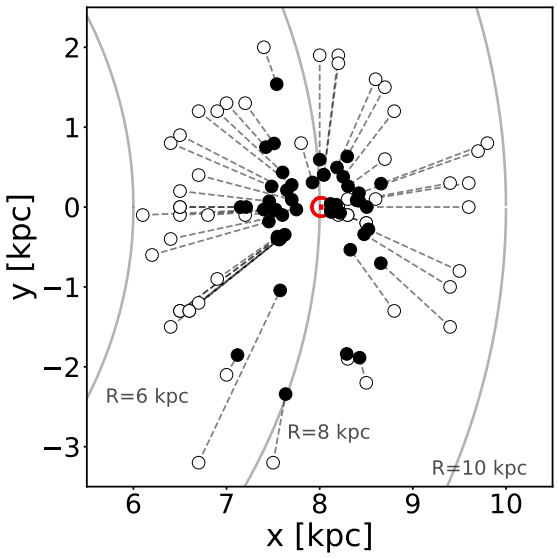

Figure 2.4: Effect of height assumptions on gas coordinates. An illustration of the change in x-y coordinates for hypothetical gas along each sightline when we assume two different distances to the gas. Open circles mark the coordinates of the upper limit on distance set by the background star. Filled circles, connected by a dashed line, show the location of gas along the same sightline assuming a height of z=3 kpc. The red solar symbol marks the position of the Sun, and lines of constant distance from Galactic center are shown in grey.

but is not often used in absorption studies because distance measurements are rarely available or are too imprecise. Throughout this paper we use a Cartesian coordinate system in our discussion of the position, scale and kinematics of gas near the disk. The x-axis extends from Galactic center in the direction of the Sun, y is perpendicular to x in the plane of the disk, and z is perpendicular to the disk such that the system is right-handed, with positive z towards the north Galactic pole. In this reference frame, the Galactic center is at the origin and the Sun lies at $(x,y,z) = (8,0,0)$ kpc. Figure 2.1 shows an edge-on view of the Milky Way in the x-z plane, and Figure 2.4 shows a face-on view of the disk with BHB coordinates projected onto the the x-y plane.

We note that the BHB distance measurements represent an upper limit on the distance to any gas detected along the line of sight. Therefore any distances inferred from spatial maps of gas absorption are upper limits. To illustrate this point, Figure 2.4 provides a visual comparison of the x-y coordinates of gas along each sightline assuming two different distances.

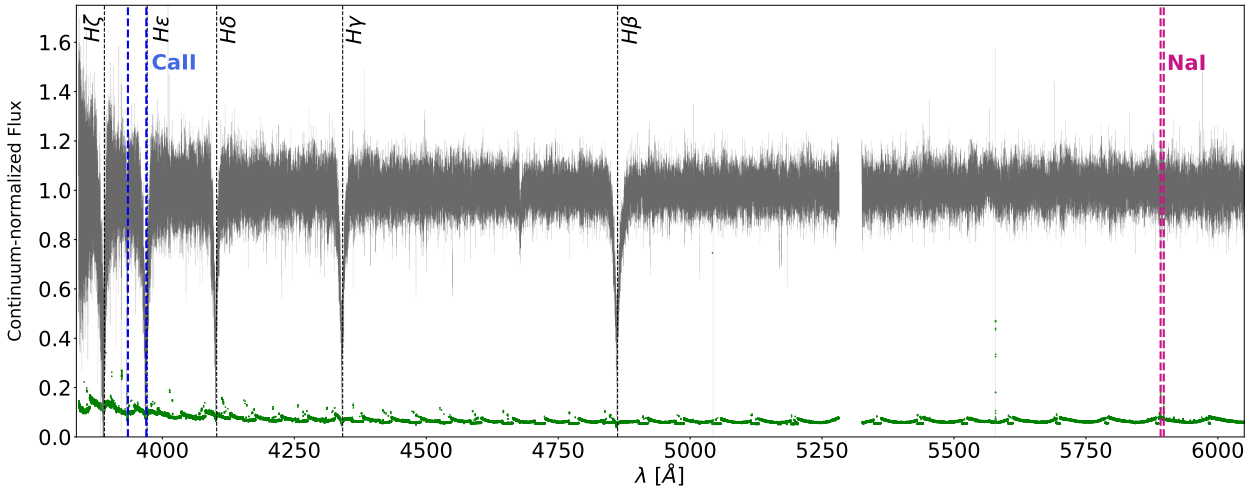

Figure 2.5: Spectrum of BHB used as background source. Keck HIRES spectrum of J1217+2104, a typical metal-poor BHB used as a background source. Flux measurement error is shown in green. Vertical lines mark stellar Balmer absorption features as well as the CaII ($\lambda\lambda$ 3934.8, 3969.6 Å) and NaI ($\lambda\lambda$ 5891.6, 5897.6 Å) absorption doublets used in this work. Note that the CaII 3969.6 line falls within the broad Hϵ feature, and that the continuum was adjusted to account for this feature before fitting the CaII doublet. A CCD chip gap falls at 5282-5326 Å. The jagged profile of the flux error is due to the blaze function of each order, which results in more flux at the center of the order than at the edges.

Coordinates of the upper limit on distance set by the background star are marked by open circles. These are connected by a dashed line to filled circles marking the coordinates of gas along the same line of sight, assuming all gas lies at a height of $z = 3$ kpc (the motivation for making such an assumption is discussed in §2.4.1). Although the disk area covered by this survey changes significantly, the results we present remain qualitatively the same regardless of the distance assumed. For that reason, we show only the coordinates corresponding to the background source in all subsequent plots unless otherwise noted.

2.2.3 Keck HIRES Spectra

At optical wavelengths, the HIRES spectrometer (Vogt et al., 1994) at the W.M. Keck Observatory can detect relatively weak absorption features of neutral and low-ionization species like CaII H+K and NaI D, which trace cool gas ($T \lesssim 10^4 K$) (Münch & Zirin, 1961;

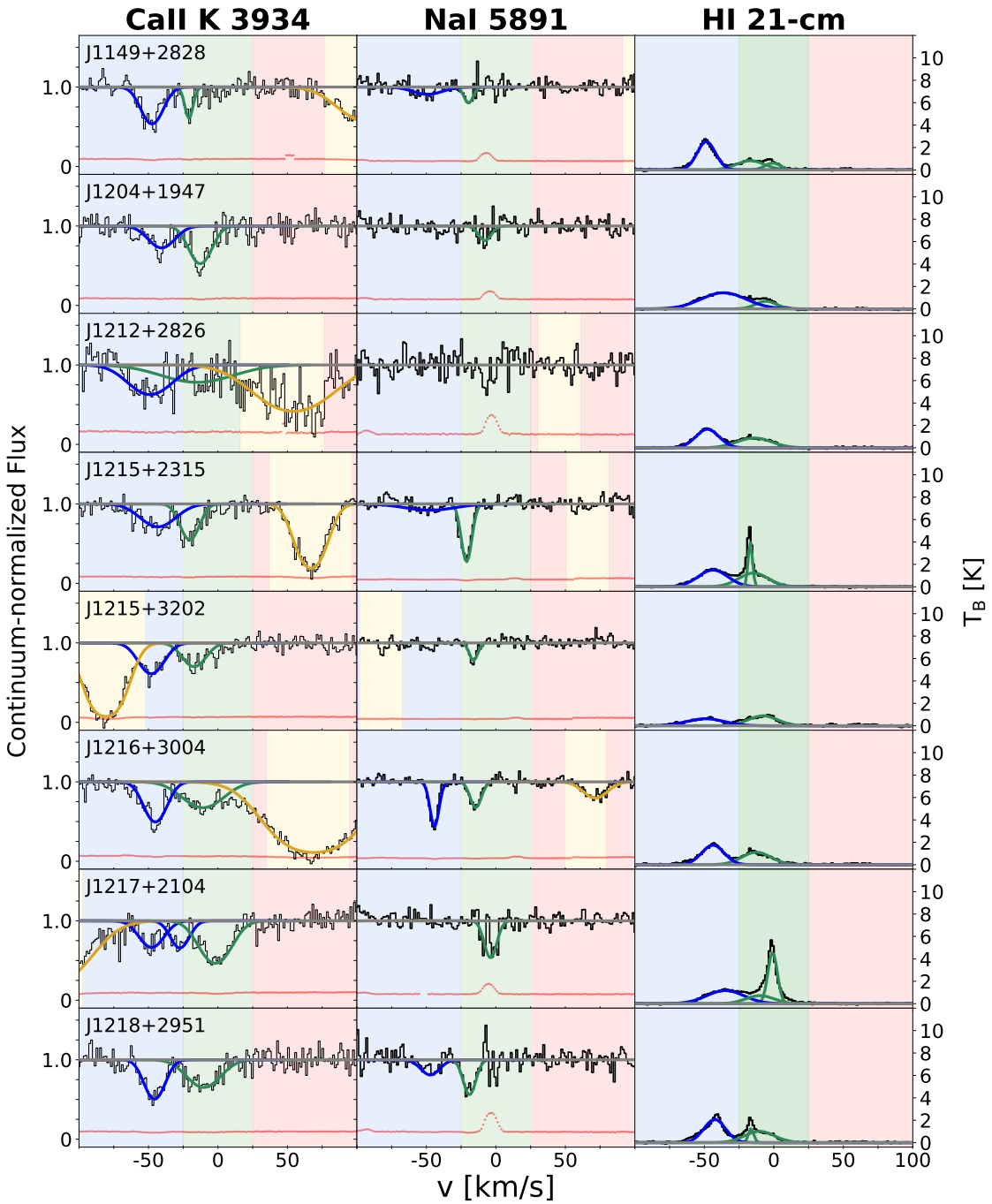

Figure 2.6: Detailed view of absorption features. Examples of the CaII and NaI absorption features marked in Figure 2.5 for several BHB sightlines (columns 1 & 2), and HI 21-cm brightness temperatures measured nearest those sightlines (column 3) from the Effelsberg-Bonn HI Survey (Winkel et al., 2016). Flux measurement errors for CaII and NaI are shown in red. The velocity range and absorption features associated with ISM gas ($|v| < 25$ km/s) are shaded green; otherwise positive velocities are shaded red and negative velocities are shaded blue. Regions near the stellar radial velocity and any associated absorption are highlighted in yellow if they fall within the window of the plot. While the spectra show stellar CaII absorption in some cases, they rarely show stellar NaI absorption. Almost all absorption detected outside the ISM velocity range is blueshifted, indicating a gaseous component moving towards the disk at approximately -75 to -25 km/s. The full set of line profile fits is included in Appendix 2.8.

Spitzer, 1956). Figure 2.5 is an example of a typical BHB spectrum and shows where the CaII and NaI absorption features fall with respect to the broad stellar Balmer lines. Columns 1 & 2 of Figure 2.6 show a more detailed view of the CaII K and NaI D_2 absorption features for selected sightlines. We obtained HIRES spectra for 56 out of 83 total stars which met the criteria outlined above. Two spectra with S/N < 6 were ultimately excluded from the sample because signal-to-noise was too low for reliable line profile fitting.

Observations were made over two runs in March 2016 and February 2017, and the instrument setup was chosen to optimize measurement of the CaII H+K ($\lambda\lambda$ 3934.8, 3969.6 Å) and NaI D ($\lambda\lambda$ 5891.6, 5897.6 Å) doublets. We took a minimum of two exposures for each sightline to allow for cosmic ray correction. Exposure times ranged from 300-1800 seconds, depending on the apparent magnitude of the target, resulting in S/N=6-46 per pixel with a median of 16.2 at wavelengths near the CaII doublet and S/N=9-60 per pixel with a median of 21.5 for the NaI doublet. Typical wavelength coverage was ∼3800-8350 Å, and when possible we adjusted wavelength coverage of each chip so that lines of interest would fall within the overlapping wavelength range detected by both chips. We used the C5 decker, with the image rotator in vertical-angle mode. The C5 decker provides spectroscopic resolution of 1.3 km/s/pixel and $R = 36{,}000$, which corresponds to a velocity FWHM of 8.3 km/s.

Raw data were reduced using the `HIRedux`[1] pipeline code included in `XIDL`[2], a data-reduction software package. We used the pipeline to combine multiple exposures for each sightline, calibrate spectra using flats and ThAr arcs, determine slit profiles for each order, perform sky subtraction, and remove cosmic rays. For a more detailed explanation of this procedure, we refer the reader to O'Meara et al. (2015).

Automated flux calibration of HIRES spectra is difficult and unreliable, so each echelle order was examined by eye for continuum fitting. A Legendre polynomial was fit to each order using the AstroPy-affiliated `linetools` package[3], an open-source code for analysis

[1]http://www.ucolick.org/∼xavier/HIRedux/

[2]http://www.ucolick.org/∼xavier/IDL/index.html

[3]https://github.com/linetools/linetools

of 1D spectra. After automated calibration and co-adding of all orders was complete, the continuum was again examined and adjusted by hand by placing or moving anchor points in absorption-free regions. The 3934 Å CaII K line often coincided with broad Balmer features in the stellar spectrum, in which case the continuum was adjusted to fit out these features and ensure that they did not affect column density measurements during analysis.

Finally, we corrected for cosmic rays, hot pixels, and gaps in the data which had not been removed by the `HIRedux` pipeline. Each affected pixel was assigned a new value equal to the mean of the nearest unaffected pixels on each side.

2.3 Analysis

2.3.1 Line profile fitting

For each sightline, we used CaII and NaI absorption features, along with HI 21cm emission measurements from the Effelsberg-Bonn HI Survey (EBHIS), to identify distinct components of gas in velocity space and fit line profiles to them. The features and line profiles discussed in this section are shown in Figure 2.6 for CaII K (λ 3934 Å), NaI D_2 (λ 5891 Å), and HI 21-cm along several sightlines.

Ca II and Na I absorption

We fit line profiles to the CaII H+K ($\lambda\lambda$ 3934.8, 3969.6 Å) and NaI D ($\lambda\lambda$ 5891.6, 5897.6 Å) doublets in order to measure gas velocity v, column density N, and Doppler b parameter $b_{\rm D}$. The Doppler parameter is a measure of line width, and reflects line broadening caused by both thermal and non-thermal processes. The wavelength range spanned by each absorption feature and initial guesses for the fit parameters were determined by hand using the `PyIGM IGMGUESSES` GUI[4]. Individual inspection allowed us to use priors of narrow velocity width and mask regions of severe blending when fitting multiple velocity components, which was crucial for obtaining good fits since all absorption features were fit independently of one another.

[4]https://github.com/pyigm/pyigm

These initial guesses were then passed to a fitting routine that uses the Markov Chain Monte Carlo (MCMC) technique as implemented in the Python package `emcee` (Foreman-Mackey et al., 2013) to calculate posterior probability distribution functions (PPDFs) for each model parameter. We assume that the logarithm of the likelihood function is equal to the distribution of $\chi^2/2$, adopting uniform priors over the parameter ranges $0.5 < b_{\rm D} < 75$, $8 <$ logN < 13. We use Markov Chains produced by 50 walkers taking 500 steps, with a burn-in of 150 steps. We report the median and $\pm$34th percentiles of the marginalized PPDFs as the parameter values and uncertainty intervals for each parameter, respectively.

Once the heliocentric velocities were determined by the MCMC fitting routine, they were corrected for motion relative to the Local Standard of Rest (LSR) along each sightline, so that gas which is moving at the LSR has $v_{\rm LSR} = 0$ km/s. All velocities in the following discussion are defined relative to the LSR in this way unless otherwise noted. We do not assume rotation for extraplanar gas, as any effects from rotation or halo lag are orthogonal to the inflow velocities we observe. Because our sightlines are at high Galactic latitudes ($b > 60°$, except three at $b = 51.4°, 55.2°, 57.5°$), Galactic rotation effects are not significant for line-of-sight velocities in this sample (Wakker & van Woerden, 1991). For the 48/54 sightlines at $b > 70°$, Galactic rotation introduces $< 5\%$ error in velocity, and for the remaining six sightlines at $50° < b < 70°$ the velocity error is $< 12\%$. The inflow velocities we measure vary by considerably more than 12%, which means that the trends we observe are not due to rotation effects. Lastly, if no absorption was detected, noise in the spectra near the wavelength of the line was used to calculate 2σ upper limits on equivalent width and column density. Across all sightlines, the column density detection limit had a median logN of 10.97 cm^{-2} for CaII and 10.58 cm^{-2} for NaI.

HI 21-cm emission

For purposes of comparison to the more complete observations which have been made in HI 21-cm emission, we obtained data from the Effelsberg-Bonn EBHIS HI survey (Winkel et al., 2016) and analyzed HI emission for positions closest to each BHB sightline. The positions

do not precisely match our BHB sightlines because of differing spatial resolutions; the effective beam size for EBHIS is 10.8′ compared to the 1.0″ slit used for HIRES observations (Vogt et al., 1994). The spectral resolution of EBHIS is ∼1 km/s. HI brightness temperature profiles were inspected by eye to obtain initial guesses for line profile parameters and determine the number of distinct emission features in velocity space. These components were fit simultaneously to a Gaussian mixture model, which determined the best fit with the Levenberg-Marquardt damped least-squares algorithm using the SciPy `curve_fit` optimizer (Millman & Aivazis, 2011). Note that since HI is detected in emission rather than in absorption along BHB sightlines, the upper limits on distance provided by background sources for CaII and NaI do not apply to HI.

2.3.2 Isolating Absorption Signatures of the Galactic Fountain

The distances to BHBs set upper limits on the distance to any intervening gas clouds along the line of sight. Because absorption could originate from gas anywhere along the sightline, extraplanar flows can't be distinguished from the Milky Way ISM concentrated in the Galactic disk using only the upper limits on distance available to us. However, extraplanar gas flows do exhibit kinematic signatures that allow us to differentiate them from Milky Way ISM gas.

In order to isolate absorption features associated with Galactic inflows/outflows and examine their properties, we separate absorption lines into two distinct velocity components: 'ISM' (velocities consistent with the Milky Way's interstellar medium, $|v| < 25$ km/s) and 'IV' (Intermediate Velocity gas, $|v| > 25$ km/s). The first is a component we associate with the Milky Way ISM; this is gas moving within ±25 km/s of the local standard of rest. Any gas outside this velocity range is not likely to be part of a coherent rotating disk, and may be associated with extraplanar gas flows. This so-called IV gas component is often defined as $35 < |v| < 90$ km/s, but this range is somewhat arbitrary and the cutoffs are often adjusted based on the gas velocities of features being considered (van Woerden et al., 2005). In this work we do not detect any gas at $|v| > 75$ km/s, and find that adopting a cutoff at $|v| = 25$ km/s for ISM gas best reveals the trends in these data.

It should be noted that interpretations of IV gas measurements are seldom clear-cut. At high Galactic latitudes, typical Milky Way disk gas should have low line-of sight velocities, since the bulk of its motion is in the transverse direction. However, any extraplanar gas moving at $|v| < 25$ km/s cannot be easily disentangled from disk gas (Boettcher et al., 2017; Zheng et al., 2019).

2.4 Results

Table 2.2 lists best-fit values for column density N, radial velocity v, and Doppler b parameter $b_{\rm D}$, which we combine with spatial coordinates from the SEGUE catalog to provide a characterization of IV gas in the halo. Figure 2.7 shows the distribution of the CaII, NaI, and HI parameter values fit using the methods described in §2.3.1.

We have tabulated results for gas detections at all velocities, but limit discussion in the body of this paper to the IV gas component. The results and figures for the Milky Way ISM component ($|v| < 25$ km/s) are presented in Appendix 2.7. This low-velocity gas behaves largely as expected for typical disk material, but we examine some noteworthy features of this component as they relate to IV gas.

2.4.1 Column Density

Absorption line measurements reveal how gas column densities vary across the face of the Milky Way's disk. When these measurements are combined with distances to background BHBs, we can also see how column densities vary with height above the disk, providing a 3-dimensional picture of the absorbing gas. Figure 2.8 shows total column densities for the IV gas component along each sightline, from both an edge-on view (top panel) and projected onto the plane of the Milky Way's disk (bottom panel). The markers are located at the coordinates of the background BHB; in other words, they reflect the upper limit on distance to the absorbing CaII and NaI gas. Results remain qualitatively the same if smaller distances are assumed (see Figure 2.4 for an example of the effect of distance assumptions on gas cloud coordinates). Colors indicate the column density of IV gas, with darker colors

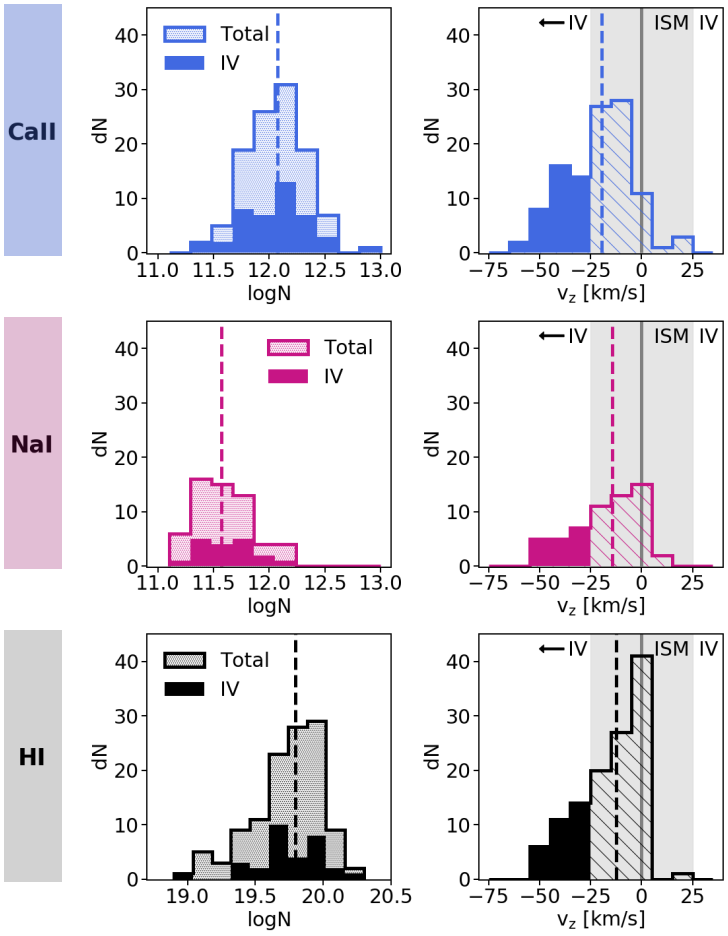

Figure 2.7: Distribution of column density & velocity. Measured column densities (left column) and the z-component of measured radial velocities (right column) for CaII, NaI, and HI. Dashed lines mark the median value for each distribution, and in the right column $v_{\rm LSR} = 0$ is indicated with a grey line. All ions are dominated by Galactic signals at $|v| < 25$ km/s (hatched fill), but a significant IV component at $v < -25$ km/s can be clearly seen (solid fill), indicating inflowing gas at the disk-halo interface.

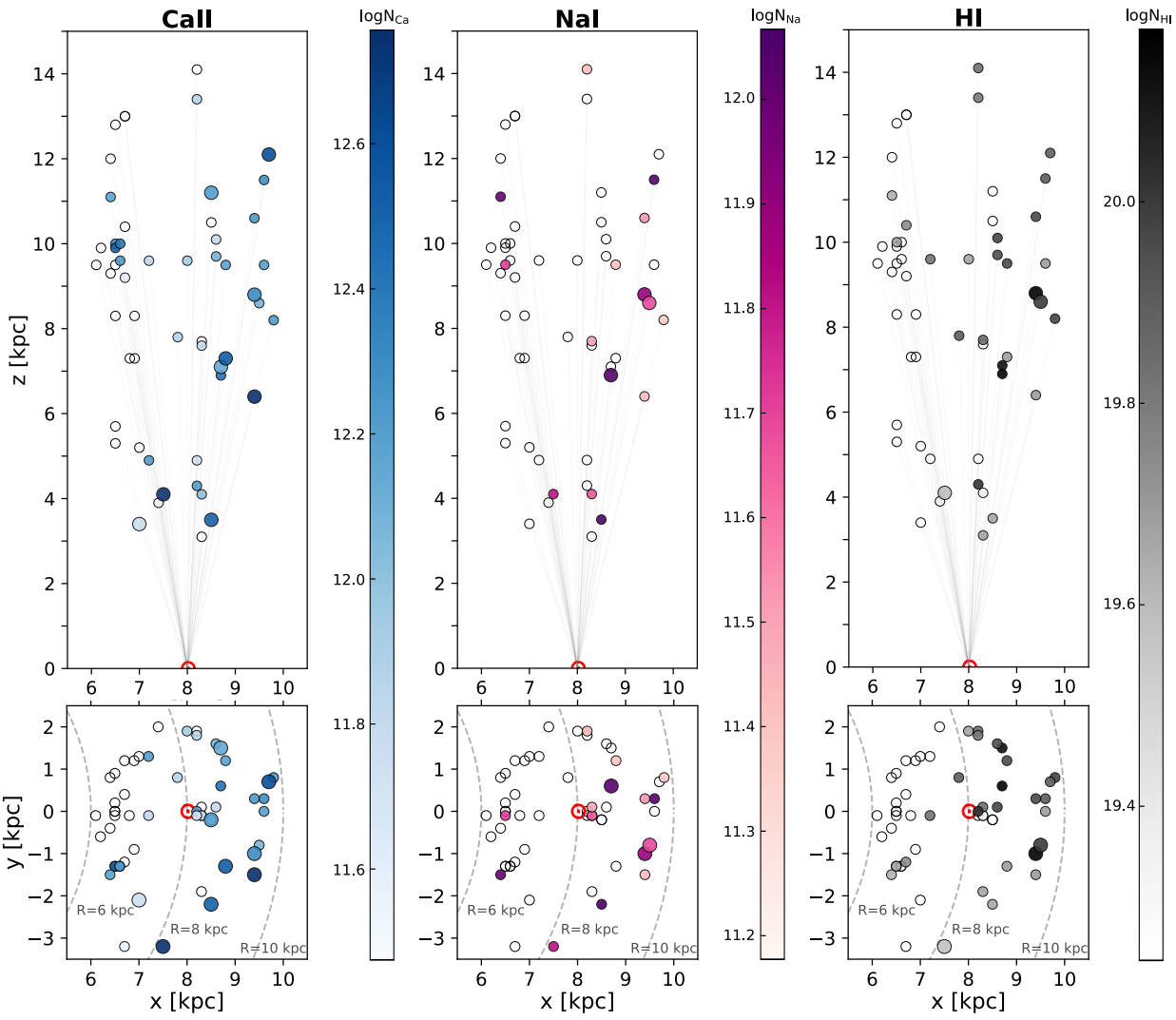

Figure 2.8: Column density measurements along BHB sightlines. Column densities for the IV component (Intermediate Velocity gas, $v < -25$ km/s). Markers correspond to background BHB sightlines projected onto the x-y and x-z planes of the Milky Way disk. The coordinates for each BHB are plotted in physical kpc units in the plane of the Milky Way; thus any inferred distance to gas absorption along a sightline is an upper limit. Color indicates column density measurements for CaII and NaI in absorption and HI in 21-cm emission. Larger markers indicate sightlines along which more than one component was detected, and their colors represent the total column density of those components. Empty circles denote nondetections. The Sun is marked by a red solar symbol, and black dashes denote lines of constant radius from Galactic center. IV column densities do not uniformly increase with z or BHB distance, implying that most of the gas is closer than the nearest background source at $z \lesssim 3.1$ kpc.

corresponding to greater column densities and empty circles denoting nondetections. Larger markers represent sightlines with multiple distinct IV gas components which have each been fit separately, and their colors represent the summed column density of those components.

In the x-y plane, most detections of IV gas are grouped together along sightlines outside the solar circle, while very little IV gas is found in the direction towards the Galactic center. This pattern is consistent across the CaII, NaI, and HI tracers. Although CaII and HI detections appear spatially coincident, we find no significant correlation between CaII and HI column densities as one might expect (Pearson $r = -0.04$, $p = 0.86$). We speculate that this may be an effect of the $10.8'$ beam size of the EBHIS HI data, which smears out signal over a large area relative to the $1''$ slit width for HIRES. Alternatively, the absence of any correlation in CaII-HI column density could be real if the HI is associated with gas in a more highly ionized phase.

Additionally, there is no significant correlation between column densities and the height probed by a sightline. This absence of any trend between total column density along a sightline and the height of the background source above the disk can be seen more clearly in Figure 2.9. If the gas were distributed uniformly or exhibited a smooth dropoff with height, we would expect to observe higher column densities along sightlines to more distant background sources. We find no evidence of such correlation (Pearson $r = -0.09$, $p = 0.64$), an indication that most of the observed gas lies at a distance closer than $z = 3.1$ kpc, the distance to the nearest background source. Further support for this picture can be seen in Figure 2.10, in which our CaII IV gas column density measurements are overlaid on a map of HI column density from the LAB survey (Kalberla et al., 2005). These CaII detections visibly coincide with the edge of two large HI complexes called the IV Arch and the IV Spur, which extend across much of the northern Galactic sky, and are estimated to sit above the Galactic disk at distances of 0.5-3 kpc (Wakker, 2001; Kuntz & Danly, 1996; Smoker et al., 2011).

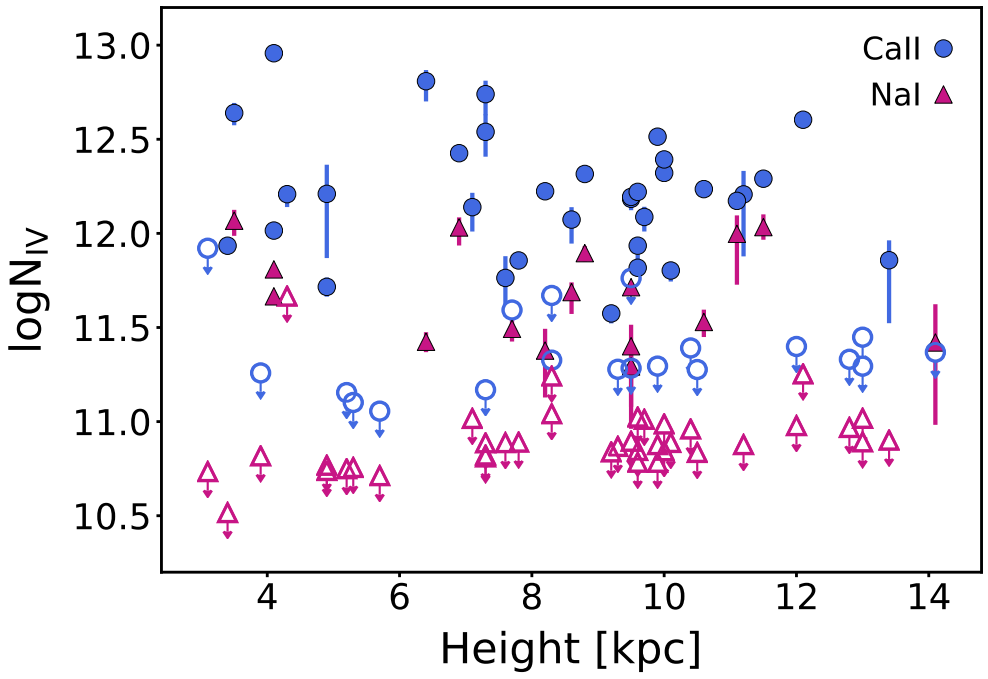

Figure 2.9: CaII and NaI lie close to the disk. The total column density of IV gas detected along BHB sightlines, which have background sources at varying heights above the disk. CaII measurements are marked by blue circles, and NaI measurements by magenta triangles. For sightlines along which no gas was detected, 2σ upper limits on column density are shown with unfilled markers. There is no correlation between the distance probed by a sightline and the total column density of gas, suggesting that most of the gas detected lies closer than the nearest background source at $z \lesssim 3.1$ kpc.

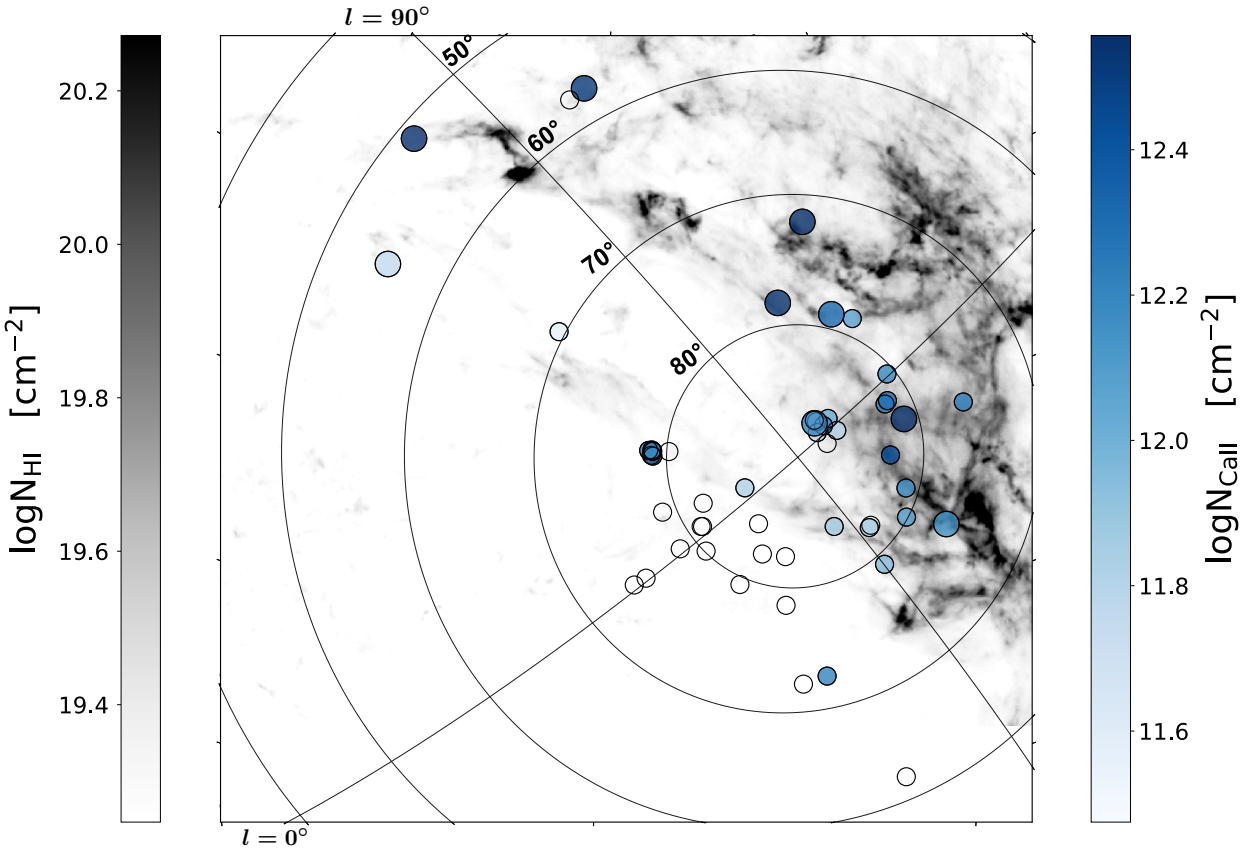

Figure 2.10: CaII column density comparison to HI 21-cm map. A map of HI column density at $-60 < v < -25$ km/s from the LAB survey in grey (Kalberla et al., 2005), overplotted with CaII IV gas column densities from this work in blue. Each marker represents a BHB sightline, colored by the total IV gas column density along that sightline. Open circles denote nondetections. Larger markers indicate sightlines with multiple distinct IV absorption components, and are colored by the total IV column density of those components. CaII detections correlate with cool gas near the edge of two large HI complexes known as the IV Arch and the IV Spur.

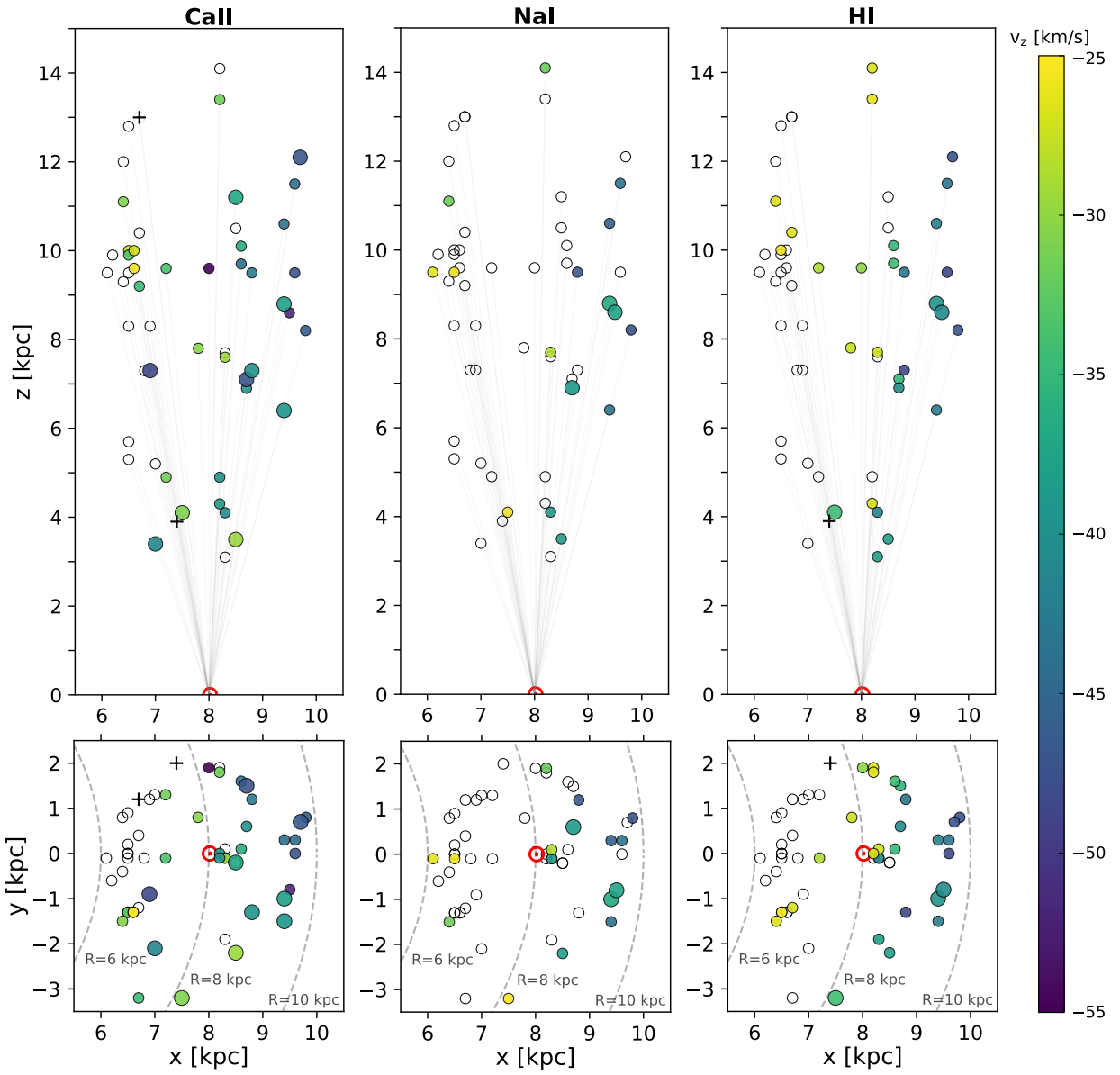

Figure 2.11: INFALL VELOCITY MEASUREMENTS ALONG BHB SIGHTLINES. Infall velocities for the IV component (Intermediate Velocity gas, $v < -25$ km/s). Markers correspond to background BHB sightlines projected onto the x-z (*top*) and x-y (*bottom*) planes of the Milky Way disk. The coordinates for each BHB are plotted in physical kpc units in the plane of the Milky Way; thus any inferred distance to gas absorption along a sightline is an upper limit. Color indicates the component of radial velocity measurements perpendicular to the disk ($v_{\rm LSR}$ sin$b$) for CaII and NaI in absorption and HI in 21-cm emission. Larger markers indicate sightlines along which more than one component was detected, and their colors represent the mean velocity of those components weighted by column density. IV gas is only detected at negative velocities, with the exception of one absorber just beyond the IV cutoff in CaII and HI, and another at $v = 40.8$ km/s in CaII. These absorbers are marked by a '+' symbol. Empty circles denote nondetections. The Sun is marked by a red solar symbol, and black dashes denote lines of constant radius from Galactic center. The infalling gas exhibits a clear velocity gradient, especially in CaII. By comparison, the 'ISM' gas shows no such trend (see Appendix 2.7).

2.4.2 Kinematics

Figure 2.11 maps infall velocities for the IV gas component, again from both an edge-on view (top panel) and projected onto the plane of the Milky Way's disk (bottom panel). Colors represent the z-component of measured radial velocities ($v_z = v\,\sin b$) in order to show motion directly towards/away from the disk. This survey has been designed to optimize constraints on the vertical component of gas velocities, so transverse velocities are not shown because they are not well-constrained by our experiment. However, results do not differ significantly if the observed radial velocity is used instead. Larger markers indicate sightlines with multiple distinct IV absorption features, and their colors represent the logN-weighted mean velocity of those components. A '+' symbol marks the location of two positive-velocity absorbers just beyond the 25 km/s IV cutoff in CaII and HI for J1223+0002, and another in CaII at 40.8 km/s for J1258+1939. These absorption features are shown in Appendix 2.8 and the parameters of their line profile fits are listed in Table 2.2. The distance constraints on our sightlines allow us to look at gas velocities in a unique way by projecting measured velocities on the x-y plane of the disk. As in the corresponding column density plot (Figure 2.8), the location of each point reflects the upper limit on distance to the absorber, which lies somewhere between the background star and the Sun. The location of the Sun is indicated with a red symbol and dashed lines indicate lines of constant radius from the Galactic center.

The IV component we have isolated reveals a distinct pattern in vertical infall velocity. Virtually all of the IV gas within 13 kpc is at negative velocities, falling towards the disk. We detect only two IV CaII absorbers at positive velocities, and a single positive-velocity HI IV absorber just beyond the ISM velocity cutoff (v = 25 km/s). This is consistent with previous findings that gas in this HI complex, as well as the vast majority of IV gas at northern Galactic latitudes, is moving towards the disk (Kuntz & Danly, 1996; Albert & Danly, 2004; Richter, 2017). We find no correlation between velocity and height above the disk; this provides further support for the picture suggested by our column density measurements in which IV gas sits mostly close to the disk at small heights (see §2.4.1). Furthermore, we find no correlation between velocity and column density (see Figure 2.12).

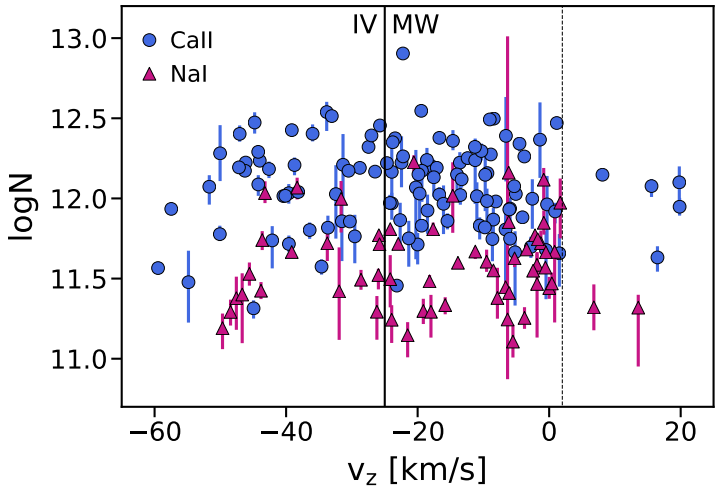

Figure 2.12: Column density & velocity are uncorrelated. Column density and z-component velocity for all distinct IV absorption components. CaII measurements are marked by blue circles and NaI by magenta triangles. There is no apparent relationship between the column density of the gas and its infall velocity. Note the abrupt dropoff in CaII and NaI detections at $v_z \gtrsim 2$ km/s, marked by the vertical dotted line. This dearth of cool gas at positive velocities is also present in HI.

IV gas does exhibit a clear infall velocity gradient across the face of the disk which is oriented roughly along the radial axis of the Milky Way. Gas infall velocities at R = 6-10 kpc increase in magnitude farther from the Galactic center (-6.0 ± 1.5 km/s/kpc in CaII, -7.0 ± 1.7 km/s/kpc in NaI, and -8.8 ± 1.3 km/s/kpc in HI). This velocity gradient is especially prominent for CaII and HI, as seen in the bottom panel of Figure 2.11. A similar trend appears in NaI, although there are fewer NaI detections overall. The gradient spans velocities from the IV cutoff at -25 km/s to -75 km/s, with faster-moving gas detected near the interior of the coincident HI IVCs mentioned in §2.4.1. In Figure 2.13, least-squares linear fits to this gradient for CaII, NaI, and HI show that this gradient is not explained by a geometric viewing effect, which would cause the z-component of observed radial velocities to be smaller for sightlines at lower Galactic latitudes, not larger.

The CaII velocity measurements are overlaid on a map of flux-weighted HI velocities from the LAB survey (Kalberla et al., 2005) in Figure 2.14. As mentioned above and shown in Figure 2.10, CaII gas detections coincide with a large HI IVC complex, probing an area at

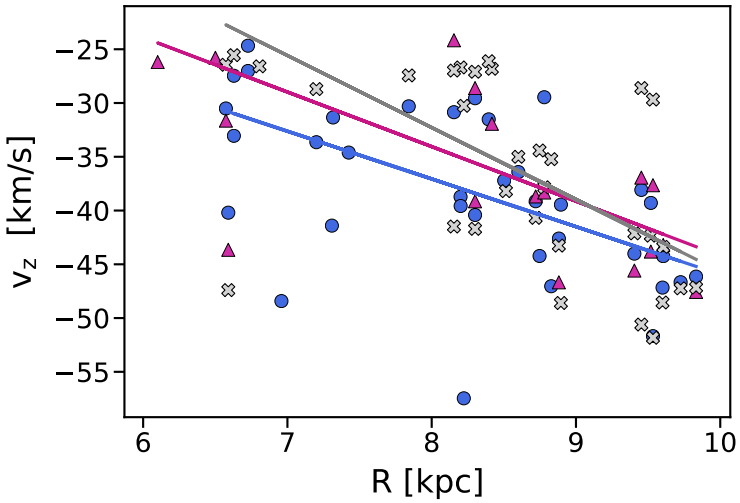

Figure 2.13: A VELOCITY GRADIENT ACROSS THE DISK. IV gas velocities for CaII and NaI detections in absorption and HI 21-cm emission, showing the z-component of measured radial velocity as it varies with distance from Galactic center. For sightlines with more than one IV component, the logN-weighted velocity is shown. Lines show the least-squares fit to the data, revealing velocity gradients of -6.0 ± 1.5 km/s/kpc in CaII, -7.0 ± 1.7 km/s/kpc in NaI, and -8.8 ± 1.3 km/s/kpc in HI.

the edge of the well-studied IV Arch and IV Spur. The locations of our CaII detections in the x-y plane are spatially coincident with that HI structure and have similar velocity gradients. However, the CaII column densities and HI column densities are not correlated, which may be a result of mismatched spatial scales probed by emission and absorption observations, respectively. Such properties of HI and CaII may indicate that large coherent structures are accreting onto the Milky Way in a manner more complex than a single-slab accreting layer (Zheng et al., 2017; Forbes & Lin, 2018). We explore various galactic fountain scenarios in our Discussion section (§2.5.2).

2.4.3 Cloud Size & Distribution

Given that the majority of detections are grouped together at $x \gtrsim 8$ kpc, it is likely that we are mapping the edge of a large structure > 3 kpc in extent. Such an extended structure may be comprised of many smaller gas cloud fragments or filaments that effectively provide uniform coverage, as is the case for some HVCs (Putman et al., 2002; Stanimirović et al.,

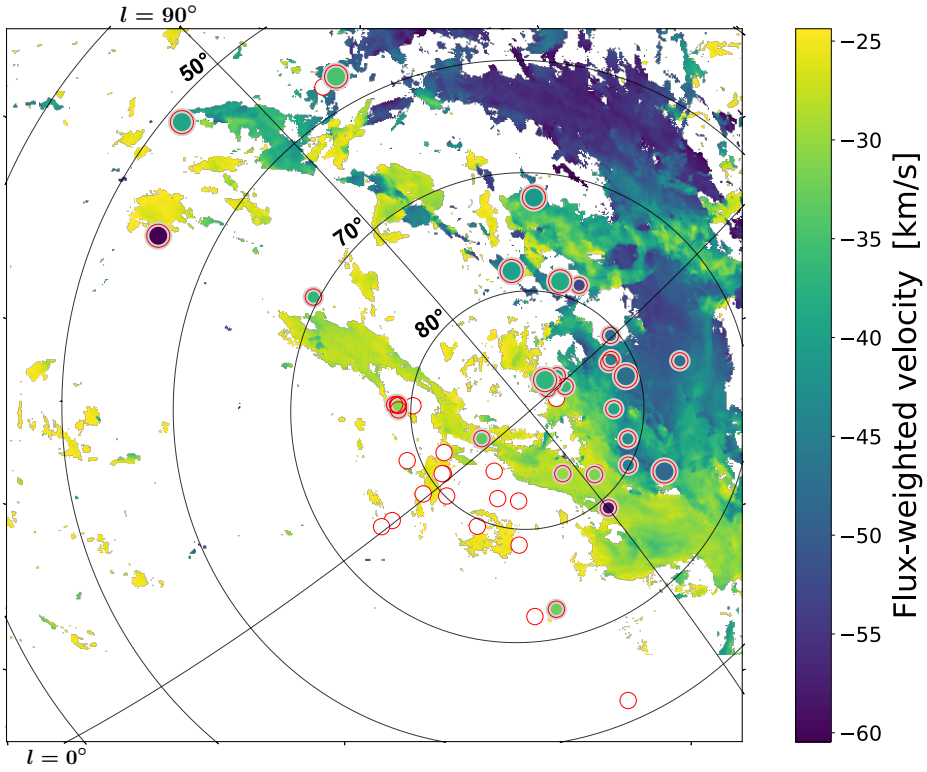

Figure 2.14: CaII velocity comparison to HI 21-cm map. A map of flux-weighted HI velocities at $-60 < v < -25$ km/s from the LAB survey (Kalberla et al., 2005), overplotted with column-density weighted infall velocities of CaII from this work. Each marker represents a BHB sightline, colored by the velocity of IV gas along that sightline. Open circles denote nondetections. Larger markers indicate sightlines with multiple IV absorption components at distinct velocities, and their color represents the mean velocity of those components weighted by column density. CaII detections correlate with the edge of two large HI complexes known as the IV Arch and the IV Spur. A velocity gradient can be seen in CaII, with faster infall velocities nearest the interior the cloud.

2008; Hsu et al., 2011; Wakker, 2001). The substructure created by these so-called clouds is probably comprised of many interrelated clumps and wisps, rather than discrete structures with well-defined boundaries (McCourt et al., 2018; Fukui et al., 2018; Marinacci et al., 2010; Ben Bekhti et al., 2007).

Comparing CaII and NaI detections to existing HI maps provides further support for wispy substructures within clouds that extend beyond the coverage of this survey. Figure 2.10 shows HI emission from the LAB survey in grey, and such morphology is clearly visible (Kalberla et al., 2005). Our IV gas detections correlate strongly with the IV Arch and IV Spur HI complexes which extend across much of the northern Galactic sky and contain clumpy substructures with angular sizes of 10-20° (Kuntz & Danly, 1993).

Distance estimates for the HI IV Arch and Spur generally fall within a range of 0.5-3 kpc (e.g., Wakker, 2001; Kuntz & Danly, 1996; Smoker et al., 2011), which is consistent with the distance constraint of $z \lesssim 3.1$ kpc we have determined for detected gas in this sample. If low-ionization Ca and Na can be tied to HI IVCs close to the disk, then measurements of HI gas provide additional spatial constraints. To illustrate this, Figure 2.4 maps the x-y coordinates of gas assuming a cloud at z=3 kpc, compared to the x-y coordinates corresponding to the upper limit on distance set by the background star. We assume a cloud height of z=3 kpc for the purposes of demonstration, since our detections place only an upper limit on this value. This figure highlights the significant effect that distance measurements can have on our ability to constrain substructure and cloud size. Connecting CaII and NaI gas with HI lying close to the disk is therefore a useful link that allows us to place tighter constraints on the scale of structures within the larger cloud probed by this survey.

Statistical variations in column density can also provide constraints on the size of gas clouds and the uniformity of their coverage across the disk (Rubin et al., 2018a,b). To show how column densities vary on different scales, we plot the difference in IV gas column density, $\Delta\log N_{\rm CaII}$, between each unique pair of sightlines in Figure 2.15. NaI and HI are not shown, but the results for those species are similar to CaII. We assume that the gas lies at a height of 3 kpc, as suggested by the trends discussed above. Figure 2.4 provides an example of how the distance scales in question are affected for a range of assumed cloud heights.

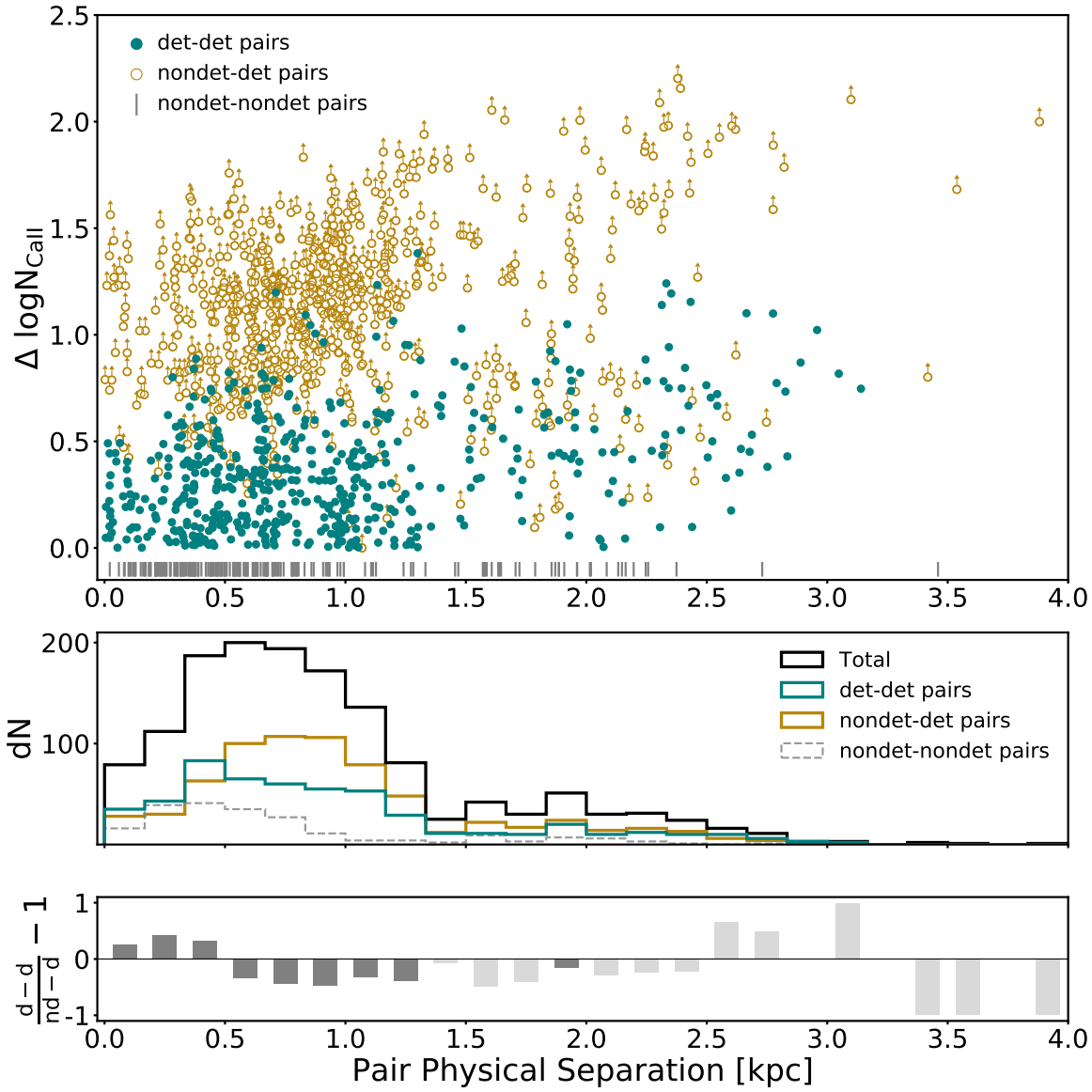

Figure 2.15: Column density variations indicate cloud sizes < 500 pc. The spatial variation of logN, which can place constraints on gas cloud size. The physical separation between IV gas along each unique pair of sightlines is calculated assuming all gas lies at z=3 kpc.
Top: Filled teal markers represent the difference in CaII column density of gas between two sightlines with CaII detections (d-d). If one sightline in the pair is a detection and one a nondetection (nd-d), lower limits on ΔlogN are determined by instrumental detection limits and indicated with an open gold marker. If both sightlines in a pair are nondetections (nd-nd), their physical separation is marked with a grey bar at the bottom of the figure.
Middle: The distribution of sightline pair separations is shown in the histogram at the top of the figure. The full set of all sightline pairs is in black, d-d pairs in teal, nd-d pairs in gold, and nd-nd in dashed grey.
Bottom: The ratio of the number of d-d pairs to nd-d pairs for each bin of the histogram above. The ratio is normalized so that it is positive when there are more d-d pairs and negative when there are more n-d pairs. Light grey bars are shown for bins in which there are fewer than 50 sightline pairs. Below scales of 0.5 kpc, there are more d-d pairs than nd-d pairs, and there is an inversion of this ratio at scales larger than 0.5 kpc. This may be an indication that there is gas substructure at scales on the order of 0.5 kpc.

In the top panel, each marker represents the difference in column density for two sightlines separated by some physical distance. Pairs of sightlines with two detections (d-d) are represented with filled teal markers. Pairs with one detection and one nondetection (nd-d) are represented by open gold markers showing the lower limits on ΔlogN as determined by instrumental detection limits. The grey bars at the bottom of the plot show the physical separation of sightline pairs with two nondetections (nd-nd). If the spatial sampling density of our sightlines is high enough to probe cloud substructure, we would expect ΔlogN to be smaller at pair separations less than the characteristic clump size. We find that column densities differ by up to two orders of magnitude, but there is no strong evidence of density fluctuations on any particular physical scale.

The histogram in the middle panel displays the distribution of sightline pair separations. The full set of all sightline pairs is in black, d-d pairs in teal, nd-d pairs in gold, and nd-nd in dashed grey. Note that the distribution of d-d pairs is skewed relative to the total distribution of sightline pairs. We expect the number of d-d pairs to increase on scales smaller than typical gas structure. The bar graph in bottom panel represents the ratio of the number of d-d pairs to nd-d pairs corresponding to each bin of the histogram above. The ratio is normalized so that it is positive when there are more d-d pairs and negative when there are more n-d pairs. At scales shorter than 0.5 kpc, there are more d-d pairs than nd-d pairs, and there is an inversion of this ratio at scales larger than 0.5 kpc.

The absence of a trend at separations larger than 0.5 kpc is an indication that any existing substructure occurs at scales no larger than 0.5 kpc, approximately twice the average separation between a sightline and its nearest neighbor (0.24 kpc). Similarly, large-scale cloud structures are likely to span areas larger than the ~ 12.6 kpc^2 covered by this survey. These constraints are consistent with the HI gas structure shown in Figure 2.10, where dense clumps have formed on scales smaller than our typical sightline separation and make up a cloud complex which extends beyond the survey area.

Covering Fraction & Volume Filling Factor

We calculate covering fraction as a convenient and simple measure of the projected sky coverage and distribution of IV gas. Before proceeding with the calculation we must recognize that our sightlines extend to varying distances, and this should be taken into account. In this case, we assume that the detected gas lies at $z = 3$ kpc and therefore all sightlines fully probe these gas clouds, and assert that this is a valid assumption based on the argument laid out in §2.4.1. See Figure 2.4 for an illustration of the effect of cloud height assumptions on distance scales.

We must also choose a column density threshold above which the covering fraction will apply. Column density measurements are a mix of detections and upper limits representing non-detections. Ideally there should be no upper limits above the chosen threshold, since this does not allow us to categorize that sightline definitively as a detection or non-detection. However, choosing a threshold that meets this criterion would exclude a significant fraction of detections in our sample (see Figure 2.9). In light of this we take the following approach: we choose a threshold of $\log N_{IV} > 11.5$ for CaII, which includes all detections and exceeds all but four upper limits, and a threshold of $\log N_{IV} > 11.3$ for NaI, which includes all detections and exceeds all but one upper limit. We treat the upper limits which exceed the threshold as detections and account for this uncertainty in the covering fraction error. The covering fraction error is determined by a standard binomial Wilson score; we calculate the 68% confidence interval treating the upper limits above the threshold as both detections and non-detections, and report the most conservative of those two values.

Using 54 sightlines, we calculate covering fractions of $f_{\rm CaII}$ ($\log N_{\rm CaII} > 11.5$) $= 63^{+6.5}_{-14.0}$%, $f_{\rm NaI}$ ($\log N_{\rm NaI} > 11.3$) $= 26^{+5.9}_{-7.6}$%, and $f_{\rm HI}$ ($\log N_{\rm HI} > 18.7$) $= 52 \pm 5.8$%. Other studies of neutral HI clouds in the Milky Way have found smaller covering fractions of ∼20-40% (Murphy et al., 1995; Wakker & van Woerden, 1991; Albert & Danly, 2004). Studies of warm HVCs in the Milky Way halo find covering fractions of ∼60-90%, larger than the low-ionization covering fractions we measure (Shull et al., 2009; Lehner & Howk, 2011; Collins et al., 2009).

If we use our statistical analysis in §2.4.3 to make an assumption about cloud size, we can also calculate the volume filling factor, given by

$$F = N_c \frac{\frac{4}{3}\pi r_c^3}{\pi R_s^2 z} \tag{2.1}$$

N_c is the total number of IV components detected along all sightlines, including six sightlines with two IV components and one sightline with three IV components. We assume that each IV gas detection is a distinct spherical cloud substructure, and that the size of these structures must be smaller than the scales we probe with this survey given the absence of statistical variation in column density described in §2.4.3. We assign an upper limit of $r_c \leq 0.1225$ kpc on cloud radius using the average xy-projected distance between a sightline and its nearest neighbor (0.245 kpc). $\pi R_s^2 = 12.6$ kpc^2 is the disk area covered by the cylindrical survey volume, and we assume the height of that cylinder to be $z = 3$ kpc since we find no evidence of IV gas at $z > 3$ kpc. This gives us volume filling factors of $F_{\rm CaII}$ ($\log{\rm N_{CaII}} > 11.5$) $\leq 0.86^{+0.07}_{-0.15}\%$, $F_{\rm NaI}$ ($\log{\rm N_{NaI}} > 11.3$) $\leq 0.35^{+0.06}_{-0.08}\%$, and $F_{\rm HI}$ ($\log{\rm N_{HI}} > 18.7$) $\leq 0.63 \pm 0.06\%$.

Although these volume filling factors are quite small compared to the covering fraction we calculate ($F_{\rm CaII} \leq 0.28\%$ vs. $f_{\rm CaII} = 63\%$), the values are not contradictory if cloud sizes are small, as suggested by our analysis of column density fluctuations in §2.4.3. Even for length scales as short as ~ 1 kpc the covering fraction of small clouds easily reaches unity, which can explain the high detection rates of low-ion CGM gas if it does in fact clump on scales < 500 pc (Liang & Remming, 2018).

2.5 Discussion

2.5.1 Implications of Small Cloud Size

The larger covering fractions and volume filling factors we see for higher ionization states support a multi-phase picture in which small clumps or droplets of cool gas are suspended

within larger clouds or streams of hotter, more diffuse gas. How this gas eventually cools and becomes incorporated into the interstellar medium remains controversial. At $T \sim 10^6$ K, thermal line emission can rapidly cool gas until it reaches $T \sim 10^4$ K, where the cooling curve drops off steeply (S. Sutherland & Dopita, 1993; Maio et al., 2007). Maller & Bullock (2004) argue that thermal instabilities naturally arise in the Galactic corona in which cool clouds condense from a hot medium, while Binney et al. (2009) have pointed out that the halo, under most assumed physical conditions, is largely stable to cooling. Instead, it may be that feedback-induced or fountain-induced cooling, in which metal-enriched clouds ejected from the disk mix with coronal material and enhance the subsequent cooling, are the relevant processes driving accretion at the disk-halo interface (Marinacci et al., 2010, 2012; Howk et al., 2018). Detailed, global hydrodynamic disk simulations will be critical to resolving the physics of gas accretion and the Galactic fountain (e.g. Fielding et al., 2017; Schneider et al., 2018; Kim & Ostriker, 2018).

The largely empirical picture of cooler, denser gas embedded within warmer, more diffuse clouds may provide insight as to why we have more sparse detections in NaI, which predominantly traces dust and dense-neutral gas ($T \lesssim 1{,}000$ K), than CaII, which traces both dense-neutral and warmer ionized gas ($T \lesssim 10{,}000$ K), despite the fact that our sensitivity to both is roughly the same (Murga et al., 2015; Puspitarini & Lallement, 2012). If NaI clouds sit within larger CaII clouds in such a hierarchical structure, then some random sightline is less likely to pass through the NaI cloud (Stern et al., 2016). More generally, if the cold phase of CGM gas lies in small, clumpy structures rather than diffuse clouds that fill a larger volume in warm phase gas, then low-ionization clouds must be relatively common in order to explain the detection rates we see.

Currently, most galaxy simulations can resolve scales of ∼500 pc at best and usually do not focus computational resources on resolving low-density gas in the CGM. In general these simulations underpredict the amount of observed CGM ions (e.g. Peeples et al., 2019; Hummels et al., 2018). Incorporating AGN feedback has improved predictions of high-ion abundances, but simulations still struggle to reproduce low-ion abundances, even for

hydrogen (Oppenheimer et al., 2018b). If low-ion CGM clouds do form on scales < 500 pc as our analysis and that of others suggests, then the resolution of CGM gas in simulations must increase by orders of magnitude in order to reflect the hydrodynamics on relevant scales (Marinacci et al., 2010; Crighton et al., 2015; McCourt et al., 2018; Liang & Remming, 2018; Sparre et al., 2019). Recent work has demonstrated that improving resolution to < 500 pc in simulations dramatically changes the characteristics of cool gas clouds (Hummels et al., 2018; Peeples et al., 2019). As simulations improve and move closer to resolving these structures on stabilization scales, observational constraints on cloud properties like the ones we present here will be useful for testing the accuracy of their predictions.

2.5.2 Gas Origins & The Galactic Fountain

The galactic fountain broadly depicts a scenario in which hot gas is ejected from a galaxy by energetic feedback processes associated with star formation and/or a central supermassive black hole, then re-accretes onto the disk to catalyze new star formation in an ongoing cycle. Our findings indicate a substantial amount of cool extraplanar gas embedded within neutral structures moving toward the disk at distances less than 3.1 kpc. The observed bulk kinematics presented in this study provide clues about the origin and fate of gas at the disk-halo interface. In this section we consider our observations in the context of the 'galactic fountain' and the potential origins of neutral infalling gas. In particular, we examine how the data might be explained by gas ejected from elsewhere within the Milky Way: either by star formation processes throughout the disk, or driven by a central galactic engine. A viable model should be able to reproduce the velocity gradient and lack of column density trends we observe.

One well-established picture of the galactic fountain places the origin of infalling gas at the sites of supernovae explosions throughout the disk. Fraternali (2017) models several variations of the disk-ejection fountain scenario that could produce the velocity gradient we see: in a simple ballistic model, particles ejected vertically from the disk will fall back to the disk at larger radii because of conservation of angular momentum. Since gravitational

potential decreases with galactic radius, ejecta at larger radii will reach a greater height. In turn, this material will reach more negative velocities by the time it reaches the disk. Such an effect could produce a radius-dependent infall velocity gradient for cooled, infalling gas. Adding in effects of condensation and drag could mean that these particles also return to the disk at significantly smaller radii. Our data can be explained by a disk-ejection scenario if outflowing gas is in a hotter phase that is difficult to detect with low ion absorption, or if the outflows are time-variable over many Myr as a result of intermittent, clustered star formation, as in the models of Kim & Ostriker (2018). Although cool outflowing gas has been detected in other local galaxies (Heckman et al., 2000; Martin, 2005; Rupke et al., 2005; Chen et al., 2010; Rubin et al., 2014; Bordoloi et al., 2014c), such outflows may have a patchy distribution across the disk, over which our observations span only a small fraction.

The velocity gradient we observe across the disk could potentially emerge in a central engine scenario as well (Bordoloi et al., 2017; Fox et al., 2015b). In this picture, gas is driven out from the center of the galaxy in a roughly conical region extending above the disk. Gas clouds cooling and condensing at the boundary of the cone at higher galactic radii would also be at greater height above the disk. This would allow gas clouds at greater radii to reach greater velocities by the time they reach the disk-halo interface. The effect would be a similar radius-dependent velocity gradient to the one described for the disk-ejection scenario above, but through a different mechanism. Over time the trajectory of this infalling gas turns toward the potential well at galactic center and begins to move more quickly across the plane of the disk, which is consistent with a lack of detected outflows in the solar neighborhood. Gas clouds which condense further from galactic center would have longer infall times and therefore experience a greater trajectory change, leading to a decrease in z-component velocities as they fall and turn towards galactic center. Although this observed phenomenon emerges nicely in a simple toy model of this scenario, it does not easily reproduce gas that predominantly lies at small z unless a full opening angle of $\phi > 110^{\circ}$ is adopted for initial gas ejection. A larger sample of halo star sightlines over the full sky would be necessary to fully test this proposed scenario.

In principle, the metal abundance of the clouds we observe could also place constraints on its origin. Gas with low metal abundance may have originated from the IGM, or been stripped from the ISM of Milky Way satellite galaxies (Kirby, 2011). Larger metal abundances would suggest that material has been processed through stars in the disk and ejected via outflows as part of a galactic fountain. Furthermore, the differing elemental yields of sources like supernovae, stellar winds, or AGN could potentially be tied to the relative abundances of various species across time scales of ∼100-300 Myr (Krumholz & Ting, 2018; Emerick et al., 2018). Unfortunately, determining the metal abundance for the extraplanar gas we observe is overall a very problematic calculation, and our data do not independently constrain the gas metallicity because of the lack of HI in absorption. We refer the reader to Wakker (2001) and Richter et al. (2001b) for discussions of metallicity determination in the IV Arch, which is estimated to be approximately solar.

When examining these results in the context of the galactic fountain, it is important to note that our velocity measurements reflect only local conditions and may not be representative of fountain gas in a global sense. Although the vertical gas velocities we measure are constraining in their own right, our sightlines do not capture gas flows in the transverse direction which are also critical for understanding fountain kinematics. However, our well-sampled kinematic measurements reinforce and confirm the observed properties of intermediate-velocity HI clouds, which have been successfully reproduced by galactic fountain models (Marasco & Fraternali, 2011; Marasco et al., 2012). The dynamics of halo gas in the Milky Way are complex, and these scenarios are highly simplified pictures which we have discussed in isolation. In reality gas kinematics are driven by an interrelated combination of several mechanisms which continuously supply the disk with gas.

2.6 Conclusions

In this work we have performed an analysis of cool ($T \sim 10^4$ K) gas at the Milky Way's disk-halo interface by examining absorption features of intermediate-velocity ($25 < |v| < 75$ km/s) CaII and NaI along sightlines to 54 high-latitude blue horizontal branch (BHB) stars

at heights of 3.1-13.4 kpc above the disk in the northern Galactic hemisphere. Distance measurements and dense sightline sampling allow us to obtain a 3-dimensional picture of the spatial extent of the gas, which we combine with the excellent resolution of Keck HIRES spectra and compare to HI 21-cm emission maps to constrain the characteristics of CGM gas flows.

1. CaII, and to a lesser extent the more sparsely detected NaI, are spatially coincident with HI emission. The detections are grouped together in the direction away from Galactic center at the edge of two large HI complexes known as the IV Arch and the IV Spur. However, CaII and HI column densities are not significantly correlated, which may be an observational effect of the large beam size of the EBHIS HI survey, or an indication that HI is associated with gas in a more highly ionized phase. (§2.4.1 and §2.5; Figures 2.8 & 2.10)

2. We find no relationship between column density along a sightline and distance to the background source, indicating that these gas clouds lie close to the disk at $z \lesssim 3.1$ kpc. (§2.4.1; Figure 2.9)

3. We detect virtually no outflowing gas, and inflows at velocities of $-75 < v_z < -25$ km/s. The gas exhibits a clear velocity gradient of ∼6-9 km/s/kpc across the disk which does not correlate with the column density of the gas. (§2.4.2; Figures 2.11 & 2.13)

4. An analysis of statistical variations in column density suggests that substructure of low ions within warm clouds exists on scales < 500 pc. Most current hydrodynamical simulations do not resolve cool CGM gas on these scales, and greater resolution may be crucial for improving simulations' chronically low predictions for observed low-ion column densities. (§2.4.3; Figure 2.15)

5. We calculate covering fractions of $f_{\rm CaII} = 63^{+6.5}_{-14.0}\%$, $f_{\rm NaI} = 26^{+5.9}_{-7.6}\%$, and $f_{\rm HI} = 52 \pm 5.8\%$, and volume filling factors of $F_{\rm CaII} \leq 0.86^{+0.07}_{-0.15}\%$, $F_{\rm NaI} \leq 0.35^{+0.06}_{-0.08}\%$, and $F_{\rm HI} \leq 0.63 \pm 0.06\%$. A comparison of covering fractions for different ions supports a multi-phase picture in which small clumps or droplets of cool gas are suspended within larger clouds or streams of hotter, more diffuse gas. (§2.4.3)

Table 2.1: PROPERTIES OF BLUE HORIZONTAL BRANCH STARS (BHBs) used as background sources to measure gas absorption. The BHB coordinates are given for a Cartesian system in which the x-axis extends from Galactic center in the direction of the Sun, y is perpendicular to x in the plane of the disk, and z is perpendicular to the disk such that the system is right-handed, with positive z towards the north Galactic pole (see §2.2.2). HRV is the heliocentric radial velocity of the BHB and b and l are Galactic latitude and longitude, respectively. Coordinates and distance measurements were obtained from the SDSS SEGUE catalog (Xue et al., 2011). Errors on distance measurements are approximately 10%.

Name	RA [h:m:s]	Dec [°:′:″]	x [kpc]	y [kpc]	z [kpc]	Distance [kpc]	b [°]	l [°]	HRV [km/s]
J1149+2828	11:49:19.16	+28:28:06.7	9.8	0.8	8.2	8.5	76.2	203.8	102.9
J1204+1947	12:04:05.42	+19:47:43.6	8.7	1.5	7.1	7.3	76.9	244.5	-205.2
J1212+2826	12:12:18.09	+28:26:02.0	9.7	0.7	12.1	12.2	81.3	202.1	40.6
J1215+2315	12:15:59.62	+23:15:57.9	8.8	1.2	9.5	9.6	81.1	236.7	61.9
J1215+3202	12:15:01.55	+32:02:20.1	9.6	0.0	9.5	9.7	80.7	178.9	-88.4
J1216+3308†	12:16:00.06	+33:08:56.2	9.4	-0.2	8.4	8.6	80.3	172.6	
J1216+3004	12:16:53.67	+30:04:08.7	9.6	0.3	11.5	11.6	81.9	189.7	59.2
J1217+2104	12:17:21.04	+21:04:11.1	8.6	1.6	9.7	9.9	80.2	249.0	-129.4
J1218+2951	12:18:00.44	+29:51:38.3	9.4	0.3	10.6	10.7	82.2	190.6	-166.9
J1219+2559	12:19:25.79	+25:59:43.0	8.7	0.6	6.9	7.0	82.8	220.1	174.2
J1223+0002	12:23:55.21	+00:02:20.9	7.4	2.0	3.9	4.4	62.1	288.1	139.8
J1223+3641	12:23:26.85	+36:41:11.1	9.5	-0.8	8.6	8.7	78.8	153.0	-80.4
J1226+1749	12:26:45.86	+17:49:52.0	8.0	1.9	9.6	9.8	79.1	270.2	60.5
J1229+2101	12:29:47.49	+21:01:35.9	8.2	1.9	14.1	14.2	82.2	262.8	211.2
J1230+2052	12:30:22.97	+20:52:21.9	8.2	1.8	13.4	13.5	82.1	264.3	174.2
J1231+3719	12:31:10.44	+37:19:08.4	9.4	-1.0	8.8	9.0	79.0	144.4	-168.0
J1234+4437	12:34:32.86	+44:37:32.1	9.4	-1.5	6.4	6.7	72.2	132.8	48.7
J1236+2837	12:36:51.75	+28:37:36.0	8.6	0.1	10.1	10.1	86.5	187.1	-195.8
J1239+2937	12:39:18.13	+29:37:52.8	8.3	-0.1	4.1	4.1	86.3	169.1	58.8
J1240+2746	12:40:54.84	+27:46:40.6	8.3	0.1	7.7	7.7	87.6	196.8	111.6
J1241+2909	12:41:17.48	+29:09:14.4	8.2	0.0	4.3	4.3	87.0	170.2	-69.9
J1242+2126	12:42:03.34	+21:26:04.2	7.8	0.8	7.8	7.8	83.9	281.9	-71.3
J1243+2842	12:43:50.94	+28:42:35.8	8.3	-0.1	7.6	7.6	87.7	169.2	-102.8
J1243+2931	12:43:39.02	+29:31:49.1	8.2	-0.1	4.9	4.9	87.0	158.0	17.2
J1244+2926	12:44:18.54	+29:26:19.4	8.5	-0.2	11.2	11.2	87.2	156.7	99.5
J1244+2939	12:44:16.47	+29:39:45.3	8.5	-0.2	10.5	10.5	87.0	154.4	-191.6
J1248+0947	12:48:10.28	+09:47:34.4	7.2	1.3	4.9	5.1	72.7	300.2	80.2
J1251+3849	12:51:11.16	+38:49:54.1	8.8	-1.3	7.3	7.4	78.3	123.2	-104.7

Name	RA [h:m:s]	Dec [°:′:″]	x [kpc]	y [kpc]	z [kpc]	Distance [kpc]	b [°]	l [°]	HRV [km/s]
J1255+0924	12:55:42.55	+09:24:23.4	7.0	1.3	5.2	5.5	72.3	306.4	150.2
J1257+1741†	12:57:57.64	+17:41:51.1	7.0	1.1	9.2	9.3	80.4	312.3	41.3
J1258+1939	12:58:58.86	+19:39:29.1	6.7	1.2	13.0	13.1	82.3	316.4	-162.3
J1259+1552	12:59:53.71	+15:52:27.7	6.9	1.2	8.3	8.5	78.6	313.3	47.1
J1306+2003	13:06:25.42	+20:03:42.3	6.5	0.9	12.8	12.9	82.1	329.6	27.4
J1307+2224	13:07:00.15	+22:24:25.7	6.7	0.4	13.0	13.1	84.1	340.6	187.9
J1310+2514	13:10:40.39	+25:14:17.4	7.2	-0.1	9.6	9.6	85.2	10.4	38.4
J1314+1751	13:14:13.24	+17:51:57.6	6.4	0.8	9.3	9.5	79.4	333.7	-31.3
J1324+2038	13:24:36.40	+20:38:17.1	6.5	0.2	8.3	8.4	80.0	354.1	28.5
J1324+2418	13:24:53.36	+24:18:36.2	6.4	-0.4	12.0	12.1	82.0	14.3	100.1
J1325+2232a	13:25:26.16	+22:32:20.5	6.5	-0.1	9.5	9.6	81.0	4.0	-148.4
J1325+2232b	13:25:54.40	+22:32:50.1	6.8	-0.1	7.3	7.4	80.9	4.4	-100.3
J1332+2054	13:32:56.98	+20:54:41.5	6.1	-0.1	9.5	9.7	78.7	1.9	109.7
J1335+2820	13:35:47.01	+28:20:41.2	6.7	-1.2	10.4	10.6	80.1	42.6	135.3
J1338+2345	13:38:25.33	+23:45:51.6	6.2	-0.6	9.9	10.1	78.9	17.9	-87.8
J1341+2801	13:41:18.85	+28:01:56.3	6.5	-1.3	9.9	10.1	78.9	40.5	-142.4
J1341+2806	13:41:52.29	+28:06:04.3	6.9	-0.9	7.3	7.5	78.8	40.8	-166.8
J1341+2823	13:41:19.85	+28:23:58.6	6.4	-1.5	11.1	11.3	78.9	42.4	-124.8
J1341+2824	13:41:27.90	+28:24:29.9	6.5	-1.3	10.0	10.2	78.9	42.4	-133.4
J1341+2829	13:41:38.30	+28:29:54.4	6.6	-1.3	10.0	10.2	78.8	42.9	-134.6
J1342+2828	13:42:43.32	+28:28:15.8	6.6	-1.3	9.6	9.8	78.6	42.7	-128.8
J1344+1842	13:44:04.41	+18:42:59.1	6.5	0.0	5.7	5.9	75.3	0.9	-74.7
J1347+1811	13:47:49.70	+18:11:43.6	6.5	0.0	5.3	5.5	74.2	1.4	18.2
J1413+5621	14:13:37.73	+56:21:57.7	8.5	-2.2	3.5	4.1	57.3	101.9	20.2
J1415+3716	14:15:57.13	+37:16:58.1	6.7	-3.2	9.2	9.9	69.5	67.9	-134.0
J1420+5520	14:20:43.45	+55:20:35.0	8.3	-1.9	3.1	3.7	57.5	99.2	-89.3
J1527+4027	15:27:50.05	+40:27:28.9	7.0	-2.1	3.4	4.1	55.2	65.6	-105.6
J1534+5015	15:34:11.23	+50:15:56.3	7.5	-3.2	4.1	5.2	51.4	81.0	-129.4

†Excluded from sample because of poor data quality

Table 2.2: PROPERTIES OF ALL CaII AND NaI GAS ABSORPTION COMPONENTS measured along BHB sightlines. $v_{\rm LSR}$ is the measured radial velocity corrected for the Local Standard of Rest in the direction of that sightline. logN is column density, and $b_{\rm D}$ is the Doppler b parameter of the absorption feature. Errors are the upper and lower quartiles determined by the MCMC line-fitting algorithm.

	CaII			**NaI**		
Name	$v_{\rm LSR}$ [km/s]	logN	b [km/s]	$v_{\rm LSR}$ [km/s]	logN	b [km/s]
J1149+2828	$-47.5^{+0.6}_{-0.6}$	$12.22^{+0.03}_{-0.03}$	$9.5^{+1.1}_{-1.1}$	$-49.0^{+3.5}_{-2.7}$	$11.38^{+0.20}_{-0.13}$	$13.5^{+14.9}_{-4.1}$
	$-20.9^{+0.4}_{-0.4}$	$12.07^{+0.45}_{-0.23}$	$1.2^{+1.4}_{-0.4}$	$-19.7^{+0.7}_{-0.6}$	$11.30^{+0.08}_{-0.08}$	$2.0^{+1.5}_{-1.1}$
J1204+1947	$-40.6^{+1.5}_{-1.1}$	$12.03^{+0.07}_{-0.06}$	$12.2^{+3.9}_{-2.6}$	$-8.1^{+1.5}_{-2.4}$	$11.38^{+0.13}_{-0.19}$	$4.7^{+3.7}_{-2.5}$
	$-12.7^{+0.6}_{-0.6}$	$12.25^{+0.03}_{-0.03}$	$9.9^{+1.1}_{-1.1}$	–	–	–
J1212+2826	$-47.6^{+2.0}_{-1.8}$	$12.40^{+0.05}_{-0.05}$	$19.9^{+2.9}_{-2.3}$	–	–	–
	$-19.6^{+0.5}_{-0.5}$	$11.83^{+0.04}_{-0.04}$	$5.3^{+1.0}_{-1.0}$	–	–	–
J1215+2315	$-43.1^{+1.5}_{-1.3}$	$12.18^{+0.06}_{-0.05}$	$16.5^{+3.6}_{-2.4}$	$-47.2^{+3.8}_{-2.4}$	$11.40^{+0.30}_{-0.13}$	$14.3^{+22.7}_{-4.7}$
	$-20.1^{+0.5}_{-0.6}$	$12.15^{+0.04}_{-0.03}$	$8.0^{+1.0}_{-0.9}$	$-20.8^{+0.1}_{-0.1}$	$12.23^{+0.06}_{-0.04}$	$2.7^{+0.3}_{-0.3}$
J1215+3202	$-47.8^{+0.7}_{-0.8}$	$12.19^{+0.03}_{-0.03}$	$11.3^{+1.6}_{-1.2}$	$-16.0^{+0.4}_{-0.3}$	$11.33^{+0.06}_{-0.05}$	$1.6^{+0.7}_{-0.5}$
	$-16.9^{+1.1}_{-1.0}$	$12.02^{+0.06}_{-0.05}$	$10.9^{+2.5}_{-1.8}$	–	–	–
J1216+3004	$-44.7^{+0.4}_{-0.4}$	$12.29^{+0.02}_{-0.02}$	$9.8^{+0.8}_{-0.8}$	$-43.6^{+0.2}_{-0.1}$	$12.03^{+0.06}_{-0.07}$	$1.9^{+0.4}_{-0.2}$
	$-10.4^{+1.5}_{-1.0}$	$12.30^{+0.06}_{-0.05}$	$18.6^{+3.5}_{-2.4}$	$-14.0^{+0.2}_{-0.2}$	$11.60^{+0.02}_{-0.02}$	$3.8^{+0.5}_{-0.5}$
J1217+2104	$-44.9^{+1.0}_{-1.1}$	$12.09^{+0.07}_{-0.06}$	$10.6^{+3.0}_{-1.6}$	$-0.8^{+0.5}_{-0.5}$	$11.85^{+0.07}_{-0.07}$	$4.2^{+0.8}_{-0.8}$
	$-24.3^{+1.0}_{-1.0}$	$11.97^{+0.10}_{-0.07}$	$7.0^{+3.9}_{-1.5}$	–	–	–
	$1.2^{+0.7}_{-0.7}$	$12.47^{+0.03}_{-0.02}$	$14.3^{+1.2}_{-1.0}$	–	–	–

	CaII			NaI		
Name	v_{LSR} [km/s]	logN	b [km/s]	v_{LSR} [km/s]	logN	b [km/s]
J1218+2951	$-44.4^{+0.5}_{-0.5}$	$12.24^{+0.03}_{-0.04}$	$8.7^{+0.8}_{-0.7}$	$-46.0^{+1.3}_{-1.5}$	$11.53^{+0.07}_{-0.07}$	$8.0^{+2.5}_{-1.9}$
	$-6.6^{+3.9}_{-3.8}$	$12.39^{+0.28}_{-0.24}$	$23.5^{+23.2}_{-11.1}$	$-17.8^{+0.4}_{-0.5}$	$11.81^{+0.04}_{-0.04}$	$4.5^{+1.1}_{-1.0}$
J1219+2559	$-39.4^{+0.3}_{-0.3}$	$12.43^{+0.02}_{-0.02}$	$9.7^{+0.5}_{-0.5}$	$-44.0^{+1.2}_{-0.9}$	$11.74^{+0.06}_{-0.06}$	$9.1^{+2.4}_{-1.5}$
	$-14.1^{+1.3}_{-2.1}$	$12.15^{+0.10}_{-0.07}$	$17.6^{+6.7}_{-3.5}$	$-34.0^{+0.9}_{-1.0}$	$11.72^{+0.11}_{-0.06}$	$7.8^{+3.9}_{-1.7}$
	–	–	–	$-5.3^{+1.0}_{-1.1}$	$11.63^{+0.05}_{-0.07}$	$7.8^{+2.2}_{-1.7}$
J1223+0002	$-15.1^{+1.5}_{-1.6}$	$12.12^{+0.05}_{-0.05}$	$21.3^{+4.2}_{-2.6}$	$-7.0^{+0.2}_{-0.2}$	$11.85^{+0.15}_{-0.09}$	$1.3^{+0.3}_{-0.3}$
	$26.1^{+4.3}_{-2.3}$	$12.10^{+0.19}_{-0.10}$	$23.4^{+15.5}_{-6.3}$	–	–	–
J1223+3641	$-52.7^{+1.0}_{-1.7}$	$12.07^{+0.11}_{-0.07}$	$8.3^{+3.1}_{-2.1}$	$-50.6^{+0.7}_{-0.7}$	$11.19^{+0.13}_{-0.09}$	$1.7^{+3.9}_{-1.1}$
	$-16.4^{+1.7}_{-3.6}$	$11.97^{+0.19}_{-0.11}$	$12.7^{+9.1}_{-4.3}$	$-26.5^{+0.3}_{-0.3}$	$11.52^{+0.09}_{-0.04}$	$2.1^{+1.2}_{-0.9}$
	$16.8^{+0.8}_{-0.8}$	$11.63^{+0.09}_{-0.07}$	$3.5^{+2.1}_{-1.7}$	–	–	–
J1226+1749	$-58.5^{+0.6}_{-0.7}$	$11.93^{+0.03}_{-0.04}$	$9.2^{+1.3}_{-1.0}$	$0.4^{+1.1}_{-1.2}$	$11.47^{+0.06}_{-0.07}$	$8.9^{+2.5}_{-1.9}$
	$-19.8^{+1.1}_{-0.9}$	$12.55^{+0.03}_{-0.03}$	$24.3^{+2.9}_{-2.4}$	–	–	–
J1229+2101	$-22.7^{+8.7}_{-7.1}$	$12.22^{+0.15}_{-0.16}$	$41.9^{+19.2}_{-14.7}$	$-1.3^{+0.9}_{-0.9}$	$11.72^{+0.06}_{-0.08}$	$8.6^{+1.6}_{-1.4}$
J1230+2052	$-31.8^{+3.8}_{-5.6}$	$11.86^{+0.25}_{-0.12}$	$24.5^{+26.7}_{-8.1}$	$1.1^{+0.3}_{-0.3}$	$11.77^{+0.07}_{-0.05}$	$5.9^{+1.3}_{-1.1}$
	$-2.8^{+1.0}_{-0.9}$	$11.70^{+0.07}_{-0.06}$	$8.8^{+2.5}_{-1.7}$	–	–	–
J1231+3719	$-51.0^{+0.6}_{-0.7}$	$11.78^{+0.04}_{-0.05}$	$5.7^{+1.5}_{-1.4}$	$-49.4^{+1.0}_{-0.9}$	$11.29^{+0.09}_{-0.08}$	$4.7^{+1.6}_{-1.5}$
	$-27.0^{+0.6}_{-0.7}$	$12.17^{+0.03}_{-0.03}$	$11.7^{+1.2}_{-1.1}$	$-26.4^{+0.3}_{-0.3}$	$11.77^{+0.03}_{-0.03}$	$4.3^{+0.7}_{-0.7}$
	$1.6^{+2.3}_{-3.6}$	$11.66^{+0.21}_{-0.12}$	$11.3^{+9.7}_{-3.9}$	$6.9^{+1.9}_{-2.7}$	$11.32^{+0.14}_{-0.14}$	$7.4^{+4.6}_{-3.0}$

	CaII			NaI		
Name	v_{LSR} [km/s]	logN	b [km/s]	v_{LSR} [km/s]	logN	b [km/s]
J1234+4437	$-35.5^{+1.7}_{-1.8}$	$12.54^{+0.12}_{-0.06}$	$26.5^{+10.1}_{-4.8}$	$-46.0^{+0.7}_{-0.7}$	$11.42^{+0.05}_{-0.05}$	$8.2^{+1.7}_{-1.6}$
	$-9.9^{+0.6}_{-0.6}$	$12.16^{+0.03}_{-0.04}$	$9.2^{+1.3}_{-1.0}$	–	–	–
	$8.5^{+0.5}_{-0.5}$	$12.15^{+0.04}_{-0.03}$	$8.4^{+1.4}_{-1.1}$	–	–	–
J1236+2837	$-36.5^{+0.7}_{-0.8}$	$11.80^{+0.06}_{-0.05}$	$8.1^{+1.5}_{-1.2}$	$-18.2^{+0.5}_{-0.4}$	$11.48^{+0.04}_{-0.04}$	$3.2^{+1.2}_{-1.1}$
	$-15.5^{+0.7}_{-0.6}$	$11.86^{+0.05}_{-0.05}$	$6.7^{+1.7}_{-1.1}$	–	–	–
	$-2.6^{+1.9}_{-3.9}$	$12.00^{+0.19}_{-0.12}$	$16.1^{+9.1}_{-5.0}$	–	–	–
J1239+2937	$-40.5^{+0.3}_{-0.3}$	$12.01^{+0.02}_{-0.02}$	$8.3^{+0.6}_{-0.5}$	$-39.2^{+0.2}_{-0.2}$	$11.67^{+0.03}_{-0.03}$	$2.3^{+0.4}_{-0.4}$
	$-20.0^{+1.0}_{-1.5}$	$11.71^{+0.12}_{-0.07}$	$10.8^{+5.9}_{-2.4}$	–	–	–
	$-0.5^{+1.7}_{-2.8}$	$11.68^{+0.31}_{-0.12}$	$15.5^{+20.8}_{-5.3}$	–	–	–
J1240+2746	$-22.2^{+1.3}_{-1.1}$	$12.26^{+0.04}_{-0.04}$	$24.0^{+4.2}_{-3.0}$	$-28.6^{+2.2}_{-2.3}$	$11.49^{+0.06}_{-0.06}$	$16.9^{+3.6}_{-2.7}$
J1241+2909	$-38.8^{+1.0}_{-1.5}$	$12.21^{+0.06}_{-0.05}$	$14.4^{+3.0}_{-2.0}$	–	–	–
	$-8.6^{+1.4}_{-2.4}$	$11.75^{+0.14}_{-0.10}$	$10.4^{+4.9}_{-2.7}$	–	–	–
J1242+2126	$-30.5^{+0.4}_{-0.5}$	$11.86^{+0.03}_{-0.03}$	$5.5^{+0.9}_{-0.7}$	$-0.8^{+0.3}_{-0.3}$	$12.12^{+0.19}_{-0.07}$	$2.3^{+0.6}_{-0.6}$
	$-11.1^{+2.1}_{-2.8}$	$12.01^{+0.15}_{-0.09}$	$19.2^{+10.5}_{-4.6}$	–	–	–
J1243+2842	$-29.6^{+4.0}_{-3.7}$	$11.76^{+0.17}_{-0.13}$	$17.9^{+10.6}_{-5.5}$	$-1.9^{+1.2}_{-1.4}$	$11.59^{+0.07}_{-0.07}$	$10.3^{+4.2}_{-1.9}$
	$-13.5^{+1.3}_{-1.1}$	$12.02^{+0.06}_{-0.06}$	$17.0^{+4.2}_{-2.6}$	–	–	–
J1243+2931	$-39.6^{+1.1}_{-0.9}$	$11.72^{+0.05}_{-0.05}$	$9.1^{+2.1}_{-1.5}$	$-21.5^{+2.2}_{-1.2}$	$11.15^{+0.14}_{-0.08}$	$7.0^{+4.6}_{-2.2}$

	CaII			NaI		
Name	v_{LSR} [km/s]	logN	b [km/s]	v_{LSR} [km/s]	logN	b [km/s]
	$-9.5^{+1.7}_{-1.1}$	$11.98^{+0.20}_{-0.08}$	$11.5^{+9.2}_{-2.6}$	$-8.5^{+0.2}_{-0.2}$	$11.55^{+0.02}_{-0.02}$	$3.8^{+0.5}_{-0.5}$
J1244+2926	$-24.0^{+1.9}_{-2.4}$	$12.17^{+0.22}_{-0.17}$	$12.3^{+10.1}_{-4.9}$	$-24.2^{+0.4}_{-0.4}$	$11.50^{+0.18}_{-0.15}$	$0.7^{+0.5}_{-0.1}$
	$-8.9^{+0.7}_{-0.9}$	$12.27^{+0.03}_{-0.03}$	$11.4^{+1.5}_{-1.2}$	$-6.6^{+0.6}_{-0.7}$	$11.45^{+0.04}_{-0.04}$	$7.3^{+1.3}_{-1.1}$
	$19.9^{+1.0}_{-0.9}$	$11.95^{+0.06}_{-0.06}$	$9.4^{+2.2}_{-1.6}$	–	–	–
J1244+2939	$-8.4^{+0.5}_{-0.6}$	$12.50^{+0.01}_{-0.01}$	$17.4^{+0.8}_{-0.7}$	$-6.2^{+0.2}_{-0.2}$	$12.16^{+0.01}_{-0.02}$	$5.5^{+0.4}_{-0.4}$
J1248+0947	$-8.9^{+1.3}_{-0.5}$	$11.87^{+0.12}_{-0.07}$	$11.7^{+5.6}_{-2.5}$	$-10.0^{+0.6}_{-0.3}$	$11.61^{+0.06}_{-0.07}$	$7.9^{+2.3}_{-2.4}$
J1251+3849	$-51.1^{+5.8}_{-5.5}$	$12.28^{+0.17}_{-0.18}$	$35.8^{+19.3}_{-12.7}$	–	–	–
	$-29.4^{+0.8}_{-0.8}$	$12.19^{+0.03}_{-0.03}$	$14.8^{+1.7}_{-1.3}$	–	–	–
	$-6.2^{+0.6}_{-0.5}$	$11.93^{+0.04}_{-0.04}$	$7.5^{+1.1}_{-0.9}$	–	–	–
J1255+0924	$-19.4^{+2.0}_{-1.1}$	$11.92^{+0.15}_{-0.10}$	$13.6^{+7.8}_{-3.2}$	$-15.4^{+4.7}_{-3.3}$	$12.02^{+0.23}_{-0.21}$	$31.4^{+23.6}_{-13.4}$
	$-6.2^{+0.5}_{-0.5}$	$11.75^{+0.04}_{-0.04}$	$6.4^{+1.4}_{-1.2}$	$-6.4^{+0.4}_{-0.4}$	$11.41^{+0.04}_{-0.04}$	$2.8^{+1.3}_{-1.1}$
J1258+1939	$-13.7^{+4.3}_{-2.6}$	$12.22^{+0.10}_{-0.07}$	$26.0^{+8.0}_{-4.2}$	$0.0^{+0.6}_{-0.5}$	$11.44^{+0.07}_{-0.07}$	$2.7^{+1.5}_{-1.2}$
	$0.9^{+0.9}_{-1.1}$	$11.92^{+0.07}_{-0.05}$	$9.8^{+2.9}_{-1.9}$	–	–	–
	$40.8^{+0.9}_{-0.9}$	$11.55^{+0.06}_{-0.07}$	$5.5^{+1.6}_{-1.5}$	–	–	–
J1259+1552	$-19.0^{+1.0}_{-0.9}$	$12.24^{+0.10}_{-0.08}$	$6.7^{+3.1}_{-2.4}$	–	–	–
	$-1.4^{+8.0}_{-5.9}$	$12.37^{+0.24}_{-0.23}$	$30.6^{+28.8}_{-14.3}$	–	–	–
J1306+2003	$-13.7^{+3.1}_{-1.6}$	$12.17^{+0.19}_{-0.08}$	$13.5^{+9.1}_{-3.7}$	$7.8^{+0.2}_{-0.2}$	$11.97^{+0.22}_{-0.15}$	$1.4^{+1.1}_{-0.3}$

	CaII			NaI		
Name	v_{LSR} [km/s]	logN	b [km/s]	v_{LSR} [km/s]	logN	b [km/s]
	$1.9^{+0.6}_{-0.8}$	$12.34^{+0.05}_{-0.04}$	$10.5^{+1.9}_{-1.5}$	–	–	–
J1307+2224	–	–	–	$0.8^{+1.9}_{-3.6}$	$11.67^{+0.44}_{-0.23}$	$13.8^{+27.0}_{-7.6}$
J1310+2514	$-33.8^{+0.9}_{-0.9}$	$11.82^{+0.07}_{-0.07}$	$6.3^{+1.8}_{-1.4}$	–	–	–
	$-9.8^{+3.3}_{-5.7}$	$12.15^{+0.23}_{-0.12}$	$20.9^{+18.7}_{-6.6}$	–	–	–
J1314+1751	–	–	–	$-2.2^{+0.3}_{-0.3}$	$11.77^{+0.03}_{-0.02}$	$3.7^{+0.7}_{-0.7}$
J1324+2038	$-17.9^{+1.4}_{-1.0}$	$12.20^{+0.07}_{-0.05}$	$14.1^{+3.6}_{-2.0}$	$13.8^{+1.1}_{-0.9}$	$11.32^{+0.37}_{-0.08}$	$4.2^{+13.3}_{-2.0}$
	$15.8^{+0.3}_{-0.3}$	$12.08^{+0.07}_{-0.04}$	$3.1^{+0.7}_{-0.8}$	–	–	–
J1324+2418	$-24.5^{+0.7}_{-0.8}$	$11.97^{+0.04}_{-0.05}$	$6.6^{+1.4}_{-1.3}$	$-23.2^{+0.3}_{-0.3}$	$11.72^{+0.02}_{-0.03}$	$4.5^{+0.5}_{-0.5}$
J1325+2232a	$-14.8^{+2.1}_{-1.6}$	$12.36^{+0.06}_{-0.07}$	$20.7^{+3.5}_{-3.1}$	$-26.1^{+0.4}_{-0.4}$	$11.71^{+0.03}_{-0.04}$	$6.3^{+0.8}_{-0.9}$
J1325+2232b	$-17.3^{+0.3}_{-0.3}$	$12.19^{+0.02}_{-0.02}$	$9.7^{+0.6}_{-0.5}$	$-18.2^{+1.4}_{-1.6}$	$11.29^{+0.16}_{-0.11}$	$8.0^{+8.0}_{-3.1}$
J1332+2054	$-11.5^{+1.1}_{-1.1}$	$11.57^{+0.03}_{-0.03}$	$3.2^{+0.8}_{-0.8}$	$-26.7^{+0.5}_{-0.5}$	$11.29^{+0.17}_{-0.10}$	$0.9^{+1.5}_{-0.4}$
	–	–	–	$-0.6^{+0.3}_{-0.3}$	$11.57^{+0.03}_{-0.03}$	$3.2^{+0.8}_{-0.8}$
J1335+2820	$-24.2^{+0.5}_{-0.6}$	$12.35^{+0.03}_{-0.03}$	$11.3^{+0.9}_{-0.9}$	–	–	–
J1338+2345	–	–	–	–	–	–

	CaII			NaI		
Name	v_{LSR} [km/s]	logN	b [km/s]	v_{LSR} [km/s]	logN	b [km/s]
J1341+2801	$-33.7^{+1.0}_{-0.9}$	$12.51^{+0.02}_{-0.02}$	$28.1^{+2.4}_{-1.6}$	–	–	–
J1341+2806	$-72.6^{+4.4}_{-3.5}$	$12.42^{+0.15}_{-0.13}$	$35.4^{+19.1}_{-10.0}$	–	–	–
	$-26.2^{+1.9}_{-2.0}$	$12.46^{+0.04}_{-0.03}$	$35.8^{+5.2}_{-3.8}$	–	–	–
J1341+2823	$-31.1^{+0.3}_{-0.3}$	$12.17^{+0.02}_{-0.02}$	$9.0^{+0.5}_{-0.5}$	$-32.2^{+0.1}_{-0.2}$	$12.00^{+0.21}_{-0.11}$	$0.9^{+0.2}_{-0.2}$
J1341+2824	$-28.0^{+0.6}_{-0.5}$	$12.32^{+0.02}_{-0.02}$	$14.9^{+0.9}_{-0.8}$	–	–	–
J1341+2829	$-27.5^{+0.4}_{-0.4}$	$12.39^{+0.02}_{-0.03}$	$7.6^{+0.6}_{-0.6}$	–	–	–
J1342+2828	$-25.2^{+0.6}_{-0.5}$	$12.22^{+0.02}_{-0.02}$	$12.8^{+1.0}_{-0.9}$	–	–	–
J1344+1842	$-24.2^{+0.2}_{-0.2}$	$12.38^{+0.01}_{-0.01}$	$14.1^{+0.5}_{-0.5}$	$-24.8^{+2.0}_{-1.2}$	$11.24^{+0.14}_{-0.09}$	$8.6^{+7.7}_{-3.1}$
	$-5.2^{+0.5}_{-0.6}$	$12.03^{+0.02}_{-0.02}$	$11.2^{+0.9}_{-0.8}$	$-3.5^{+0.2}_{-0.2}$	$11.68^{+0.02}_{-0.02}$	$2.7^{+0.6}_{-0.5}$
J1347+1811	$-9.4^{+0.7}_{-0.6}$	$12.49^{+0.03}_{-0.03}$	$20.4^{+2.0}_{-2.0}$	$-1.8^{+0.3}_{-0.3}$	$11.74^{+0.02}_{-0.02}$	$6.6^{+0.7}_{-0.6}$
J1413+5621	$-45.4^{+0.2}_{-0.2}$	$12.04^{+0.02}_{-0.02}$	$4.4^{+0.9}_{-1.0}$	$-45.6^{+0.1}_{-0.1}$	$12.07^{+0.07}_{-0.06}$	$1.5^{+0.2}_{-0.1}$
	$-4.8^{+1.0}_{-1.1}$	$11.88^{+0.04}_{-0.04}$	$12.6^{+1.9}_{-1.6}$	$-4.5^{+1.3}_{-1.2}$	$11.25^{+0.07}_{-0.07}$	$10.3^{+2.7}_{-2.2}$
J1415+3716	$-36.9^{+0.8}_{-0.8}$	$11.57^{+0.05}_{-0.04}$	$6.9^{+1.5}_{-1.2}$	$-5.9^{+1.4}_{-1.7}$	$11.11^{+0.10}_{-0.10}$	$6.0^{+3.2}_{-2.6}$
	$-8.7^{+1.1}_{-1.0}$	$11.98^{+0.03}_{-0.03}$	$16.6^{+1.9}_{-1.9}$	–	–	–
J1420+5520	$-11.6^{+0.6}_{-0.5}$	$11.82^{+0.04}_{-0.03}$	$7.9^{+1.6}_{-1.1}$	–	–	–

	CaII			NaI		
Name	v_{LSR} [km/s]	logN	b [km/s]	v_{LSR} [km/s]	logN	b [km/s]
J1527+4027	$-72.4^{+0.3}_{-0.3}$	$11.57^{+0.02}_{-0.02}$	$5.4^{+0.6}_{-0.6}$	$-3.0^{+0.1}_{-0.1}$	$11.55^{+0.02}_{-0.02}$	$2.6^{+0.4}_{-0.5}$
	$-54.7^{+0.5}_{-0.7}$	$11.31^{+0.06}_{-0.05}$	$5.0^{+1.6}_{-1.2}$	–	–	–
	$-28.2^{+0.3}_{-0.3}$	$11.46^{+0.03}_{-0.03}$	$4.5^{+0.7}_{-0.7}$	–	–	–
	$-6.5^{+0.2}_{-0.2}$	$12.08^{+0.01}_{-0.01}$	$9.6^{+0.3}_{-0.3}$	–	–	–
J1534+5015	$-51.3^{+0.1}_{-0.1}$	$12.02^{+0.01}_{-0.01}$	$5.1^{+0.2}_{-0.2}$	$-30.9^{+0.2}_{-0.2}$	$11.81^{+0.01}_{-0.02}$	$4.4^{+0.3}_{-0.3}$
	$-28.4^{+0.04}_{-0.04}$	$12.90^{+0.03}_{-0.03}$	$4.1^{+0.1}_{-0.1}$	$-0.6^{+0.2}_{-0.2}$	$11.66^{+0.03}_{-0.02}$	$2.6^{+0.6}_{-0.6}$
	$-4.8^{+0.3}_{-0.3}$	$12.26^{+0.01}_{-0.01}$	$15.9^{+0.5}_{-0.4}$	–	–	–

[†]Excluded from sample because of poor data quality

2.7 Appendix A: Milky Way ISM Results

2.7.1 Column Density

ISM component column densities are shown in Figure 2.7.1, which can be compared directly with the IV component in Figure 2.8. Higher CaII and NaI column density detections are grouped together at positive y values (the direction of Galactic rotation), in contrast to the IV component which has high CaII and NaI column density detections clustered together at positive x values (the direction away from Galactic center). The pattern for HI column densities, which are higher at $x < 8$ kpc, do not match CaII and NaI for ISM gas as they do for IV gas. The Sun, at $x = 8$ kpc, is nestled just outside the the Sagittarius spiral arm of the Milky Way, and the elevated HI column density measurements we measure in that direction can be explained by this feature (Vallée, 2016, 2017).

2.7.2 Kinematics

Figure 2.7.2 shows ISM gas component velocities, which again are directly comparable to the IV component results shown in Figure 2.11. Detections of Milky Way disk gas (Figure 2.7.2) are relatively uniform and show no clear spatial trends in velocity, although most of the gas is moving at negative velocities in the same direction as accreting gas in the IV component. This is somewhat unexpected for normal gas in the disk, which should have an average z-component velocity close to zero relative to the local standard of rest. Therefore, it is possible that these metals are not associated with normal ISM gas and are either slow-moving extraplanar gas that was not separated from disk gas by our $|v| < 25$ km/s velocity cut, or gas affected by some other phenomenon within the disk (Zheng et al., 2015).

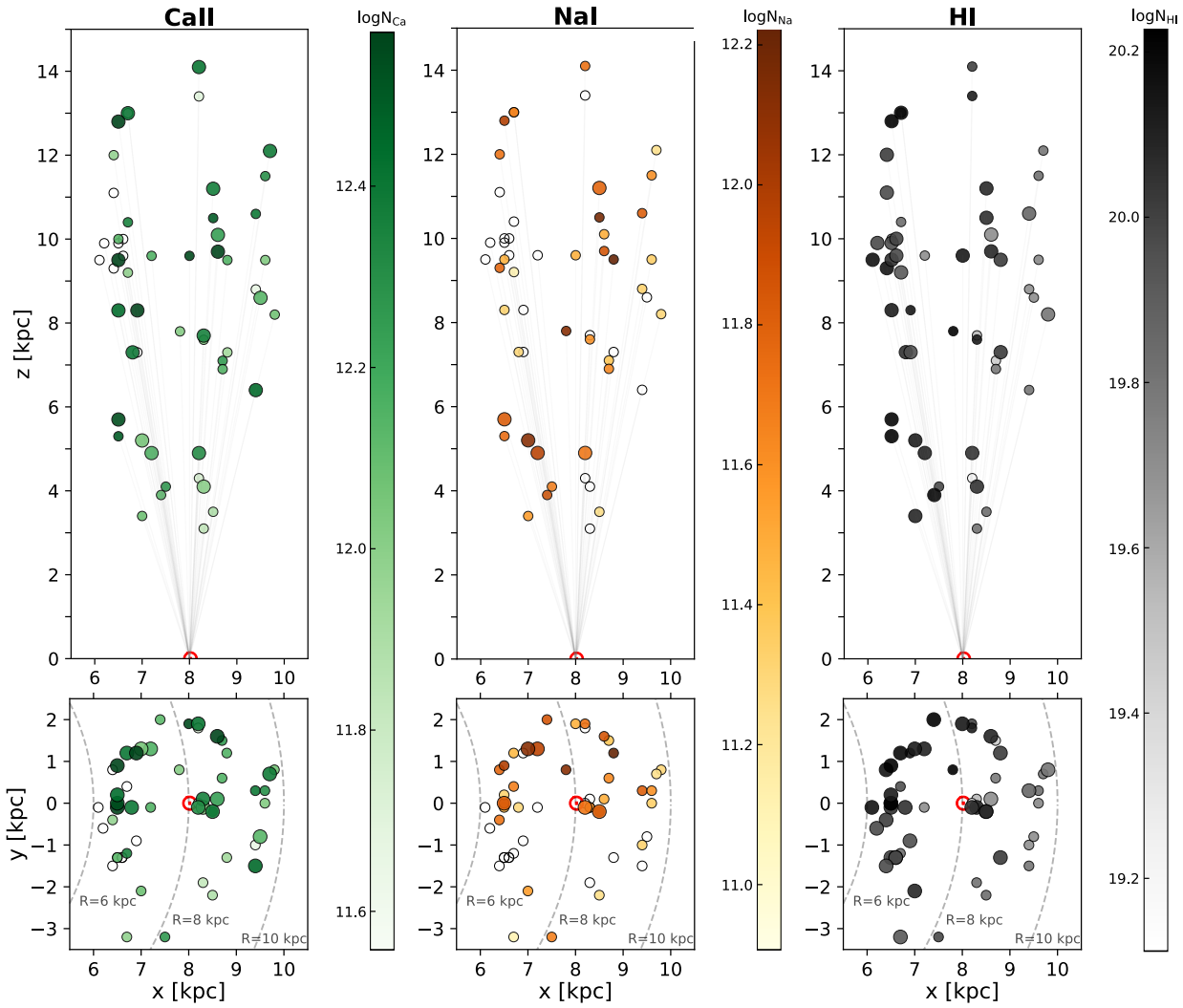

Figure 2.7.1: ISM COMPONENT COLUMN DENSITY MEASUREMENTS. Column densities for the ISM component (Milky Way ISM gas, $|v| < 25$ km/s). Markers correspond to background BHB sightlines projected onto the x-y plane of the Milky Way disk. The coordinates for each BHB are plotted in physical kpc units in the plane of the Milky Way; thus any inferred distance to gas absorption along a sightline is an upper limit. Color indicates column density measurements for CaII and NaI in absorption and HI in 21-cm emission. Larger markers indicate sightlines along which more than one component was detected, and their colors represent the mean column density of those components. Empty circles denote nondetections. The Sun is marked by a red solar symbol, and black dashes denote lines of constant radius from Galactic center.

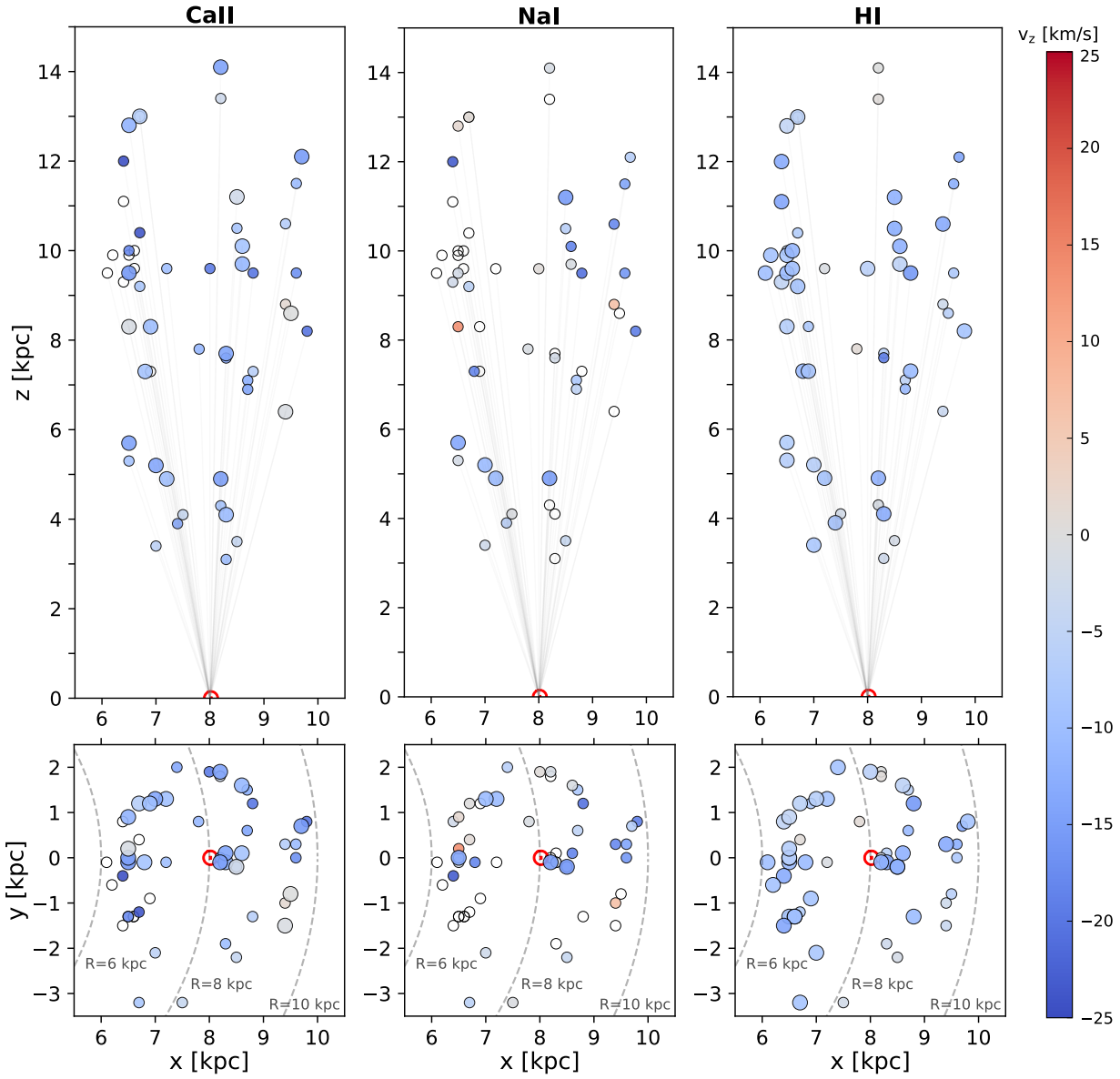

Figure 2.7.2: ISM COMPONENT VELOCITY MEASUREMENTS. Velocities for the ISM component (Milky Way ISM gas, $|v| < 25$ km/s). Markers correspond to background BHB sightlines projected onto the x-y plane of the Milky Way disk. The coordinates for each BHB are plotted in physical kpc units in the plane of the Milky Way; thus any inferred distance to gas absorption along a sightline is an upper limit. Color indicates the component of radial velocity measurements perpendicular to the disk ($v_{\rm LSR}$ sin$b$) for CaII and NaI in absorption and HI in 21-cm emission. Larger markers indicate sightlines along which more than one component was detected, and their colors represent the mean velocity of those components weighted by column density. Empty circles denote nondetections. The Sun is marked by a red solar symbol, and black dashes denote lines of constant radius from Galactic center. In contrast to the 'IV' component, the CaII and NaI ISM component does not exhibit any spatial velocity gradient across space.

2.8 *Appendix B: BHB Absorption Features & Line Profile Fits*

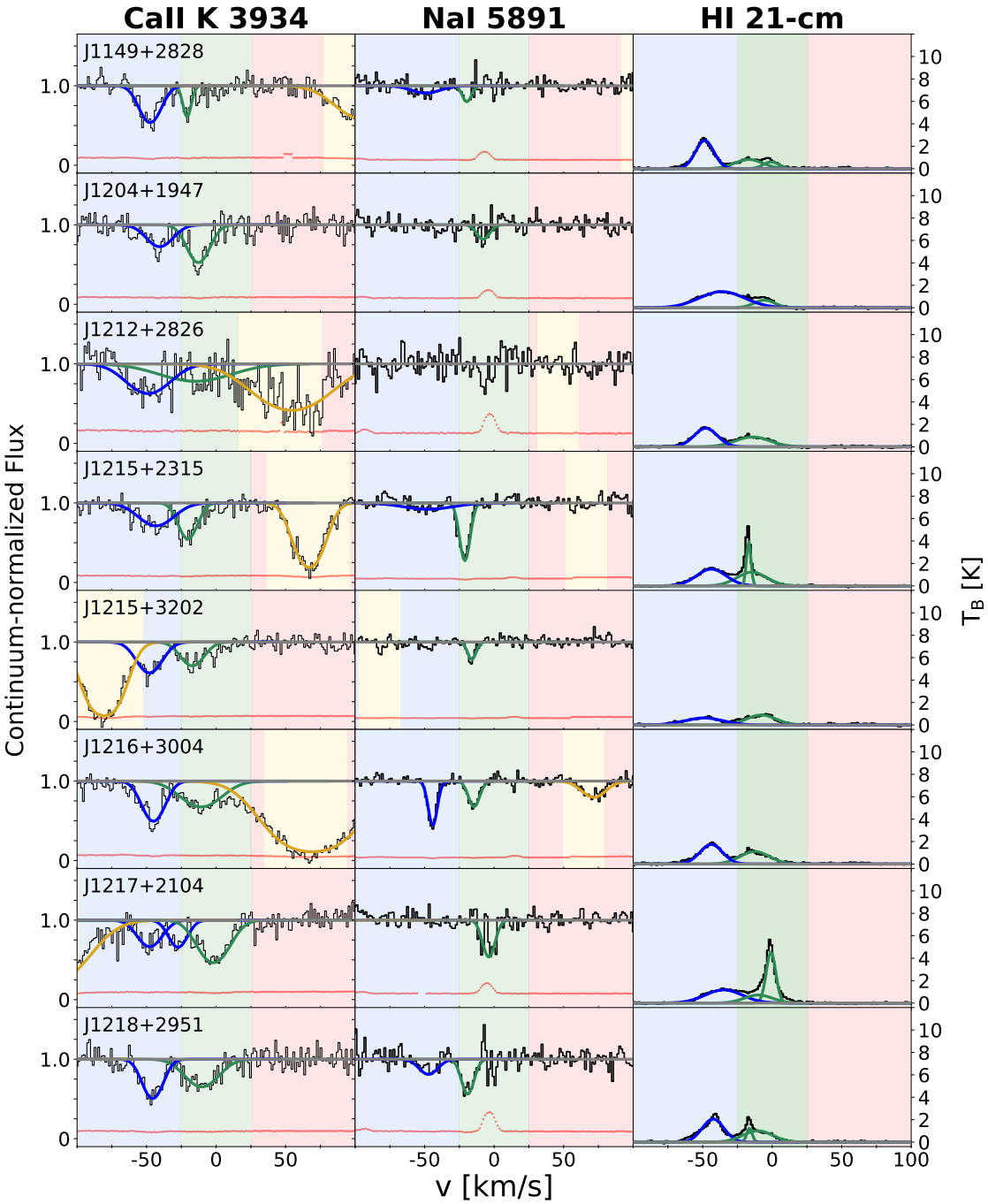

Figure 2.8.1: The full set of line profile fits, as described in Figure 2.6.

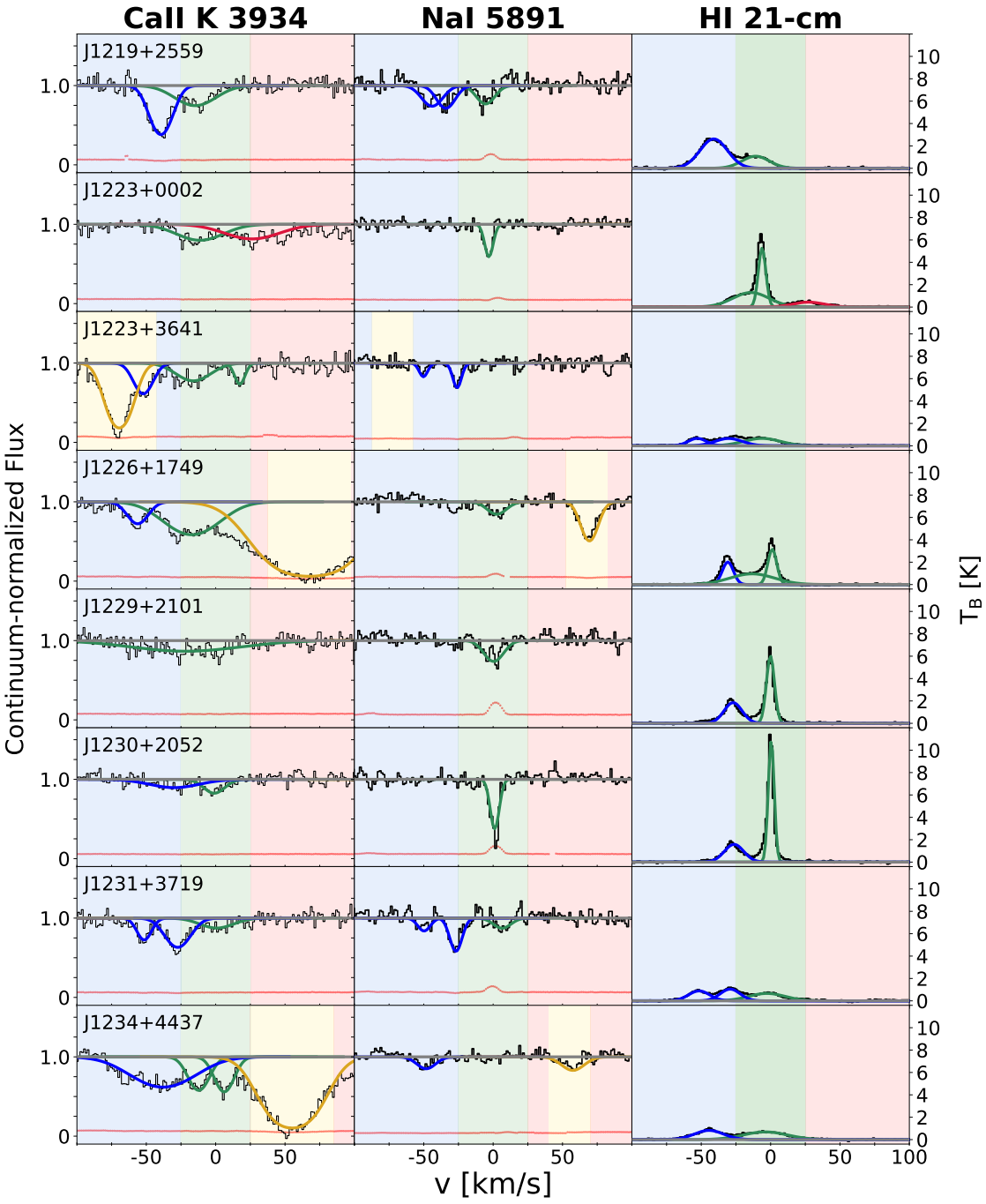

Line profile fits (continued)

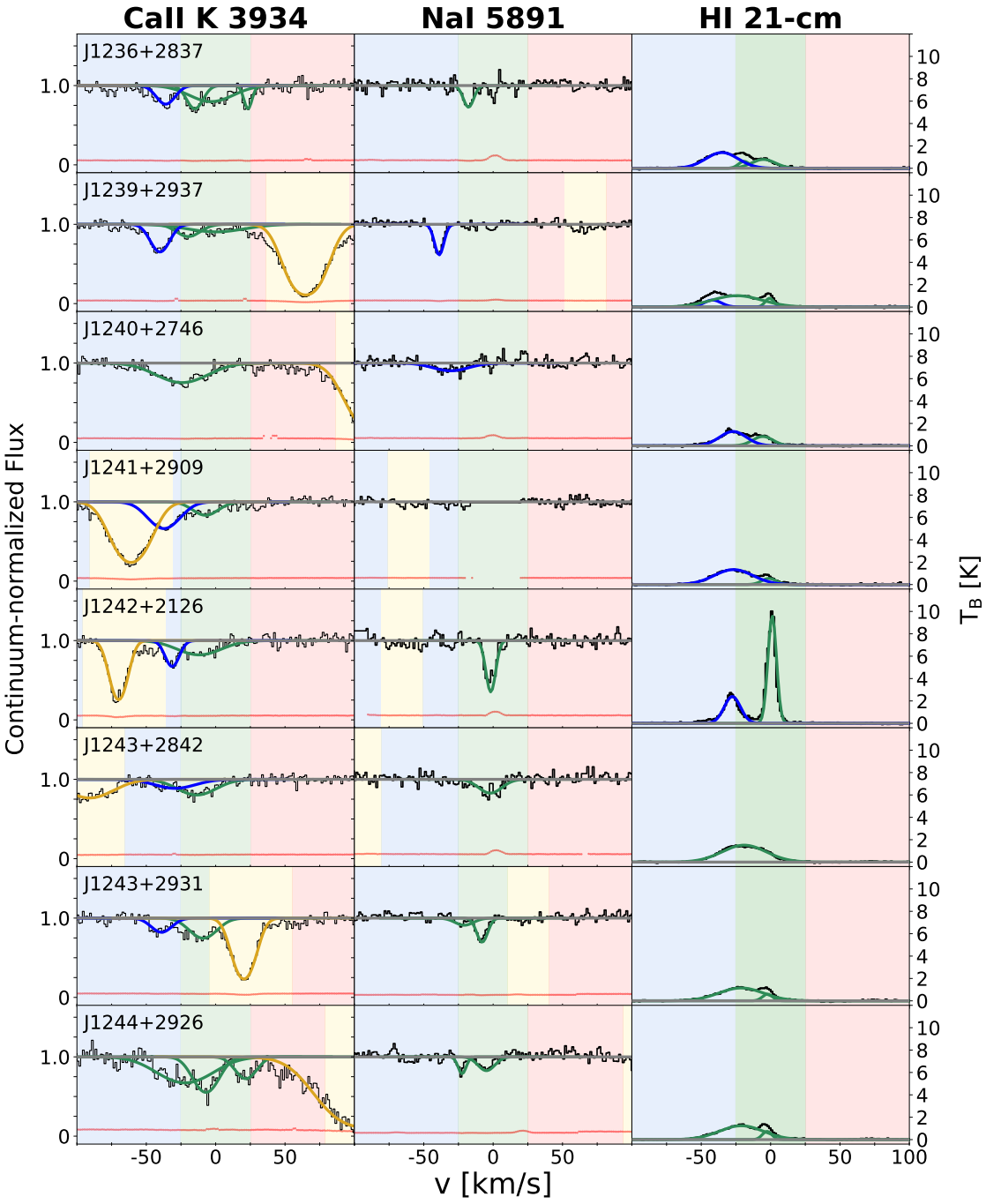

Line profile fits (continued)

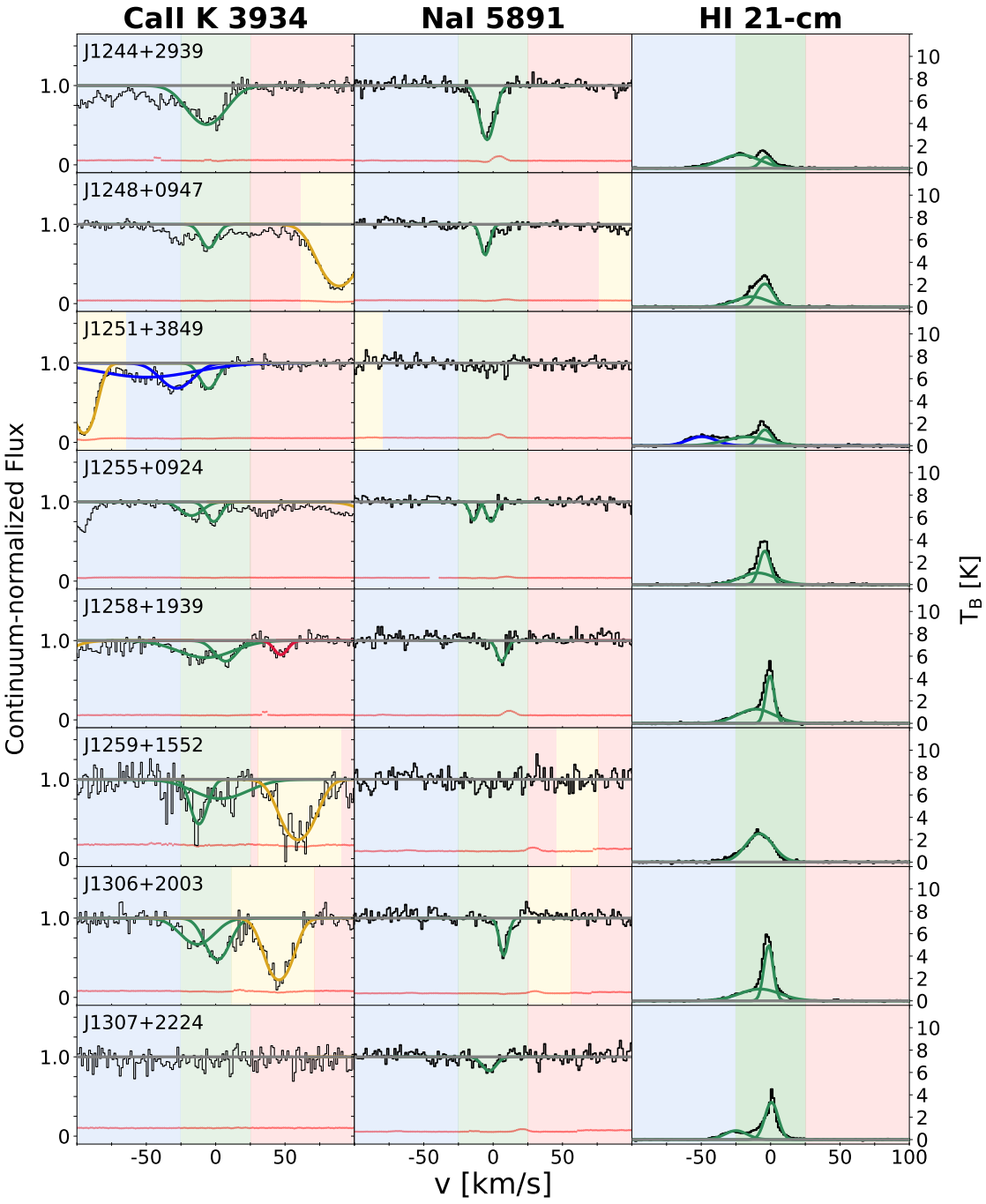

Line profile fits (continued)

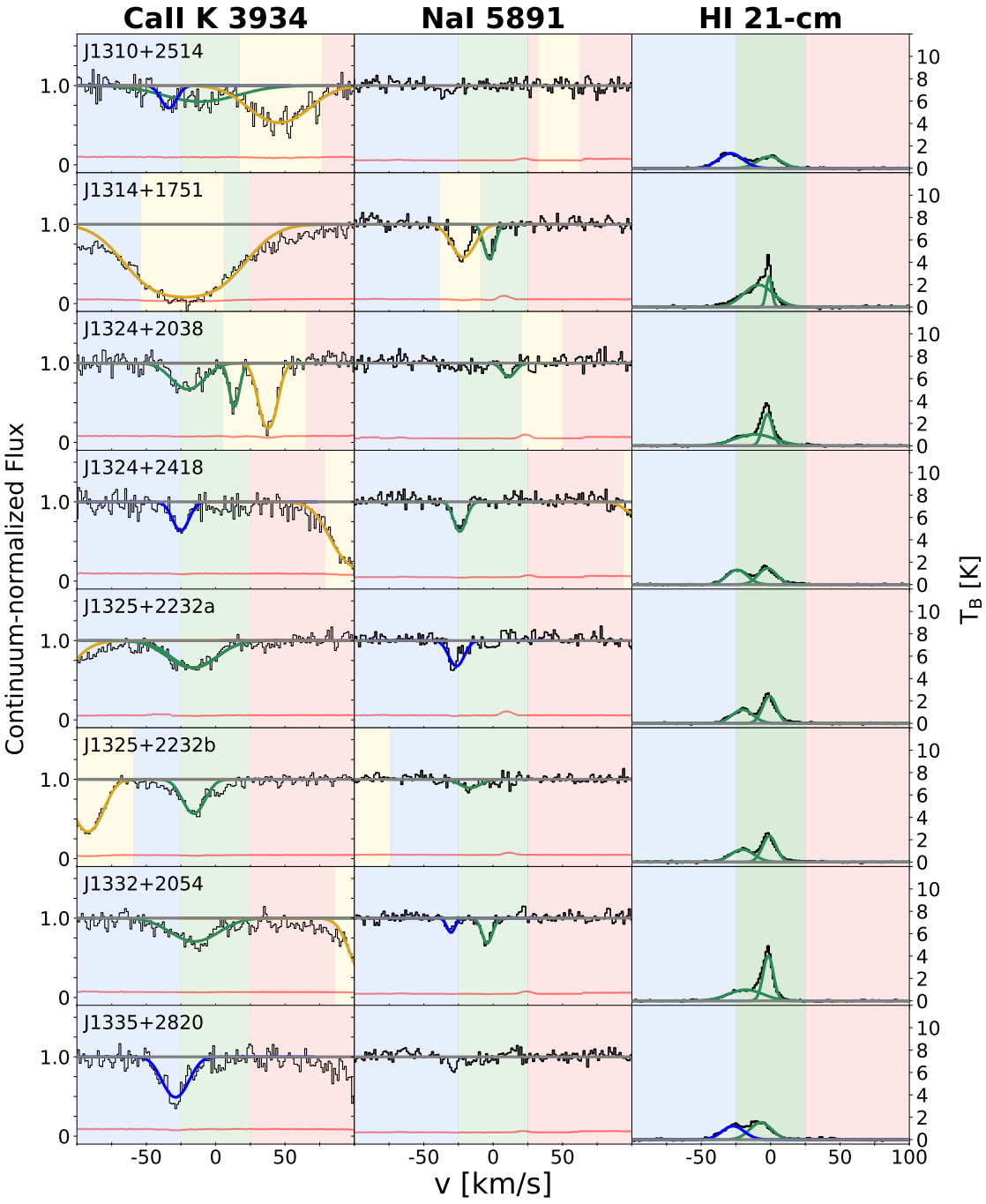

Line profile fits (continued)

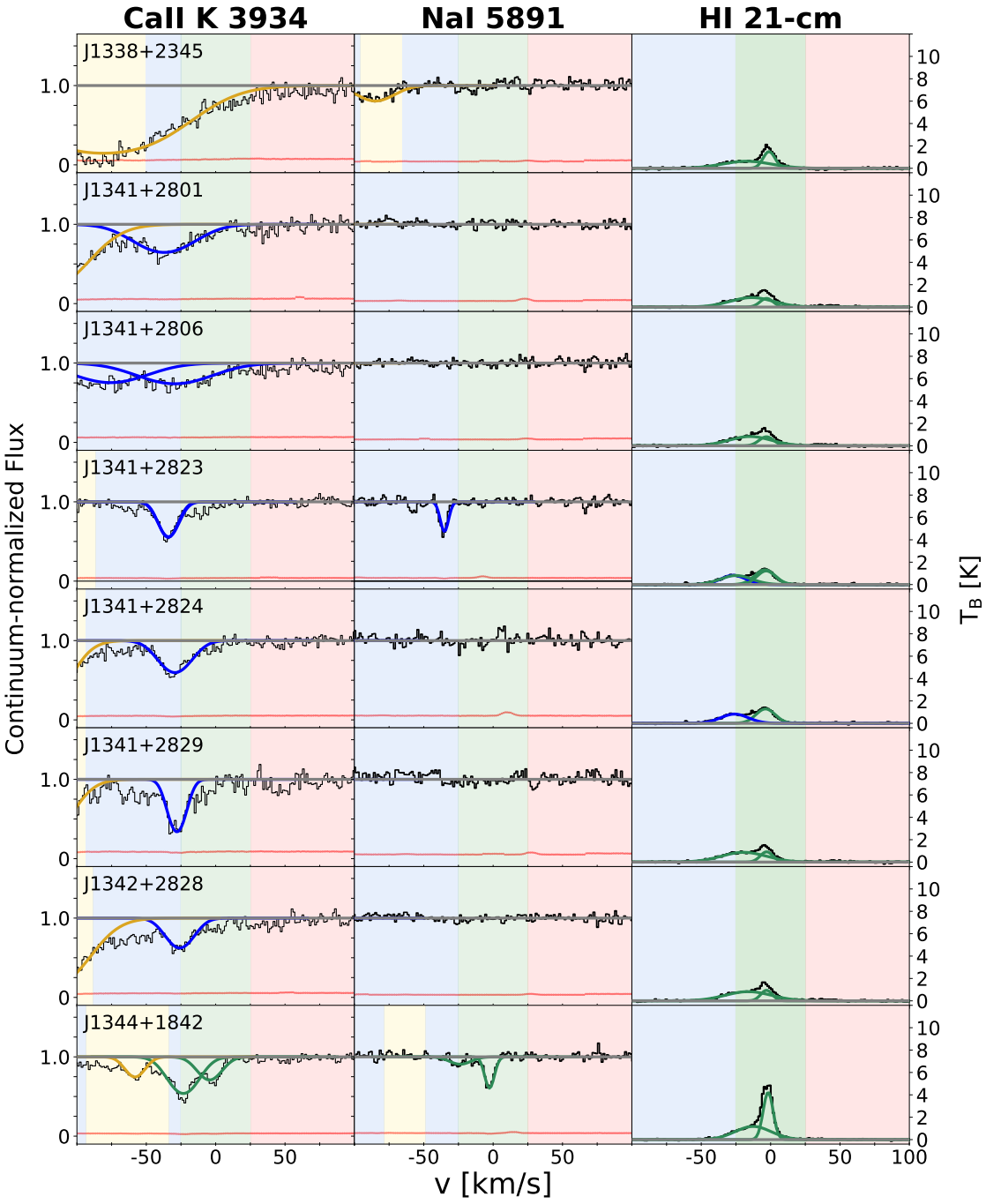

Line profile fits (continued)

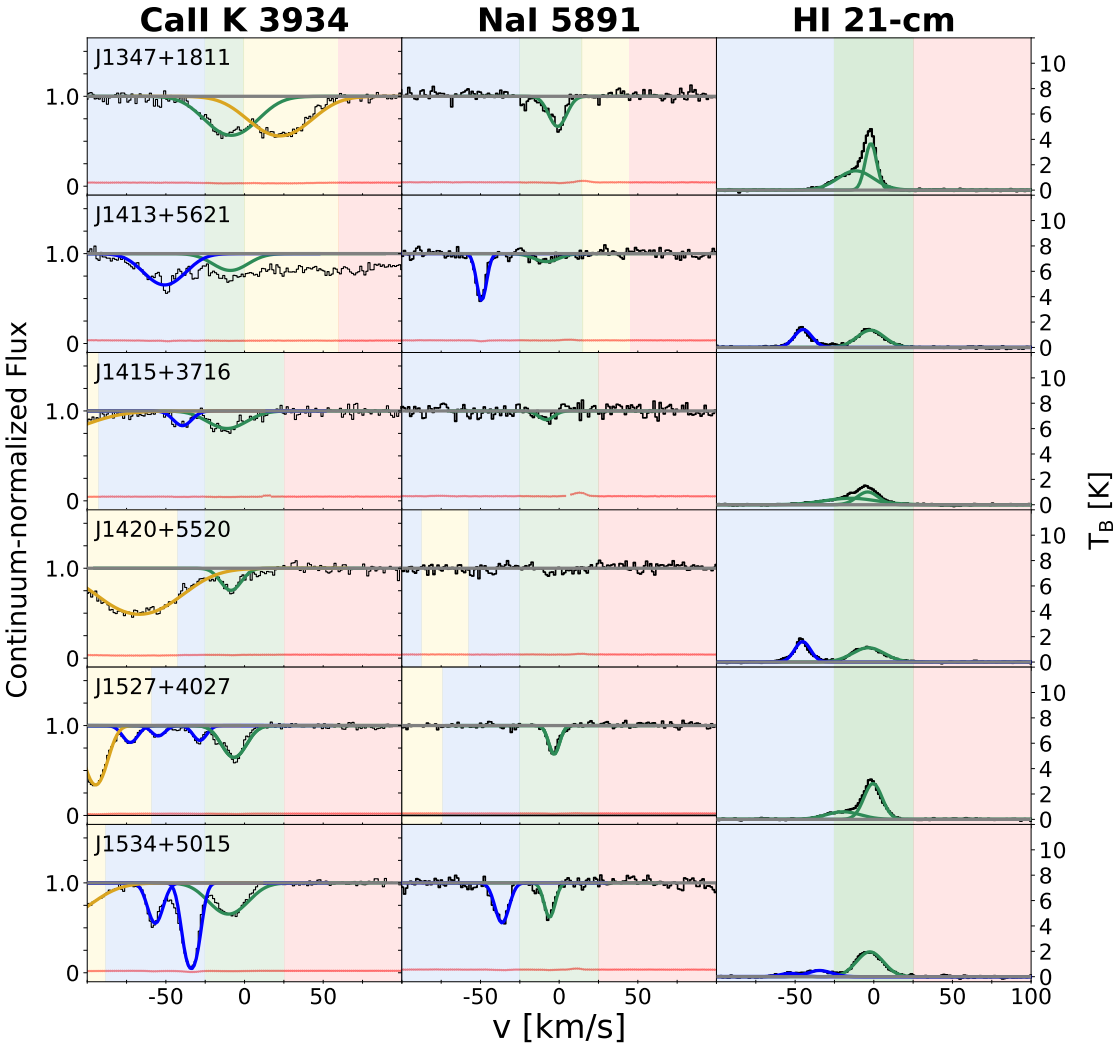

Line profile fits (continued)

Chapter 3

THE QUASTAR SURVEY: DETECTING HIDDEN LOW-VELOCITY GAS IN THE MILKY WAY'S CIRCUMGALACTIC MEDIUM

Portions of this chapter were originally published in collaboration with Jessica K. Werk, Joshua E.G. Peek, Yong Zheng, and Mary Putman in the May 2021 edition of the Astrophysical Journal (Bish et al., 2021, ApJ*, Vol. 906, 120; 2021 © American Astronomical Society, DOI: 10.3847/1538-4357/abccca), and are reproduced below with the permission of the American Astronomical Society.*

Chapter Summary

From our position embedded within the Milky Way's interstellar medium (ISM), we have limited ability to detect gas at low relative velocities in the extended Galactic halo because those spectral lines are blended with much stronger signals from dense foreground gas. As a result, the content of the Milky Way's circumgalactic medium (CGM) is poorly constrained at $|v_{\rm LSR}| \lesssim 150$ km s^{-1}. To overcome this complication, the QuaStar Survey applies a spectral differencing technique using paired quasar-star sightlines to measure the obscured content of the Milky Way's CGM for the first time. We present measurements of the C IV doublet ($\lambda\lambda$ 1548, 1550 Å), a rest-frame UV metal line transition, detected in *HST*/COS spectra of 30 halo-star/quasar pairs evenly distributed across the sky at Galactic latitudes $|b| > 30°$. The 30 halo stars have well-constrained distances (d≈5-14 kpc), and are paired with quasars separated by $< 2.8°$. We argue that the difference in absorption between the quasar and stellar sightlines originates primarily in the Milky Way's extended CGM beyond ∼10 kpc. For the Milky Way's extended, low velocity CGM ($|v|$ <150 km/s), we place an upper limit on the mean C IV column density of $\Delta{\rm logN}_{\rm LVCGM} < 13.39$ and find a covering fraction of $f_{\rm CIV,LVCGM}({\rm logN} > 13.65) = 20\%$ [6/30], a value significantly lower than the covering fraction for star-forming galaxies at low redshift. Our results suggest either that the bulk of Milky Way's C IV-traced CGM lies at low Galactic latitudes, or that the Milky Way's CGM is lacking in warm, ionized material compared to low-redshift ($z < 0.1$) star-forming galaxy halos.

3.1 Introduction

Over the past decade, groundbreaking work with the Cosmic Origins Spectrograph (COS) on the Hubble Space Telescope (HST) has shown that the circumgalactic medium (CGM) around Milky Way-like galaxies is the hiding place of most galactic baryons and metals and an important source of fuel for star formation (Werk et al., 2014; Peeples et al., 2014; Tumlinson et al., 2017). This tenuous, predominantly-ionized halo gas is notoriously difficult to detect in emission because of its low density, so it is most commonly measured in absorption along quasar sightlines that pierce nearby galaxy halos (e.g. Bahcall & Spitzer, 1969; Bergeron, 1986; Lanzetta et al., 1995; Prochaska et al., 2011; Werk et al., 2013). Extragalactic absorption-line studies are useful for investigating average global properties of the CGM, but the limited availability of quasar sightlines means we can rarely make more than one or two measurements within a single galaxy halo outside the Local Group. The Milky Way, with hundreds of sightlines that pierce its halo, provides a unique opportunity to characterize the structure and kinematics of our own CGM better than that of any other galaxy in the universe.

Observations of CGM gas reveal a complex structure and distribution which can be explained by various physical models. On the largest scales, the CGM may be distributed spherically with a steeply declining density profile (e.g. Liang & Chen 2014; Werk et al. 2014); it may form a thick, rotating, toroidal structure (e.g. Stewart et al. 2011; Bregman et al. 2018); or it may be composed of large shocked sheets of material flowing through the halo (McQuinn & Werk, 2018). The Northern and Southern Galactic skies are quite different in their known CGM components, which may indicate an overall asymmetry (Putman et al., 2012; Bordoloi et al., 2017). Additionally, smaller-scale structures, such as clouds and thin filaments are known to populate the CGM (e.g. Ben Bekhti et al., 2009; Saul et al., 2012; Stocke et al., 2013; McCourt et al., 2015; Stern et al., 2016; Bish et al., 2019).

While our own Galaxy was the first in which we detected extraplanar material (Muller et al., 1963), we have yet to make a definitive measurement of the column density of the

Milky Way's CGM because global measurements of Galactic halo properties are confounded by our location within the Milky Way's disk. Any attempt to isolate signals from the Milky Way's CGM will be hampered by blended foreground absorption from the ISM in which we are embedded (see Zheng et al. 2015). In particular, Galactic foreground gas in the disk obscures halo gas with similar relative velocities.

In order to avoid foreground contamination from the low-velocity material in the disk, Milky Way CGM studies typically target high-velocity gas ($|v| \gtrsim 100$ km/s) and do not constrain lower-velocity material beyond the inner ∼10 kpc of the halo. Ionized high-velocity clouds are ubiquitous, covering 65-90% of the sky at typical distances of 5-15 kpc (Fox et al., 2006; Collins et al., 2009; Shull et al., 2009; Lehner et al., 2012; Richter, 2017). But despite their abundance, observations indicate that high- and intermediate-velocity clouds likely make up a small fraction of the Milky Way's total halo mass (Putman et al., 2012), and point to the possibility that considerable material is hidden at lower velocities in the extended Galactic CGM.

In other low-redshift galaxies, the average velocity of galactic CGM absorption generally centers around 0 km/s relative to the host galaxy's systemic velocity (e.g. Tumlinson et al., 2013; Werk et al., 2016). Metal-enriched gas is detected in external L* galaxies moving at low relative velocities out to their virial radii (e.g., Liang & Chen, 2014; Werk et al., 2014; Lehner et al., 2015; Burchett et al., 2016). In the COS-Halos survey of low-redshift galaxy halos, ∼ 90% of the total CGM column density within ±600 km/s of the galaxy systemic velocity was found at $|v| < 100$ km/s (Tumlinson et al., 2013; Werk et al., 2014). Kinematic analysis of warm gas signatures in the quasar absorption-line survey COS-GAL also shows that a substantial portion of the CGM is likely hidden at $|v| < 100$ km/s (Zheng et al., 2019). In the recent CGM^2 survey, the majority of the HI column density detected in absorption around $z < 0.48$ galaxies lies within ±250 km s^{-1} of the galaxy systemic velocity, despite a velocity window of 1000 km s^{-1} (Wilde et al., 2021). Additionally, Martin et al. (2019) find that the velocity of low-ionization gas around nearby galaxies is tied with the rotation of the disk out to radii of ∼70 kpc. If the Milky Way is similar to other star-forming galaxies at

low redshift, these observations further reinforce the evidence suggesting that a significant fraction of Galactic baryons are yet to be detected in the low-velocity Galactic CGM.

Simulations of Milky Way analogs also broadly agree that a significant fraction of circumgalactic baryons are moving at low velocities. The FOGGIE simulations, which focus on resolving the CGM around galaxies with extreme spatial and mass resolution, show with mock observations that the strongest absorption is confined to within 200 km/s of the systemic velocity (Peeples et al., 2019; Zheng et al., 2020). Other synthetic observations of a MW-mass galaxy generated from the high-resolution cosmological simulation Enzo also predict that $\sim 65\%$ of the Milky Way's CGM mass at Galactic latitudes $|b| > 20^{\circ}$ is hidden at low-intermediate velocities ($|v| < 100$ km/s) for all gas phases, and that the warm-hot component (10^5 K $< T < 10^6$ K) is primarily moving at $|v| < 150$ km/s (Zheng et al., 2015; Joung et al., 2012b).

The C IV doublet is a useful probe of warm ionized gas in galaxy halos because of its strong oscillator strength (Savage & Wakker, 2009) and high covering fraction in the CGM of external galaxies (Keeney et al., 2013; Liang & Chen, 2014). In low-redshift galaxies that span a wide range of stellar mass ($9.5 < \log\,(M_*/M_{\odot}) < 11$), estimates of log $\mathrm{N_{CIV}}$ [$\mathrm{cm^{-2}}$] range from 13.5 - 14.5, with a covering fraction of $\sim$50% out to half the virial radius for $\log \mathrm{N_{CIV}} > 13.5$ $\mathrm{cm^{-2}}$ (Bordoloi et al., 2014b; Burchett et al., 2016). Using conservative ionization fraction arguments which take the maximum fraction of carbon that presents as C IV, $\sim$30%, for both photo- and collisionally-ionized gas, such measurements imply $> 10^6 M_{\odot}$ of carbon sits in the CGM of external galaxies. For sub-L* galaxies with stellar masses $10^{8.5} \lesssim \mathrm{M^*\ [M_{\odot}]} \lesssim 10^{10}$, this estimated CGM carbon mass amounts to 50% to 80% of the total ISM carbon mass (Bordoloi et al., 2014b).

Measurements of the Milky Way's CGM are needed at all velocities in order to directly probe the baryonic mass of the Milky Way, test the expectations from cosmological simulations, and compare the Milky Way to other galaxies. Motivated by this need, we present QuaStar: an absorption-line survey designed to enable the first measurements of low-velocity CGM gas in the Milky Way that have been isolated from contaminating foreground absorption.

The QuaStar survey follows recent work examining ionized CGM gas absorption in the Milky Way using *HST*/COS archival spectra of hundreds of quasars (Richter, 2017; Zheng et al., 2019; Qu et al., 2020). Richter (2017) provides a list of quasar pairs with $< 1^\circ$ sightline separation and highlights the differences in their Si II , Si III, C II , and C IV absorption profiles. Our preliminary investigation of sightlines included in the Zheng et al. (2019) COS-GAL sample showed that the variation of C IV for 20/26 quasar pairs with angular separation $< 2^\circ$ is consistent with noise. With this study we build on the discovery that C IV , sensitive to warm ($T > 10^{4.5}$ K) CGM gas, is found in large coherent structures and exhibits little variation in column density between sightlines at small separation (Werk et al., 2019).

Specifically, QuaStar uses close pairs of quasar and halo star sightlines to account for the foreground gas absorption that blends with and obscures our view of low-velocity gas in the Milky Way's CGM. The experimental design of QuaStar relies on the expectation that C IV -bearing gas in the inner halo of the Milky Way is homogeneous on the angular scales probed by the star-quasar sightline pairs – an assumption that we seek to evaluate as we carry out the analysis. If both quasar and stellar spectra have the same amount of C IV absorption due to foreground gas, then the difference in total C IV absorption between them likely originates in the Milky Way's extended CGM, revealing its unobscured content for the first time.

In this chapter we focus on the first isolated measurement of N_{CIV} in the extended Milky Way halo ($R_{CGM} \gtrsim 10$ kpc) for 30 sightline pairs across the sky, and use our findings to place the Milky Way's CGM content in a broader extragalactic context. §3.2 expands on the details of the QuaStar survey design, sample, and data. §3.3 describes our analysis methods for obtaining column density measurements and applying a "spectral differencing" technique to isolate low-velocity C IV in the Milky Way's CGM. We present the results of our ISM-subtracted C IV measurements in §3.4, and discuss the implications of our findings in §3.5. Finally, we conclude with a summary in §3.6.

3.2 Observations

3.2.1 Survey Design

The QuaStar survey consists of *HST*/COS G160M spectroscopy of 30 UV-bright halo stars at distances $d \sim 5 - 14$ kpc paired with archival G160M spectra of quasars separated by less than 2.8° on the sky (Figure 3.2.1 & Table 3.1). Quasar sightlines probe the extended CGM, while halo star sightlines span foreground absorption from the disk and the disk-halo interface. Thus, the survey design allows absorption along the stellar sightline (originating from foreground gas associated with the disk) to be subtracted from absorption along the quasar sightline (originating from both disk and CGM gas), in principle isolating absorption signatures of gas beyond the disk-halo interface.

3.2.2 Sample Selection

To ensure that foreground ISM contamination could be subtracted successfully, we selected a sample of halo stars that are (1) FUV-bright (FUV magnitude < 17.5), (2) well above the Galactic plane ($|z| > 6$ kpc) and (3) close on the sky (< 2.8°) to quasars with well-detected rest-frame C IV. The disk-halo interface has been suggested to have a scale height of ∼3 kpc in C IV (Savage & Wakker, 2009), so we targeted stars >6 kpc above the Galactic plane. Assuming an exponential density profile along the z-axis for C IV-bearing gas, a halo star at z ∼6 kpc allows us to subtract out $\gtrsim$86% ($= 1 - e^{6/3}$) of absorption from the obscuring disk-associated material.

Although sightlines at lower Galactic latitudes would be sensitive to CGM features in the extended plane of the disk, UV-bright quasar lines of sight at low Galactic latitudes are rare due to significant extinction from the Milky Way disk. Generally, sightlines at higher Galactic latitudes are less affected by Galactic differential rotation and generally must pass through less foreground ISM substructure in order to probe gas at >6 kpc above the disk. As a result, we chose QuaStar lines of sight to lie at $|b| > 30°$. We sampled the sightlines as evenly as possible in Galactic longitude and within our range of Galactic latitudes. In

selecting lines of sight, we did not avoid the well-studied, ionized Magellanic System (Fox et al., 2014), the bulk of which lies at d $\gtrsim$ 50 kpc and $|v_{\rm LSR}| > 100$ km s^{-1}. We discuss its possible contribution to our C IV measurements throughout the manuscript, and sightlines that intersect HI associated with the Magellanic System are labeled "MS" in Figure 3.2.2 and Table 3.1.

The stellar sightlines for QuaStar are blue horizontal branch halo stars (BHBs), which have little scatter in their absolute magnitudes and generally exhibit FUV-bright continua with few stellar absorption features (Deason et al., 2011; Werk et al., 2019). To construct a parent sample of halo stars, we started with the Smith et al. (2010) catalog of BHB candidates. This catalog was itself constructed from photometric SDSS observations, using a machine learning method trained on the spectroscopically-confirmed catalog of Xue et al. (2008). We then matched the stars to *Gaia* DR2 for parallaxes (Gaia Collaboration et al., 2016, 2018). While *Gaia* does not have the parallactic sensitivity to robustly measure the distance to these halo stars, the primary interlopers into our color selection are nearby disk stars, which *Gaia* parallaxes allow us to reject. We found that these interloper disk stars comprised roughly 20% of the original sample.

The SDSS sample is largely limited to the Northern sky, so for Southern targets we turned to the SkyMapper survey (Wolf et al., 2018). SkyMapper is the only large-area southern survey with accurate u-band photometry, a critical filter for selecting BHB stars. We found a small subset of SDSS BHB stars from Smith et al. (2010) that are also detected in SkyMapper. These served as the training set for a k-nearest neighbors algorithm, which we used to predict the BHB probability of the rest of the Sky Mapper stellar sample based on colors. Using the same *Gaia* method to reject interlopers we found the highest likelihood BHBs (>90%) subsample to be 10% disk stars, which we rejected.

We then took this decontaminated joint SDSS/Sky Mapper parent sample of halo BHB stars and found all stars with well-measured FUV magnitudes from GALEX (Bianchi et al., 2017). We took the subset of these stars brighter than FUV = 18.5 and cross-matched it with the COS-GAL sample of quasars (Zheng et al., 2019) with well-measured C IV Galactic

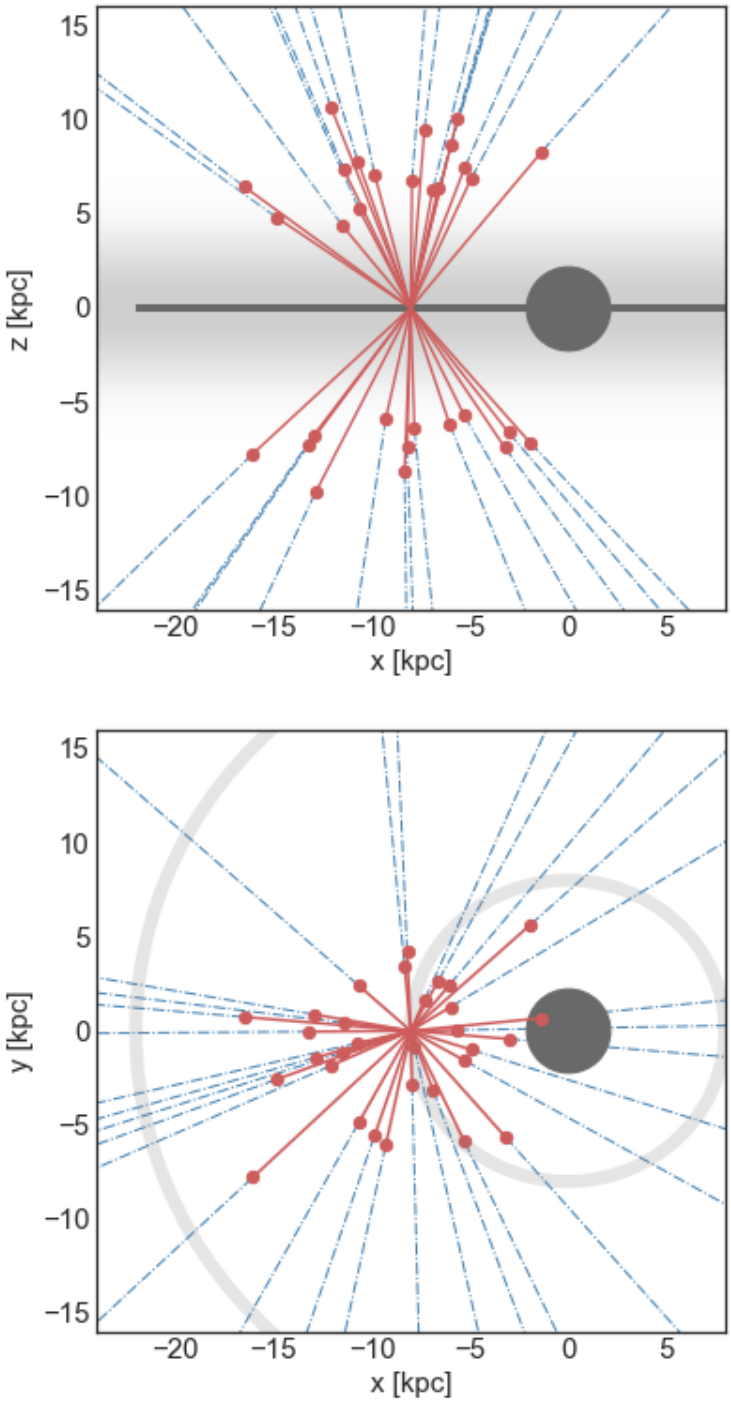

Figure 3.2.1: QuaStar survey design. Spatial distribution of close star-quasar sightline pairs ($< 2.8°$ separation) in the QuaStar survey, projected onto the x-z (top) and x-y (bottom) planes of the Milky Way disk. Sightlines toward halo stars are shown in red, and the blue dashed lines show the corresponding sightlines to the paired quasar. The Galactic disk and bulge are shown in dark grey for reference. In the top panel, the approximate extent of the disk-halo interface is shaded light grey (Savage & Wakker, 2009). In the bottom panel, lines of constant Galactocentric radius are shown in grey.

absorption, requiring pairs to be closer than 3°. Each of the archival quasars paired to these stars was examined to look for redshifted lines contaminating the Galactic C IV absorption, and one quasar was rejected for having saturated contamination. From this list we culled out any redundant stars that significantly overlapped, with a bias toward removing fainter stars that would be time consuming to observe. Finally, we included three sightline pairs from an initial pilot study that made use of preexisting observations of stars (Lehner & Howk, 2011) and quasars (Zheng et al., 2019). One sightline pair (quasar LBQS-0107-0232 & star J0111-0011) was later excluded from analysis because Lyman-alpha forest prevented accurate measurement of Milky Way absorption features. The final list is composed of 30 BHB star-quasar pairs which provide a roughly even sampling of the high-latitude ($b > 30°$) sky (Figure 3.2.1).

3.2.3 Quasar & Stellar Spectra

QuaStar includes both stellar and quasar spectra observed with the G160M grating on Cosmic Origins Spectrograph (COS; Froning & Green, 2009; Green et al., 2012) on the Hubble Space Telescope. The stellar spectra were obtained as part of a Cycle 26 HST Large Program (PID #15656), and the archival quasar spectra were originally obtained as part of a number of different programs with varying science goals. We detect far-UV absorption features from metal ions such C IV ($\lambda\lambda$ 1548 Å, 1550 Å) and Si IV ($\lambda\lambda$ 1393 Å, 1402 Å), which trace warm ionized material. Both our newly-observed stellar targets and their archival quasar pairs in the Hubble Spectral Legacy Archive (HSLA) were observed at a central wavelength of 1577 Å , with a wavelength range of 1383-1754 Å and a velocity resolution of 18 $\mathrm{km\,s^{-1}}$.

The stellar spectra were co-added with 3-pixel binning using the IDL routine `COADD_X1D` (v3.3) developed by Danforth et al. (2016). Co-added quasar spectra were obtained directly from the HSLA and rebinned to match the stellar spectra using the SpectRes spectral resampling tool (Carnall, 2017). Co-author Yong Zheng performed a co-added flux comparison among `COADD_X1D` and HSLA data for a set of bright UV stars, finding that despite their

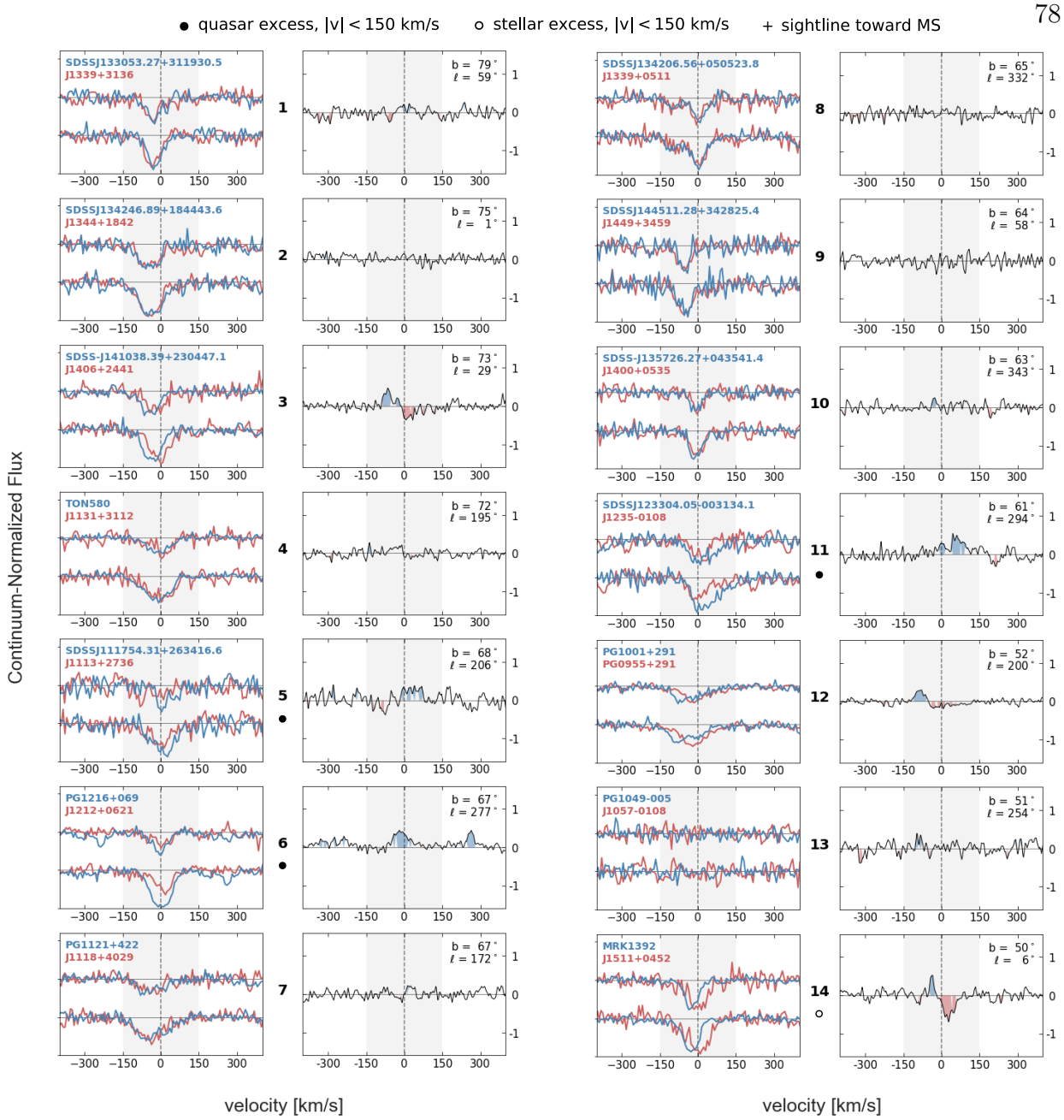

Figure 3.2.2: DIFFERENCE SPECTRA. *Left columns:* C IV ($\lambda\lambda$ 1548, 1550 Å) absorption doublets in the contamination-corrected, continuum-normalized star-quasar spectrum pairs. Velocities are given in the LSR frame. For each sightline pair, spectra and target names are shown in red for the star and blue for the quasar. The stronger 1548 Å line is shown on bottom with the 1550 Å line above it. Since the doublet lines are separated by ∼500 km/s in velocity space, some features which appear at positive velocities relative to the 1548 Å line are also visible at negative velocities relative to the 1550 Å line. The sightline pairs are labeled with ID numbers, which are listed in Table 3.1 and referenced throughout this work. A symbol below the ID number identifies sightline pairs with significant excess quasar absorption (●) or stellar absorption (○) at $|v| < 150$ km/s. Sightlines in the direction of the Magellanic System are labeled with a '+' symbol. *Right columns:* Difference spectrum showing the average excess quasar absorption for the doublet lines shown in the left column (quasar absorption - stellar absorption). A value of 0 means the normalized flux of the star and quasar are identical, and a value of ±1 corresponds to an excess equal to the continuum level. In order to highlight features that are inconsistent with noise, regions of the difference spectrum where the excess absorption is greater than the flux error for both lines in the doublet are shaded blue or red for quasar and stellar excess, respectively. In both columns, the grey shaded region shows the 150 km/s 'low-velocity' window within which absorption features were measured.

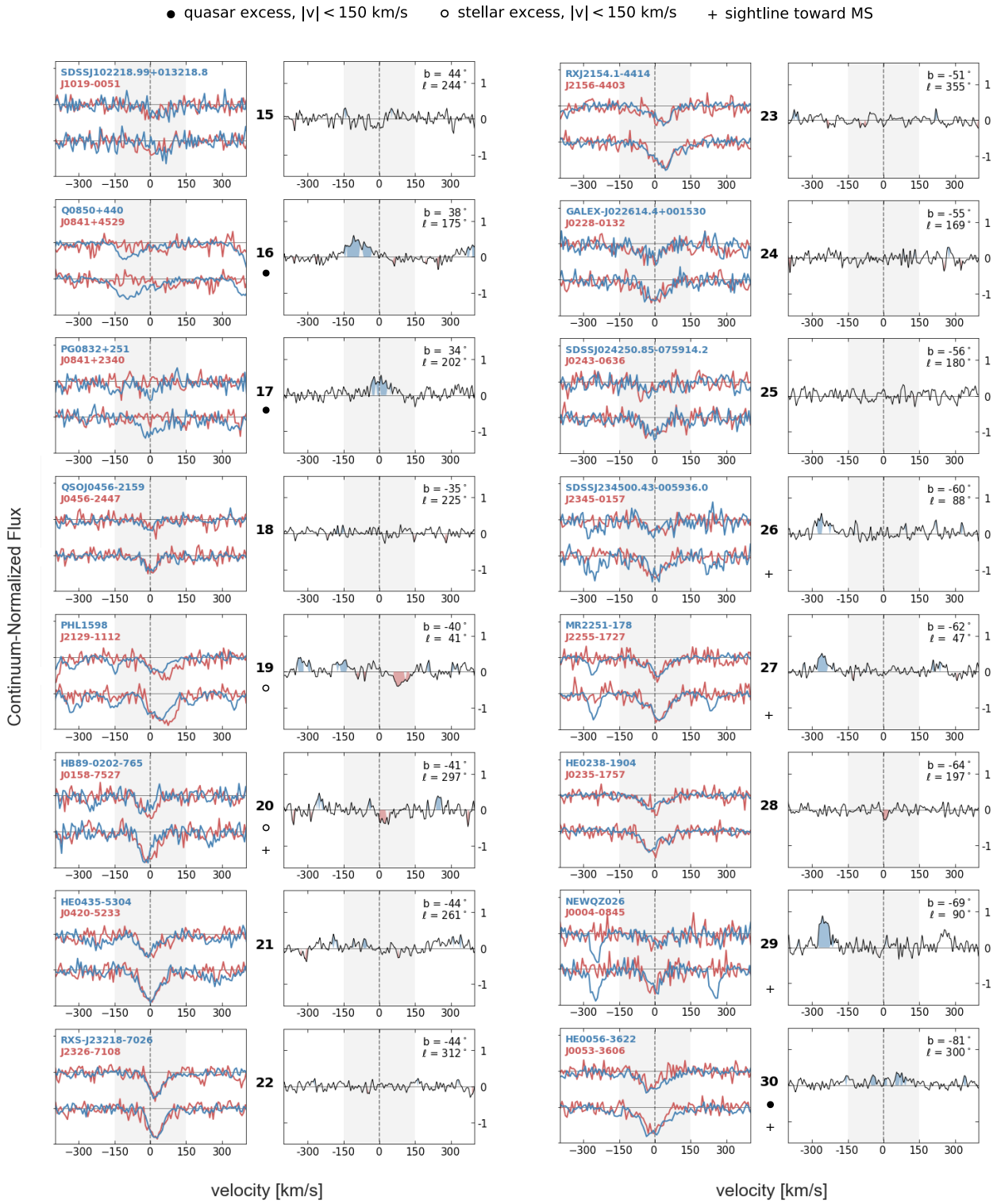

Difference Spectra. (continued)

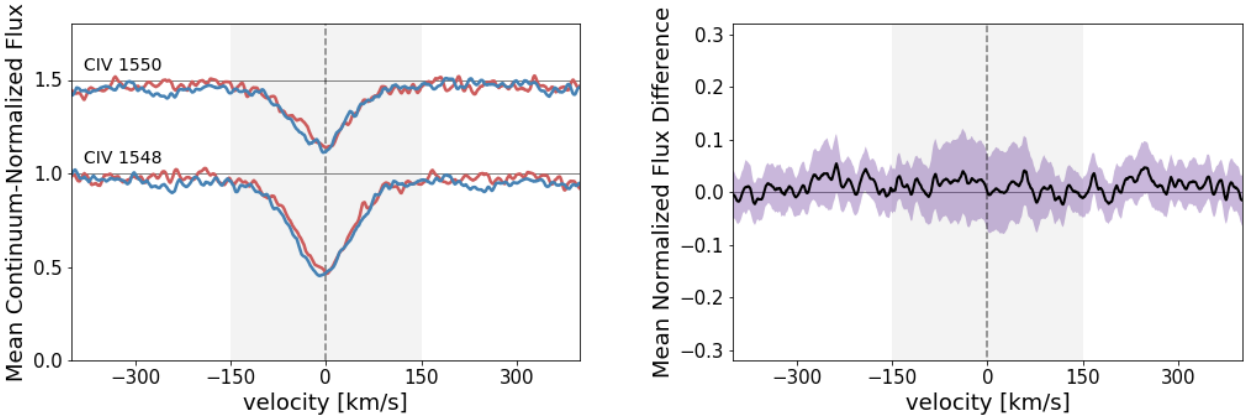

Figure 3.2.2: The bulk of C IV in the Milky Way sits close to the disk at low velocities. Mean C IV absorption profiles (*left*) and difference spectra (*right*) for all 30 individual sightline pairs shown in Figure 3.2.2. The low-velocity ($|v| < 150$ km s^{-1}) measurement window used in this work is shaded grey. The left panel shows the stacked C IV ($\lambda\lambda$ 1548, 1550 Å) doublet profiles for all quasar sightlines in blue and stellar sightlines in red. In the right panel, the corresponding stacked difference spectrum is shown with the standard error on the mean shaded purple. The fluxes are normalized identically in both panels, although the right panel displays a much smaller flux range.

slightly different algorithms the spectral co-addition routines from `COADD_X1D` and HSLA yield similar line profiles and coadded flux levels (Y. Zheng et al. 2020, private comm.). This check assures that the stellar and quasar spectra comparison does not suffer significant systemic errors. After spectra were binned and co-added, continuum fitting was performed for both stars and quasars using the `linetools` package[1], an open-source code for analysis of 1D spectra.

In order to enable accurate measurement of the C IV column density down to a limit consistent with that of low-redshift CGM surveys (log $N_{CIV} \gtrsim 13.5$ cm^{-2}), we obtained COS spectra of stellar sightlines with signal-to-noise of S/N $\gtrsim$ 10 over the full spectrum. The stellar COS spectra have $14.0 <$ S/N < 43.3 at $\lambda = 1550$ Å, with a median value of 16.5. The quasar spectra have $5.6 <$ S/N < 29.5 at $\lambda = 1550$ Å, with a median value of 14.2. For reference, a S/N of $\sim$15 at $\lambda = 1550$ Å corresponds to a median 2σ upper limit (e.g. for non-detections) of log $N_{CIV} \lesssim 13.20$ cm^{-2} over a 50 km/s window. As we will discuss below,

[1]https://github.com/linetools/linetools

our difference spectra require us to measure features over two larger velocity ranges, which in turn impacts our effective sensitivity limit for the column density difference measurement. Specifically, we will consider all material within $\pm$150 km s^{-1} and $\pm$300 km s^{-1} of the local standard of rest; these windows carry an effective 1σ sensitivity limit to Δ log N_{CIV} of 13.39 and 13.56 cm^{-2}, respectively. The sensitivity limits for the difference measurements are explained in more detail in §3.3.3.

3.3 Analysis

3.3.1 Contamination Correction

Once data reduction was complete we identified and corrected for contaminating absorption features, which were present in 16 quasar spectra and 17 stellar spectra. In quasar spectra, where absorption line systems at higher redshifts can overlap with rest-wavelength features of interest, there were a greater number of contamination features per sightline and those features had larger column densities on average. Contaminating absorption lines intrinsic to the BHB stellar atmospheres were less numerous, and when present, the contaminating absorption was weaker.

In order to distinguish contaminants from Galactic absorption, we used the `PyIGM` `IGMGUESSES` GUI[2] to identify all absorption features within 500 km/s of the C IV ($\lambda\lambda$ 1548, 1550 Å) and Si IV ($\lambda\lambda$ 1393, 1402 Å) doublets and obtain preliminary line profile fits (with velocity v, column density N, and Doppler b parameter b_D). We found that absorption features in the C IV doublet consistently matched one another but Si IV features were frequently saturated, resulting in unreliable column density measurements. For that reason, we focus only on C IV measurements in the body of this paper.

To remove contaminating absorption, the velocity window used to fit each absorption component was determined by eye, and both lines in each absorption doublet were then fit

[2]https://github.com/pyigm/pyigm

simultaneously. This individual inspection allowed us to assign narrow velocity priors for fitting in cases when multiple components were blended. Any remaining absorption features that were not present in both lines of the C IV doublet were considered contaminants. If we found any blended contaminants in quasar spectra, we then identified and fit profiles for all absorption line systems at higher redshifts to identify the contaminating line. Once all absorption components were identified and fit, we adjusted the normalized fluxes of each spectrum using the best-fit line profiles of the contaminants. All subsequent analysis was performed on the resulting contamination-corrected spectra.

3.3.2 Column Densities

We measured column densities using the apparent optical depth method (AODM) with the same `linetools XSpectrum1D` package[3] used for data reduction (see §3.2.3). We measured the C IV ($\lambda\lambda$ 1548, 1550 Å) and Si IV ($\lambda\lambda$ 1393, 1402 Å) doublets, which are both strong and well-defined features in UV COS spectra. However, saturated Si IV features often prevented precise or reliable measurement and we therefore present only the C IV measurements in this work.

We report column densities measured for two velocity windows, which include absorption within 150 km/s and 300 km/s of the Galactic local standard of rest (LSR) for each sightline. In our primary analysis we focus on the $|v| < 150$ km/s window. We choose this velocity range in order to fully capture the low-velocity absorption features we detect while minimizing the potential for including additional noise or contaminating features. Going forward we use the term "low-velocity" to refer to this $|v| < 150$ km/s window unless otherwise specified. In addition, we make the same measurement within a wider $|v| < 300$ km/s window, which includes absorption from the Magellanic System (MS) along some quasar sightlines. If structures similar to the MS exist in external galaxies then they could potentially contribute

[3]https://github.com/linetools/linetools

to CGM column densities measured at low velocity relative to the galaxy, depending on the sightline orientation and corresponding observed radial velocity. We therefore find this wider velocity window useful for comparing our results to column densities of external galaxies in the literature (see §3.5.2 for such comparisons).

3.3.3 Difference Spectra

In order to isolate and measure absorption signatures of CGM gas beyond the disk-halo interface, which is always blended with absorption from foreground gas along the line of sight, we leverage the unique experimental design of QuaStar to correct for the blended foreground absorption. Data included in the archival COS-GAL sample indicates that C IV absorption exhibits no detectable variation between $\sim 80\%$ of sightlines separated by $< 2^{\circ}$ (Zheng et al., 2019); we can reasonably assume that the C IV absorption originating from foreground gas will be consistent between the stellar and quasar spectra in the same fraction of our close sightline pairs (but see O VI analysis of SMC/LMC sightlines by Howk et al. 2002). Therefore, we can measure the absorption from foreground gas along stellar sightlines that extend to the disk-halo interface, and use those measurements to subtract foreground gas absorption along the closely-paired quasar sightlines. We expect that $\sim$20% of paired sightlines will have excess stellar or quasar absorption due to clumpy foreground gas. In theory, the resulting difference spectrum will reveal any remaining C IV absorption originating from Milky Way CGM gas behind the star. We discuss some caveats to these assumptions in §3.5.2.

Figure 3.2.2 displays line profiles of the C IV ($\lambda\lambda$ 1548, 1550 Å) absorption doublet for each paired star (red) and quasar (blue), along with the corresponding difference spectrum for each sightline pair. Each pair is labeled with an ID number that can be referenced in Table 3.1, and a symbol appears below the ID number in cases where the sightline pair has significant excess quasar absorption (•) or stellar absorption (∘) at $|v| < 150$ km/s. Sightlines in the direction of the Magellanic System are labeled with a '+' symbol, regardless of whether excess absorption is detected. The spectra (left columns) are continuum-normalized and

corrected for contamination, and the corresponding difference spectra (right columns) are determined simply by subtracting the stellar flux from the quasar flux. Thus, the difference spectra are positive where absorption along the quasar sightline exceeds absorption along the stellar sightline, and vice versa. The difference spectra in Figure 3.2.2 are shaded where this excess is greater than flux measurement errors, with red shading used for excess stellar absorption and blue for excess quasar absorption.

The mean stacked absorption profile and difference spectrum of the individual sightline pairs in Figure 3.2.2 is presented in Figure 3.2.2. As with the individual sightline pairs, the left panel shows the C IV absorption doublet, with the mean normalized flux for quasars in blue and stars in red. The right panel shows the mean stacked difference spectrum for the 30 sightline pairs. The standard error on the mean, shaded purple, is calculated using the jackknife resampling method, which does not assume a normal distribution or large sample size. The absorption profile in the left panel illustrates that the bulk of the C IV column density we detect in the Milky Way is moving at velocities within 100 $\mathrm{km\,s^{-1}}$ of the local standard of rest. However, the difference spectrum in the right panel is relatively flat and consistent with zero, which suggests that little of the low-velocity C IV lies beyond $d \approx 14$ kpc in the Milky Way's halo. While stacked spectra are useful for getting a sense of global behavior over the whole sky, we caution that they may be misleading. Features of interest that are weak and present in only one direction on the sky may be smoothed out. In a forthcoming paper we will further examine such features and the kinematic information they provide about Galactic features such as rotational lag and gas flows.

If foreground absorption were perfectly homogeneous and identical along both quasar and stellar sightlines in every case, we would not expect to see any stellar excess in the difference spectra. However, as discussed in §3.2, we expect that variation in foreground gas density due to clumpy ISM substructure will result in a significant detection of excess absorption for 20% of our paired star and quasar sightlines. In our sample of 30 sightline pairs, this translates to 3 ± 1 pairs with detectable stellar excess and 3 ± 1 pairs with detectable quasar excess, assuming Poisson noise. We will report both an empirical covering fraction, uncorrected for

this clumpiness factor, and a corrected covering fraction, which excludes three detections assumed to be contamination.

To determine our sensitivity to weak CIV features in the difference spectra, we estimate upper limits on N_{CIV} for each spectrum using the 1σ error on column density measured within a featureless region of the continuum near the C IV ($\lambda\lambda$ 1548, 1550 Å) doublet. The velocity width of the featureless region matches the width of the window used for column density measurements, but the exact location of the featureless region in velocity space was selected by eye to ensure that contaminating lines were excluded from the measurement. These 1σ detection limits are conservative upper limits given the large velocity ranges over which they are measured. The upper limit we report on the difference measurement $\Delta\log N_{CIV}$ in the case of a non-detection, N_{det}, is the two one-sigma upper limits for stellar and quasar sightlines added in quadrature.

3.4 Results

We measure C IV column densities for each individual sightline, and the difference between those column densities for each star-quasar sightline pair. For convenience we define our column density difference measurement of low-velocity C IV in the Milky Way's CGM to be

$$\Delta log N_{LVCGM} \begin{cases} = log(N_q - N_s) & \\ \qquad\qquad if\ \bullet: & |N_q - N_s| > N_{det} \\ & N_q > N_s \\ = -log(N_s - N_q) & \\ \qquad\qquad if\ \circ: & |N_q - N_s| > N_{det} \\ & N_q < N_s \\ < N_{det} & \\ \qquad\qquad if\ \varnothing: & |N_q - N_s| < N_{det} \end{cases}$$

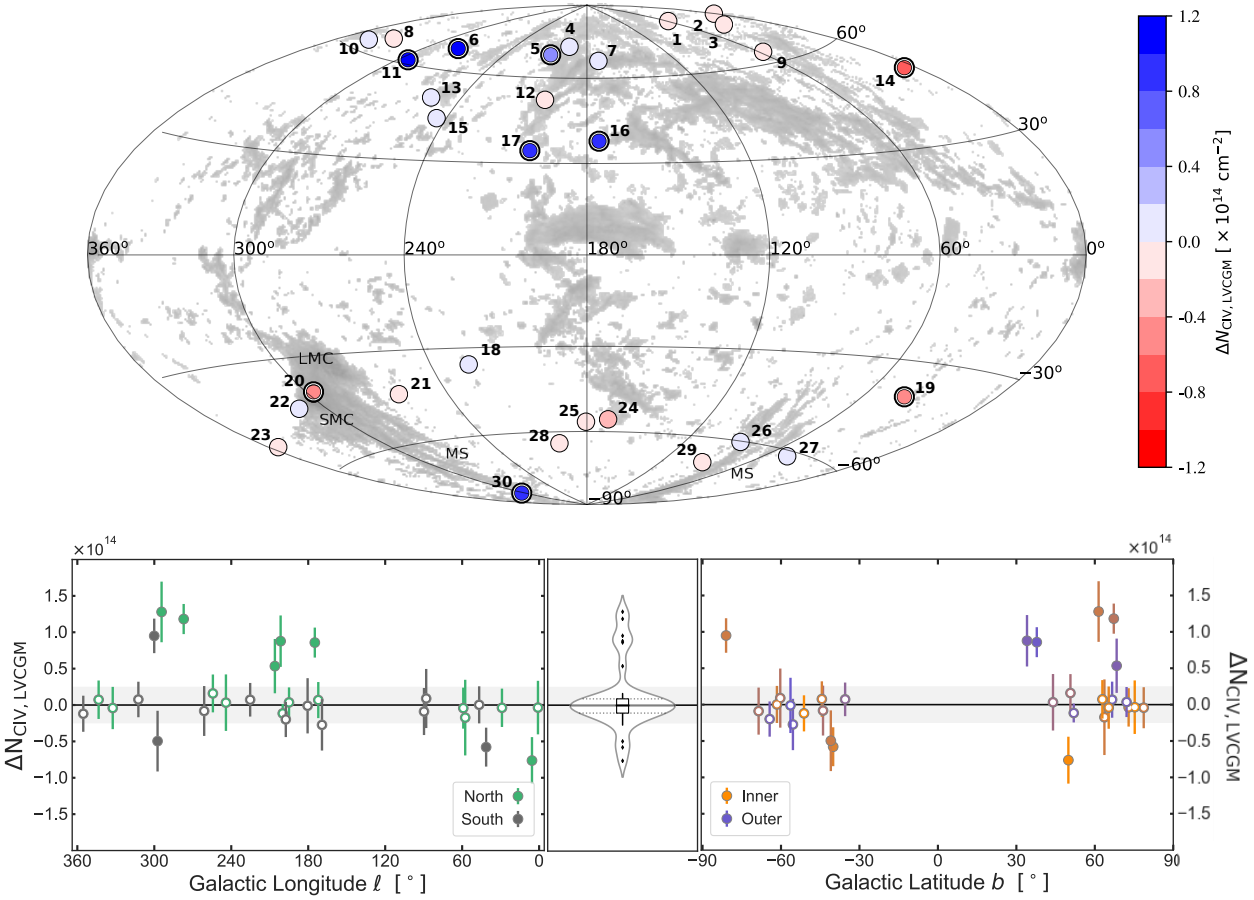

Figure 3.4.1: Low-velocity C IV in the Milky Way's CGM. *Top:* Full-sky map of Galactic high-velocity clouds from the HI4PI survey in grey (HI4PI Collaboration et al., 2016; Westmeier, 2018) overlaid with QuaStar column densities for low-velocity halo gas. Specifically, $\Delta\log N_{LVCGM}$ is the difference in low-velocity ($|v| < 150$ km/s) C IV gas column density between the star and quasar in each sightline pair. Each marker represents one star-quasar sightline pair. Blue markers/positive values indicate an absorption excess along the quasar sightline, which likely originates from the Milky Way's extended CGM. Red markers/negative values indicate absorption excess along the stellar sightline, which is likely due to small-scale foreground fluctuations in C IV column density. Thick marker edges highlight sightline pairs with significant absorption excess. The Magellanic Clouds and Magellanic Stream are labeled for reference. *Bottom:* Column density difference of sightline pairs vs. Galactic longitude and latitude. Here, color represents the galactic coordinates of the sightline pair. Open markers represent measurements below the sensitivity limit. In the left panel, markers are green if a sightline is in the Northern Galactic hemisphere and grey if it is in the Southern Galactic hemisphere; in the right panel, markers are orange if the sightline is towards Galactic center, and purple if it is away from Galactic center. The violin plot in the middle panel shows the distribution, median value, and interquartile range of the C IV column density difference measurement $\Delta\log N_{LVCGM}$. The range of column density measurements that fall below the median sensitivity limit of the sample ($\Delta\log N_{LVCGM} < 13.39$ cm^{-2}) are shaded grey. Notably, the column density difference $\Delta\log N_{LVCGM}$ for most sightline pairs falls below the sensitivity limit, suggesting there is little low-velocity gas in the Milky Way's extended CGM.

where N_q is the quasar sightline column density, N_s is the stellar sightline column density, and the difference measurement sensitivity limit N_{det} is the sensitivity limit of the stellar and quasar spectra added in quadrature, as discussed in §3.3.3. Thus, $\Delta\log N_{\rm LVCGM}$ is the log of the difference in column density for a star-quasar pair, where excess absorption along the quasar sightline gives a positive value, and excess absorption along the stellar sightline gives a negative value. If the column density difference is smaller than the sensitivity limit, then N_{det} places an upper limit on the value of $\Delta\log N_{\rm LVCGM}$. The difference measurement $\Delta\log N_{\rm LVCGM}$ will be negative in cases where there is a small clump or overdensity present along the line of sight to the star that is not in the foreground gas along the quasar sightline. We expect roughly 10% of sightline pairs to have column density excess along the stellar sightline due to differences in foreground gas absorption (see §3.3.3).

We present the results for two velocity windows: one measuring $|v| < 150$ km/s gas (hereafter referred to as "low-velocity"), and a wider $|v| < 300$ km s^{-1} window that is useful for comparing to extragalactic CGM measurements (see §3.3.2 for an explanation of this choice of velocity windows). The low-velocity ($|v| < 150$ km/s) C IV column densities and difference measurements for each star-quasar sightline pair are listed in Table 3.1. Low-velocity C IV column densities for stellar sightlines have a range of $\log N_{\rm CIV,star} = [13.12, 14.41]$ and the log of the median column density is 14.11; quasar sightlines have a range of $\log N_{\rm CIV,quasar} = [13.47, 14.40]$ and the log of the median column density is 14.16. The column density difference measurements for sightline pairs have a range of $\Delta\log N_{\rm LVCGM} = [11.41, 14.11]$ for pairs with excess quasar absorption and $\Delta\log N_{\rm LVCGM} = -[12.03, 13.88]$ for pairs with excess stellar absorption. Over all $\Delta\log N_{\rm LVCGM}$ measurements, the log of the median column density difference is -11.60 and the median sensitivity limit is $logN_{det} = 13.39$. The distribution of these values is shown by the violin plot at the center of the bottom panel of Figure 3.4.1. Within the low-velocity window we detect excess stellar absorption above the sensitivity limit for 3 sightline pairs (IDs 14, 19, & 20) and excess quasar absorption for 6 sightline pairs (IDs 5, 6, 11, 16, 17, & 30). We find a total low-velocity C IV covering fraction of $f_{\rm CIV,}{}_{star}$(log N>13.65)=97% [29/30] and $f_{\rm CIV,}{}_{quasar}$(log N>13.65) = 100% [30/30]; after subtracting fore-

ground gas absorption with the spectral differencing technique, the C IV covering fraction of the isolated CGM component is $f_{\rm CIV,LVCGM}$(log N>13.65)=20% [6/30]. If we assume that three of these sightlines are false positives caused by clumpy foreground gas (as discussed in §3.3.3), then the corrected covering fraction is $f^{*}_{\rm CIV,LVCGM}$(log N>13.65)=10% [3/30]. To test our assumption that there is negligible variation of C IV column density on scales of <2°, we confirmed that $|\Delta{\rm logN_{LVCGM}}|$ is not correlated with sightline separation of the star-quasar pair (p=0.67). We also confirmed that $\Delta{\rm logN_{LVCGM}}$ is not correlated with Galactic latitude (p=0.58), Galactic longitude (p=0.37), or distance to the foreground star (p=0.71).

We repeat these measurements within the wider $|v| < 300$ km/s velocity window, and obtain difference measurements with a range of $\Delta{\rm logN_{LVCGM}} = [12.04, 14.28]$ for pairs with excess quasar absorption and $\Delta{\rm logN_{LVCGM}} = -[12.42.13.92]$ for pairs with excess stellar absorption, with a log of the overall median column density difference of 12.65 and an overall median sensitivity limit of $logN_{det} = 13.56$. Within this wider velocity window we detect excess stellar absorption above the sensitivity limit for 2 sightline pairs (IDs 14 & 19), and excess quasar absorption for 10 sightline pairs (IDs 5, 6, 11, 16, 17, 21, 26, 27, 29, & 30). The covering fraction of CGM gas within the wider velocity window is $f_{\rm CIV,CGM}$(log N>13.65)=38% [9/24], and the corrected covering fraction is $f_{\rm CIV,CGM}$(log N>13.65)=25% [6/24]. Note that this covering fraction excludes any sightline pairs with a sensitivity limit greater than the given limiting column density. The absorption features we detect at $150 < |v| < 300$ km/s are typically distinct from any excess absorption at $|v| < 150$ km/s and do not suffer from blending. We identify the Magellanic System as the absorber in most of these sightlines and discuss possible origins of other excess absorption in §3.5.1.

The upper panel of Figure 3.4.1 shows the $\Delta{\rm logN_{LVCGM}}$ difference measurements within a $|v| < 150$ km/s velocity window, overlaid on a map of Galactic HVCs ($|v| > 70$ km s^{-1}) from the HI4PI survey in grey (HI4PI Collaboration et al., 2016; Westmeier, 2018). Each marker represents one star-quasar sightline pair and is labeled with an ID that can be referenced in Table 3.1 and Figure 3.2.2. Markers are blue if there is more C IV absorption along the quasar sightline, and red if there is more along the stellar sightline. The bottom panel plots the

same difference measurements against Galactic latitude and longitude separately, with their distribution in the middle. Each marker again represents one sightline pair, but here the color of the markers corresponds to their Galactic coordinates. The median sensitivity limit for the sample is shaded grey for reference, but each sightline pair may have a sensitivity limit above or below this value.

The fraction of sightline pairs with significant excess stellar absorption (3/30) is consistent with our expectation that 10% of sightline pairs will have stellar excess due to clumpiness in foreground gas (see §3.3.3). The quasar excess detection rate (6/30) suggests that the column density of extended Milky Way CGM gas is below our sensitivity limit of $\log N_{\mathrm{C\,IV}} < 13.39$ cm^{-2} across most of the sky. All but one of the significant detections are in the Northern Galactic hemisphere at latitudes $60° < b < 70°$. The two sightline pairs with the greatest excess quasar absorption (IDs 6 & 11) are close together at Galactic longitudes $270° < \ell < 300°$.

3.5 Discussion

In this section we comment on the significance of specific difference measurement detections and identify the Magellanic System, a low-velocity cloud, and HI Complex A as possible origins of the detected absorption. We then compare our observations of the Milky Way's CGM to similar measurements of external galaxies in order to place our results in larger context. Finally, we discuss apparent inconsistencies between the Milky Way and other galaxies, and explore some explanations which might reconcile them.

3.5.1 The Magellanic System and LVHCs

One of the most prominent features visible in the difference spectra is the excess quasar sightline absorption at $v \sim -250$ km/s for pair IDs 26, 27, and 29 (see Figure 3.2.2). The velocities and Galactic coordinates of these features are consistent with absorption from the Magellanic Stream (Nidever et al., 2008; Fox et al., 2014) and they have C IV column

densities $\log N_{CIV} = 13.81$, 13.78, and 14.16, respectively. Those three prominent absorbers account for 96% of the excess absorption added by the wider velocity window (that is, at $150 < |v| < 300$ km/s), which increases the median difference measurement of the overall sample by $\Delta\log N = 12.46$ from the narrower low-velocity window. Two other sightlines also have absorption identified as MS because they are in the direction of MS-associated HI gas: sightline 30 intersects a section of the Magellanic Stream with low radial velocities and shows some detectable absorption within the low-velocity window, while sightline 20 lies in the direction of the Magellanic Clouds and has a stellar excess within the low-velocity window.

The considerable contribution of high-velocity gas to the total column density detected in the Milky Way's CGM is an apparent contradiction to extragalactic CGM studies that detect $> 90\%$ of both low- and high-ionization CGM gas at velocities within 200 km/s of the galaxy systemic velocity (e.g., Tumlinson et al., 2013; Werk et al., 2016). But the Magellanic system is a dominant feature peculiar to the Milky Way, and therefore presents a complication when interpreting our results in the context of other Milky Way-like galaxies.

Our primary analysis of low-velocity gas, however, focuses on a $|v| < 150$ km/s window that excludes most MS absorption. Within that narrower window we detect low-velocity CGM gas for six sightline pairs. Three of these detections are likely due to expected fluctuations of foreground gas density (see §3.3). Furthermore, the quasar excess for pair #16 may be capturing the ionized edge of Complex A, which has a distance of 8 kpc $\lesssim d \lesssim$ 10 kpc (Wakker & van Woerden, 1997; Wakker, 2001; Sembach et al., 2003). The two remaining detections have a clear correlation with known structures. Sightline pairs 6 & 11 have the largest $\Delta\log N_{LVCGM}$ measurements, and both lie in the Northern Galactic hemisphere in the direction of a HI low-velocity halo cloud (LVHC) previously identified by Peek et al. (2009).

Low-velocity clouds represent a distinct population that has not been well-studied, but are associated with detections of both HI and metals that trace cooler gas, typically in the lower halo or the Milky Way disk (Ben Bekhti et al., 2009). The low-velocity cloud that corresponds to our detections is a continuation of a large HVC complex in the region (Peek

et al., 2009; Saul et al., 2012); aside from the MS, all known HVC complexes have distances that place them in the inner halo ($d \lesssim 15$ kpc). It is therefore unlikely that the low-velocity gas we detect in sightline pairs 6 & 11 originates in the extended CGM.

Finally, we note that five of the six quasar excess detections are found in the northern Galactic hemisphere. Although we do not know the distance to any of these absorbers with certainty, their distribution suggests that low-velocity CGM gas in the Milky Way is not spatially homogeneous.

3.5.2 Comparison with Low-Redshift CGM Surveys

In §3.4 we reported excess quasar absorption in 6/30 sightline pairs, and we expect that 3 ± 1 of those detections are due to fluctuations of foreground gas (see §3.3.3). Two of the remaining three detections originate in a low-velocity HI halo cloud that is likely to be located in the inner Galactic halo. Within a wider velocity window, almost all detected absorption originates from the Magellanic System. In sum, we detect very little low-velocity gas in the Milky Way's extended CGM. Are these results expected based on what we know about low-velocity halo gas in external Milky Way-like galaxies? In order to understand our findings, we must examine them in the context of existing extragalactic observations.

In this section we compare QuaStar column density measurements and covering fractions of C IV with similar measurements in external low-redshift galaxies. In addition to the low-velocity ($|v| < 150$ km/s) window used throughout our main analysis and discussion of this work (Figure 3.4.1 and Table 3.1), we use a wider velocity window ($|v| < 300$ km/s) to measure column density difference. This expanded velocity window is useful for comparison with external galaxies, which often include a velocity search window of ± 300 km s^{-1} from the galaxy redshift. However, complication arises with comparisons using the expanded velocity window because it includes Magellanic System absorption in the Milky Way, whereas there is scant evidence for LMC-like companions in other galaxies (Tollerud et al., 2011; Liu et al., 2011; James & Ivory, 2011). For that reason we consider measurements within the wider

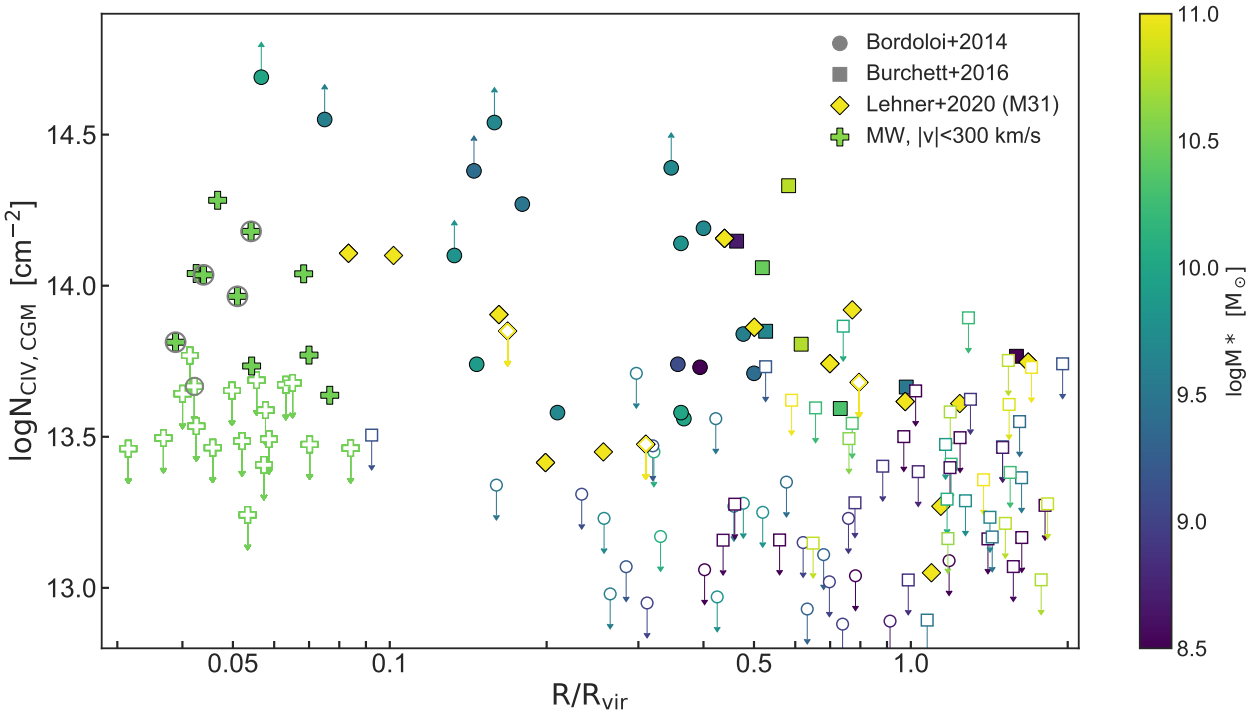

Figure 3.5.1: CGM column density in Milky Way vs. other galaxies. Column densities of C IV in the CGM of the Milky Way and other low-redshift galaxies (Bordoloi et al., 2014b; Burchett et al., 2016; Lehner et al., 2020) as a function of distance from the center of the host galaxy normalized by virial radius. In the case of external galaxies, R/R_{vir} is the impact parameter ρ of the sightline normalized by the galaxy's virial radius. For QuaStar sightlines, which have a different viewing geometry than extragalactic sightlines, R/R_{vir} is the paired star's Galactocentric distance normalized by the Milky Way's virial radius. The markers are filled if the measurement is a detection, otherwise the upper limit is shown with an open marker. Marker colors represent the stellar mass of the galaxy being probed by the sightline. The Milky Way column density difference measurements in QuaStar, represented by '+' symbols, are measured within a $|v| < 300$ km/s window, which includes the Magellanic System. QuaStar sightlines in the direction of the MS are circled.

velocity window to be more conservative in the context of investigating whether the Milky Way has anomalously sparse low-velocity CGM compared to other galaxies.

In Figure 3.5.1, we plot column densities of C IV as a function of R/R_{vir}, the distance from the center of the host galaxy normalized by its virial radius. In the case of external galaxies, R/R_{vir} is the impact parameter ρ of the sightline normalized by the galaxy's virial radius. For QuaStar sightlines, which have a different viewing geometry than extragalactic sightlines, R/R_{vir} is the paired star's Galactocentric distance normalized by the Milky Way's virial radius. Column densities are represented by markers colored according to the stellar mass of the host galaxy; the markers are filled if the measurement is a detection, otherwise the upper limit is shown with an open marker. The Milky Way column density difference measurements in QuaStar, represented by '+' symbols, are measured within a $|v| < 300$ km/s window that includes the MS. QuaStar sightlines in the direction of the MS are circled. We assume a virial radius of 230 kpc for the Milky Way, determined by adopting a mass of $M_{vir} = 1.3 \times 10^{12}$ (Posti & Helmi, 2019), $\rho_{crit} = 2.78 \times 10^{11} h^2 M_\odot$ Mpc^{-3} (Planck Collaboration et al., 2014), and the $R_{200} - M_{halo}$ relation, $R_{200}^3 = 3M_{halo}/4\pi\Delta_{vir}\rho_{matter}$.

We compare our results with C IV column densities of low-velocity gas in the halos of M31 (Lehner et al., 2020), a sample of nearby galaxies ($z < 0.015$; Burchett et al., 2016), and the COS-Dwarfs survey ($z < 0.1$; Bordoloi et al., 2014b) in Figure 3.5.1. It should be noted that many of these galaxies have stellar masses significantly lower than the Milky Way, and do not necessarily reflect the distribution of nearby galaxies. The CGM of dwarf galaxies may have a different density profile than L^* galaxies, and they are thought to experience halo-scale flows tied to star-formation activity which may drive gas loss (Oppenheimer et al., 2018a; Johnson et al., 2017; Li et al., 2021). Ideally we would only compare our results to measurements of galaxies with masses and star-formation rates similar to the Milky Way, but the data for C IV in galaxy halos are sparse. At this time, the column densities we show in Figure 3.5.1 represent the only substantial datasets available with C IV column densities around low-redshift galaxies.

The available measurements of C IV around external galaxies exhibit a trend of increasing column density at smaller impact parameters, and at $R/R_{vir} < 0.2$ most $\log N_{CIV}$ measurements fall well above the sensitivity limit of QuaStar (the majority are lower limits as a result of saturation). The few Milky Way CGM detections are slightly lower than expected based on this trend, although they appear roughly consistent with the C IV in M31 as measured by the AMIGA survey (Lehner et al., 2020). However, most QuaStar sightlines do not show detectable C IV in the Milky Way's CGM; this is inconsistent with the external sightline measurements, particularly at low impact parameters.

The striking discrepancy between the Milky Way and other low-redshift galaxies is illustrated most clearly in Figure 3.5.2. The black line represents the empirical cumulative covering fraction for all sightlines within some radial distance of a galaxy, calculated for the three data sets in Figure 3.5.1 combined (Bordoloi et al., 2014b; Burchett et al., 2016; Lehner et al., 2020). The 1-σ and 2-σ Wilson binomial confidence intervals are shaded light and dark grey, respectively. The symbols with error bars represent the covering fraction and 1-σ confidence interval for Milky Way CGM detections in QuaStar within the low-velocity window ('LV MW', $|v| < 150$ km/s) and broader window that includes Magellanic System absorption ('MW', $|v| < 300$ km/s). For external galaxies, the cumulative covering fraction trends upward at smaller impact parameters, approaching unity at $R/R_{vir} < 0.1$.

The CGM covering fraction in the Milky Way (as observed from within the Galaxy at $R \sim 0.03 R_{vir}$) is not consistent with the trend in detection rate for external galaxies. This is especially evident in the low-velocity window, which has a covering fraction of $f_{C,LV\,MW} = 20\%$, well below the cumulative covering fraction of $f_{C,lit}(R < 0.2R_{vir}) = 79\%$ for external galaxy sightlines. For the $|v| < 300$ km/s window, the Milky Way covering fraction is higher at $f_C, MW = 38\%$ but still significantly lower than the trend for external galaxies.

It is particularly unexpected that the window that includes Magellanic System absorption has a lower covering fraction than external galaxies. Satellite galaxies the size of the Magellanic Clouds are uncommon in the halos of L* galaxies (Tollerud et al., 2011; Liu et al., 2011; James & Ivory, 2011), so one might naively expect a galaxy like the Milky Way to have

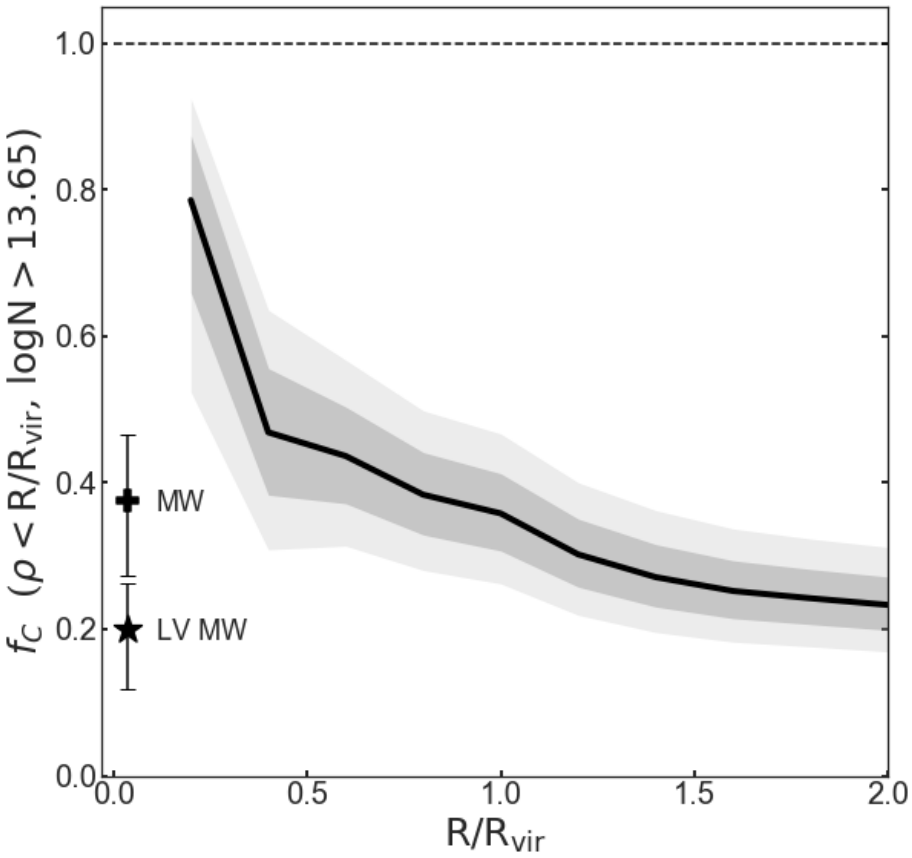

Figure 3.5.2: CGM covering fraction in Milky Way vs. other galaxies. Cumulative covering fraction f_C of low-velocity C IV CGM gas for impact parameters within R/R_{vir} of the host galaxy and a limiting column density of 13.65. The black line represents the covering fraction of low-velocity CGM gas for the combined samples of external galaxies presented in Figure 3.5.1 (Burchett et al., 2016; Bordoloi et al., 2014b; Lehner et al., 2020). The 1-σ and 2-σ Wilson binomial confidence intervals are shaded light and dark grey, respectively. The star symbol represents the covering fraction and 1-σ confidence interval for low-velocity CGM detections in QuaStar ('LV MW', $|v| < 150$ km/s), and the plus symbol represents the same measurement within a wider velocity window that includes the Magellanic System ('MW', $|v| < 300$ km/s). The cumulative covering fraction for external galaxies grows larger at smaller impact parameters, approaching unity at $R/R_{vir} < 0.1$. The CGM covering fraction in the Milky Way, as observed from within the Galaxy at $R \sim 0.03\ R_{vir}$, is inconsistent with the trend for the CGM covering fractions in external galaxies.

a covering fraction that is higher than other galaxies. The discrepancy between the Milky Way and its low-redshift neighbors only widens when we consider that three of the sightlines showing excess quasar absorption may be the result of foreground clumpiness. Furthermore, the inconsistency persists even when we account for the shorter distance probed by the Milky Way's inside-out sightline geometry.

It is important to recognize how different observing geometries constrain CGM measurements in the Milky Way versus those made in external galaxies, and consequently how those geometries affect observed column densities. Measurements of the Milky Way's CGM are affected by an "inside-out" geometric observing bias that differs from the "outside-in" geometric bias for external galaxies. Any sightline that probes the Milky Way's extended CGM must also pass through the denser and more clumpy gas in the inner halo. Although the QuaStar survey is designed to circumvent this issue, subtracting absorption from foreground gas introduces some uncertainty that does not affect external galaxy measurements. Furthermore, all QuaStar sightlines are at high Galactic latitude ($|b|$ >30°) and originate from the same point within the Galaxy, while extragalactic sightlines pierce galaxy halos at a range of orientations and distances from the host galaxy.

The different observing geometries also mean that in the Milky Way, gas velocities are measured along sightlines pointing radially outward from the disk, while velocities within extragalactic systems are measured along sightlines in a direction tangential to the galaxy. In both cases, measured velocities are only a projection of the true gas velocity onto the line of sight. Therefore, even if the CGM of the Milky Way and other L* galaxies were identical, a velocity structure that changes along the radial direction would result in different observed velocities and increase the scatter of inside-out measurements by a factor of ~ 2 (Zheng et al., 2020). Such asymmetries in the kinematics of CGM gas are indeed seen in idealized simulations (Lochhaas et al., 2020). If this is correct, the gas that is detected at low velocities in external galaxies might be detected at > 150 km/s if the same gas was observed from within the galaxy (Zheng et al., 2015).

To check that our results are not being driven by an observing geometry bias, we repeated the comparison to external galaxies using a 'chord length' parameter. The chord length of each sightline is defined as the full distance the sightline traverses within the virial radius of the host galaxy, and is equal to $2\sqrt{R_{\rm vir}^2 - \rho^2}$. For external galaxy sightlines, ρ is the impact parameter; for QuaStar sightlines, it is the foreground star's Galactocentric distance. Chord length therefore scales inversely with impact parameter for external galaxies. For example, in a galaxy with a virial radius of $R_{vir} = 200$ kpc, impact parameters of 50 kpc and 150 kpc correspond to chord lengths of 387 kpc and 265 kpc, respectively. For Milky Way sightlines with $\rho = 8$ kpc, the chord length is approximately 230 kpc. If we observed the Milky Way from the outside in like an external galaxy, the same chord length would correspond to a much larger impact parameter. Even so, when we compare the Milky Way to external galaxies using chord length, we still find a significantly lower covering fraction of low-velocity C IV in the Milky Way. The chord length thus provides an additional, conservative metric for comparing the disparate Milky Way and extragalactic datasets. However, without deprojected velocities and actual distance information for the absorbers along their sightlines, it is not possible to fully account for all biases arising from observing geometry. We emphasize that these biases may affect measured column densities in both the Milky Way and external galaxies.

3.5.3 Understanding the CIV Content of the Extended CGM: Is the Milky Way an Anomaly?

To interpret our results, we must consider the physical properties of C IV-bearing gas within the broader context of a complex, multiphase CGM (Tumlinson et al., 2017). Generally, C IV has two possible phases: (1) along with common metal ions such as Si IV, N V, and O VI, it may trace warm, collisionally-ionized "transition temperature" or "intermediate-ionization-state" gas at $T \sim 10^{5.5}$ K (e.g. Werk et al., 2016); (2) C IV (and other intermediate ions present in the CGM) could also trace low-density, cool T$\approx 10^{4.5}$ K photoionized material, generally envisioned as clouds in the CGM (e.g. Stern et al., 2016). In a simulated experiment

similar to QuaStar, Zheng et al. (2020) used mock observations of 5,000 quasar-star pairs through the halo of a high-redshift Milky Way analog in the FOGGIE simulation (Peeples et al., 2019) and found that C IV may be a less sensitive tracer of the outer CGM than O VI and N V. In the FOGGIE simulations of high-redshift Milky Way analogs, therefore, C IV appears to predominantly trace cooler material typically detected as low ionization state metal species. In contrast, the cosmological hydrodynamical simulation EAGLE, with its AGN feedback model, predicts that C IV manifests as both warm and cool material, making it an ideal tracer of the total baryonic content of the CGM (Oppenheimer et al., 2020). Thus, the near-absence of C IV in the QuaStar observations could mean either a lower quantity of low-density photoionized, cool clouds relative to other nearby star-forming galaxies, or, alternatively, an atmosphere depleted of transitional temperature gas, which is primarily exhibited by non-star-forming galaxies (Tumlinson et al., 2011).

With this in mind, we can speculate about what might cause the surprisingly low covering fraction we find for low-velocity gas in the Milky Way's CGM. QuaStar observations hint at a C IV distribution that deviates notably from the norm; we find that the bulk of the column density detected in the halo beyond $d \sim 14$ kpc is associated with the MS at velocities greater than 150 km/s (see §3.5.1). This is kinematically very different from sightlines through external galaxy halos, in which the bulk of the CGM gas column density tends to sit at $v < 150$ km s^{-1} relative to galaxy systemic velocities (e.g., Tumlinson et al., 2013; Werk et al., 2014; Zheng et al., 2019). These contrasting measurements do not necessarily mean the Milky Way is missing C IV at low velocities, however. For example, if halo gas predominantly flows in a radial direction, differing observing geometries in the Milky Way versus external galaxies (discussed in §3.5.2) could cause halo gas velocities projected along the line of sight to be lower for external galaxies, producing a similar effect.

Moreover, because QuaStar focuses on high-latitude ($|b| > 30°$) sightlines, we cannot rule out the intriguing possibility that the C IV-traced CGM lies predominantly at lower Galactic latitudes. A toroidal or flared-disk morphology would not be probed by the QuaStar survey's inside-out high-latitude sightlines, but could be detected by outside-in sightlines through

external galaxy halos with almost any orientation. Such an extended disk model is supported at least indirectly by observational and theoretical work that find evidence for a large-scale rotational signal in the CGM (Hodges-Kluck et al., 2016; Oppenheimer, 2018; Martin et al., 2019; Ho et al., 2017; Zabl et al., 2019). Other work has suggested that a co-rotating warm gas disk in the Milky Way may be more extended in the direction perpendicular to the disk rather than the radial direction (e.g., Qu & Bregman, 2019; Qu et al., 2020), so future observations using low-latitude sightlines will be important for constraining this picture of the CGM.

We also consider the possibility that the Milky Way truly is different from most nearby star-forming galaxies. Evidence suggests that the Milky Way is a green valley galaxy, falling between the red sequence of quenched galaxies and the blue cloud of galaxies with active star formation on the color-magnitude diagram (Mutch et al., 2011; Licquia et al., 2015; Licquia, 2016; Bland-Hawthorn & Gerhard, 2016). Star formation in Milky Way-mass galaxies declines over several Gyr on average, more slowly than lower-mass galaxies (Pacifici et al., 2016). Although a global star-formation history for the Milky Way itself is difficult to determine, the Galaxy may currently be in such a period of decline (Snaith et al., 2014, 2015). In intermediate- and high-mass galaxies at low redshift, decreasing star formation is tied to mechanisms such as gas consumption and weak tidal interactions with small satellite galaxies, like the Magellanic Clouds (Bell et al., 2005).

The transformation galaxies experience as they begin to quench is not yet fully understood, but the CGM, which plays a key role in sustaining star formation by serving as a reservoir of gas, is almost certainly impacted by the process. Indeed, the presence of O VI in galaxy halos is confirmed to correlate with global star formation, while it is relatively absent from the halos of non-star-forming galaxies (Tumlinson et al., 2011). The physical explanation for this observed dichotomy in O VI is widely debated (e.g. Oppenheimer et al., 2016; McQuinn & Werk, 2018), but if O VI and C IV both trace T $\approx 10^{5-6}$ K transitional-temperature gas, then the near absence of C IV in the Milky Way's halo may be a similar reflection of its declining star-formation rate. Unfortunately, this is difficult to test directly

because there are few measurements of C IV in the CGM of quiescent galaxies available for such a comparison. Simultaneous measurements of both O VI and C IV are exceedingly rare given available UV detector characteristics and the two doublets' > 500 Å separation in wavelength, though some such measurements have been made for a few systems (e.g., Werk et al., 2016; Johnson et al., 2017).

Finally, the Local Group environment, which contains both M31 and the Milky Way, may not be representative of the typical environment of L* galaxies. Galaxy environment has been tied to the CGM properties of galaxies and may exert a divergent influence on otherwise similar galaxies (e.g. Yoon & Putman, 2013; Stocke et al., 2014; Burchett et al., 2018). The SAGA survey reports that 86% (109/127) of its MW analog satellites are star-forming, in contrast to only 29% (4/14) of Local Group satellites of both M31 and the Milky Way in the same mass range (Geha et al., 2017; Mao et al., 2021). The low star formation rates of the Local Group satellites compared to other L* satellite populations may indicate different local environmental conditions shaping the Milky Way that ultimately manifest as different CGM properties. What's more, satellites as massive as the Milky Way's SMC/LMC are not typically found around low-redshift galaxies (Tollerud et al., 2011; Liu et al., 2011; James & Ivory, 2011). The Milky Way is expected to merge with the LMC in $\sim$2.4 Gyr (Cautun et al., 2019), an event which will undoubtedly disrupt circumgalactic gas. After this significant interaction, the global properties of the Milky Way's CGM may better match those of nearby star-forming galaxies.

Generally, CGM covering fractions of a range of ionized and neutral gas tracers are lower in cluster environments compared to isolated galaxies (Yoon & Putman, 2013; Pointon et al., 2017; Zhang et al., 2019), but assessing the nature and impact of small group environments is more difficult. In particular, data cannot yet distinguish between gas associated with an intragroup medium and the CGM of a massive halo (Stocke et al., 2017, 2019). It is therefore possible that our anomalously low C IV covering fractions and median column densities are simply indicative of a hotter intragroup medium relatively devoid of C IV compared to other more "typical" L* environments. The somewhat low C IV column densities measured within

0.5 $R/R_{\rm vir}$ of M31 relative to the CGM of other nearby galaxies, evident in Figure 3.5.1 (yellow diamonds), may lend support to the idea that both the Milky Way and M31 reside in an environment with a depleted C IV-traced gaseous reservoir. However, the AMIGA survey reports a C IV covering fraction of approximately 50% (with a threshold column density of log $N_{CIV} = 13.8$) within 150 kpc of M31 (Lehner et al., 2020), significantly higher than what we find around the Milky Way and roughly consistent with results for other nearby L* galaxies.

To make progress in our understanding, more observations of the low-velocity CGM will be needed. Sightlines at low Galactic latitudes in particular are important for constraining the morphology of the low-velocity CGM and testing the idea that warm gas is hidden in an extended, flared disk. HST/COS is the best available instrument for observing UV absorption lines of warm gas, and allows us to map ions like C IV and Si IV. Additional measurements of these ions in the CGM of low-redshift, Milky Way-like galaxies will be key for making robust comparisons with the Milky Way. Although there are no concrete plans to bring new, highly-sensitive, high-resolution spectrographs online with wavelength coverage in the far UV, it will be necessary to measure ions that trace other gas phases to bring a complete picture of the low-velocity CGM into focus.

3.6 Conclusions

The QuaStar survey has enabled the first measurements of the Milky Way's low-velocity CGM ($|v| < 150$ km/s) that are unobscured by foreground gas in the disk. We measured C IV column densities along sightlines to 30 halo stars (d $\sim$ 8 kpc) paired with quasars at small angular separations ($< 2.8°$), evenly sampling the sky at Galactic latitudes $|b| > 30°$ (§3.2; Figure 3.2.1). Applying a spectral differencing technique, we isolated Milky Way CGM absorption in each quasar spectrum by subtracting the foreground gas absorption measured in its paired stellar spectrum to obtain a "difference measurement" $\Delta\log N_{\rm LVCGM}$ (§3.3; Figure 3.2.2). Our main results are as follows:

1. We detect low-velocity ($|v| < 150$ km/s) C IV in the Milky Way's CGM for 6/30 sightline pairs, place an upper limit of $\Delta\log N_{\rm LVCGM} < 13.39$ cm^{-2} on the median column density,

and report a covering fraction of $f_{\rm CIV,LVCGM}$(logN>13.65) = 20% [6/30]. Within a wider velocity range that includes the Magellanic System ($|v|$ < 300 km/s), we detect C IV for 10/30 sightline pairs, place an upper limit of logN< 13.56 cm^{-2} on the median column density and report a covering fraction of $f_{\rm CIV,CGM}$(logN>13.65) = 38% [9/24]. 96% of the additional absorption detected in this wider velocity window likely originates in the Magellanic System. Accounting for the existence of foreground substructure with angular scales below our sightline separations further reduces these two covering fractions to 10% and 25%, respectively. (§3.3, §3.4, and §3.5.1; Figures 3.2.2 and 3.4.1)

2. The covering fraction of low-velocity C IV in the Milky Way's CGM is markedly lower than observations of other L* galaxies. Although it is possible the Milky Way represents an anomaly, the differing geometric viewing effects of the Milky Way and external galaxies allow for the possibility that the warm, low-velocity CGM of L* galaxies exhibits a flared-disk morphology. QuaStar's 'inside-out' observations of the Milky Way at high latitudes would not probe such a structure, while 'outside-in' sightlines with various orientations would be more likely to detect it in external galaxies. Alternatively, it is possible that the Milky Way's CGM is uniquely affected by environment, or has begun the process of quenching and thus appears different than typical star-forming galaxies. (§3.5; Figures 3.5.1 and 3.5.2)

Table 3.1: PROPERTIES OF STAR-QUASAR SIGHTLINE PAIRS: (1) Sightline pair ID used in this work, followed by 'S' for star and 'Q' for quasar. (2) Catalog name of the star or quasar. (3 - 6) Right ascension/declination and Galactic longitude/latitude of the source. (7) Angular separation on the sky between the star and quasar sightlines. (8) Distance to the star. No distance is reported for quasars. (9) Column densities for the C IV ($\lambda\lambda$ 1548, 1550 Å) doublet within $\pm$150 km s^{-1} of the Local Standard of Rest (LSR). (10) The difference in the measured C IV column densities for each close sightline pair. (11) Symbols: $\varnothing$ non-detection, $\bullet$ excess QSO absorption, or $\circ$ excess stellar absorption. Sightlines in the direction of the Magellanic Stream are labeled 'MS'.

ID	Name	RA	Dec	l	b	$\Delta\theta$	d_{star}	logN$_{\rm CIV}$	logN$_{\rm LVCGM}$	
		[h:m:s]	[d:m:s]	[°]	[°]	[°]	[kpc]	[cm^{-2}]	[cm^{-2}]	
(1)	(2)	(3)	(4)	(5)	(6)	(7)	(8)	(9)	(10)	(11)
1S	J1339+3136	13:39:05.82	+31:36:30.70	59.12	78.70	1.77	9.6	$14.19^{+0.05}_{-0.06}$	<13.34	$\varnothing$
1Q	SDSSJ133053.27+311930.5	13:30:53.28	+31:19:30.72	61.28	80.43		-	$14.17^{+0.05}_{-0.06}$		
2S	J1344+1842	13:44:04.41	+18:42:59.03	0.89	75.26	0.31	10.4	$14.37^{+0.03}_{-0.03}$	<13.47	$\varnothing$
2Q	SDSSJ134246.89+184443.6	13:42:46.80	+18:44:43.80	0.24	75.53		-	$14.37^{+0.06}_{-0.07}$		
3S	J1406+2441	14:06:38.54	+24:41:41.89	28.96	72.93	1.86	9.0	$14.26^{+0.05}_{-0.05}$	<13.32	$\varnothing$
3Q	SDSS-J141038.39+230447.1	14:10:38.40	+23:04:47.18	24.57	71.64		-	$14.25^{+0.04}_{-0.04}$		
4S	J1131+3112	11:31:39.17	+31:12:47.98	194.96	72.14	0.11	8.2	$14.11^{+0.06}_{-0.07}$	<13.26	$\varnothing$
4Q	TON580	11:31:09.50	+31:14:05.00	194.94	72.03		-	$14.12^{+0.02}_{-0.03}$		
5S	J1113+2736	11:13:47.22	+27:36:48.51	205.99	68.35	1.39	11.4	$14.11^{+0.06}_{-0.07}$	$+13.73^{+0.23}_{-0.52}$	$\bullet$
5Q	SDSSJ111754.31+263416.6	11:17:54.24	+26:34:16.68	209.10	69.16		-	$14.26^{+0.07}_{-0.08}$		
6S	J1212+0621	12:12:21.95	+06:21:24.30	277.09	67.25	1.76	7.3	$13.96^{+0.06}_{-0.07}$	$+14.07^{+0.07}_{-0.08}$	$\bullet$
6Q	PG1216+069	12:19:20.93	+06:38:38.52	281.07	68.14		-	$14.32^{+0.03}_{-0.04}$		
7S	J1118+4029	11:18:21.44	+40:29:07.88	172.15	66.62	1.94	7.9	$14.10^{+0.07}_{-0.08}$	<13.34	$\varnothing$
7Q	PG1121+422	11:24:39.18	+42:01:45.02	167.26	66.86		-	$14.13^{+0.04}_{-0.05}$		
8S	J1339+0511	13:39:03.97	+05:11:57.35	332.40	65.31	0.77	8.2	$14.22^{+0.06}_{-0.07}$	<13.37	$\varnothing$
8Q	SDSSJ134206.56+050523.8	13:42:06.48	+05:05:24.00	333.89	64.87		-	$14.21^{+0.04}_{-0.04}$		
9S	J1449+3459	14:49:20.37	+34:59:40.18	57.61	63.67	1.00	7.1	$14.19^{+0.05}_{-0.06}$	<13.64	$\varnothing$
9Q	SDSSJ144511.28+342825.4	14:45:11.28	+34:28:25.45	56.74	64.59		-	$14.14^{+0.13}_{-0.19}$		
10S	J1400+0535	14:00:35.61	+05:35:17.21	343.40	62.89	1.27	7.7	$13.96^{+0.09}_{-0.11}$	<13.36	$\varnothing$

ID	Name	RA [h:m:s]	Dec [d:m:s]	l [°]	b [°]	$\Delta\theta$ [°]	d_{star} [kpc]	logN$_{\rm CIV}$ [cm^{-2}]	logN$_{\rm LVCGM}$ [cm^{-2}]	
10Q	SDSS-J135726.27+043541.4	13:57:26.27	+04:35:41.40	340.77	62.51		-	$13.99^{+0.07}_{-0.09}$		
11S	J1235-0108	12:35:00.48	-01:08:54.80	294.32	61.45	0.79	7.1	$14.09^{+0.06}_{-0.07}$	$+14.11^{+0.12}_{-0.17}$	●
11Q	SDSSJ123304.05-003134.1	12:33:04.05	-00:31:34.17	293.11	61.99		-	$14.40^{+0.06}_{-0.07}$		
12S	PG0955+291	09:58:15.14	+28:52:33.12	199.88	51.94	1.27	5.5	$14.17^{+0.02}_{-0.03}$	<13.09	∅
12Q	PG1001+291	10:04:02.59	+28:55:35.18	200.08	53.21		-	$14.13^{+0.03}_{-0.03}$		
13S	J1057-0108	10:57:52.64	-01:08:54.95	254.32	50.68	1.53	9.1	< 13.28	<13.41	∅
13Q	PG1049-005	10:51:51.44	-00:51:17.73	252.28	49.88		-	$13.47^{+0.22}_{-0.45}$		
14S	J1511+0452	15:11:38.17	+04:52:54.54	5.56	49.89	1.84	10.8	$14.41^{+0.05}_{-0.05}$	$-13.88^{+0.24}_{-0.15}$	○
14Q	MRK1392	15:05:56.55	+03:42:26.21	2.75	50.26		-	$14.26^{+0.02}_{-0.03}$		
15S	J1019-0051	10:19:35.54	+00:51:12.57	244.15	44.01	2.49	7.5	$13.88^{+0.10}_{-0.13}$	<13.56	∅
15Q	SDSSJ102218.99+013218.8	10:22:18.99	+01:32:18.82	242.16	46.07		-	$13.90^{+0.15}_{-0.23}$		
16S	J0841+4529	08:41:21.54	+45:29:12.42	174.86	37.81	2.74	10.4	$13.85^{+0.10}_{-0.13}$	$+13.93^{+0.09}_{-0.12}$	●
16Q	Q0850+440	08:53:34.24	+43:49:02.28	177.08	39.94		-	$14.20^{+0.02}_{-0.02}$		
17S	J0841+2340	08:41:40.74	+23:40:03.36	201.51	34.07	1.92	8.5	$13.61^{+0.18}_{-0.33}$	$+13.94^{+0.15}_{-0.22}$	●
17Q	PG0832+251	08:35:35.80	+24:59:41.00	199.49	33.15		-	$14.11^{+0.09}_{-0.11}$		
18S	J0456-2447	04:56:15.22	-24:47:36.77	225.26	-35.48	2.81	13.5	$13.79^{+0.12}_{-0.17}$	<13.31	∅
18Q	QSOJ0456-2159	04:56:08.93	-21:59:09.30	221.98	-34.65		-	$13.84^{+0.07}_{-0.08}$		
19S	J2129-1112	21:29:17.55	-11:12:03.19	41.30	-40.05	1.08	11.1	$14.37^{+0.05}_{-0.05}$	$-13.76^{+0.27}_{-0.16}$	○
19Q	PHL1598	21:31:35.20	-12:07:04.50	40.54	-40.96		-	$14.24^{+0.02}_{-0.02}$		
20S	J0158-7527	01:58:15.71	-75:27:25.37	297.45	-40.95	0.91	8.8	$14.20^{+0.06}_{-0.07}$	$-13.70^{+0.80}_{-0.26}$	MS ○
20Q	HB89-0202-765	02:02:13.70	-76:20:03.10	297.55	-40.05		-	$14.03^{+0.12}_{-0.16}$		
21S	J0420-5233	04:20:08.33	-52:33:47.75	261.11	-43.93	2.56	8.5	$14.31^{+0.05}_{-0.05}$	<13.43	∅
21Q	HE0435-5304	04:36:50.80	-52:58:49.00	261.02	-41.37		-	$14.29^{+0.05}_{-0.06}$		
22S	J2326-7108	23:26:01.06	-71:08:39.21	312.41	-44.38	0.78	10.6	$14.22^{+0.05}_{-0.06}$	<13.37	∅
22Q	RXS-J23218-7026	23:21:51.10	-70:26:44.00	313.29	-44.84		-	$14.24^{+0.03}_{-0.03}$		
23S	J2156-4403	21:56:38.48	-44:03:02.93	355.37	-51.21	0.37	8.5	$14.21^{+0.06}_{-0.06}$	<13.32	∅

ID	Name	RA [h:m:s]	Dec [d:m:s]	l [°]	b [°]	$\Delta\theta$ [°]	d_{star} [kpc]	logN$_{\rm CIV}$ [cm^{-2}]	logN$_{\rm LVCGM}$ [cm^{-2}]	
23Q	RXJ2154.1-4414	21:54:51.06	-44:14:06.00	355.18	-50.86		-	$14.18^{+0.03}_{-0.03}$		
24S	J0228-0132	02:28:23.16	-01:32:41.41	169.27	-55.44	1.88	8.2	$14.18^{+0.06}_{-0.07}$	<13.50	∅
24Q	GALEX-J022614.4+001530	02:26:14.46	+00:15:30.01	166.57	-54.38		-	$14.10^{+0.08}_{-0.10}$		
25S	J0243-0636	02:43:43.26	-06:36:59.69	180.49	-56.37	1.39	8.8	$14.00^{+0.09}_{-0.12}$	<13.56	∅
25Q	SDSSJ024250.85-075914.2	02:42:50.87	-07:59:14.28	182.15	-57.42		-	$14.00^{+0.11}_{-0.16}$		
26S	J2345-0157	23:45:29.55	-01:57:28.50	88.03	-60.28	0.97	8.5	$14.04^{+0.07}_{-0.08}$	<13.55	MS ∅
26Q	SDSSJ234500.43-005936.0	23:45:00.43	-00:59:36.06	88.79	-59.39		-	$14.07^{+0.11}_{-0.16}$		
27S	J2255-1727	22:55:27.05	-17:27:10.53	46.73	-61.56	0.35	7.1	$14.19^{+0.06}_{-0.07}$	<13.43	MS ∅
27Q	MR2251-178	22:54:05.88	-17:34:55.30	46.20	-61.33		-	$14.19^{+0.02}_{-0.02}$		
28S	J0235-1757	02:35:31.78	-17:57:34.98	197.48	-64.34	1.49	10.9	$14.08^{+0.08}_{-0.09}$	<13.33	∅
28Q	HE0238-1904	02:40:32.50	-18:51:51.00	200.48	-63.63		-	$14.00^{+0.03}_{-0.03}$		
29S	J0004-0845	00:04:41.65	-08:45:06.77	89.73	-68.56	2.50	9.4	$13.97^{+0.06}_{-0.08}$	<13.46	MS ∅
29Q	NEWQZ026	00:12:24.01	-10:22:26.40	92.32	-70.89		-	$13.93^{+0.13}_{-0.18}$		
30S	J0053-3606	00:53:39.63	-36:06:49.70	300.06	-81.00	1.00	6.5	$14.09^{+0.07}_{-0.08}$	$+13.98^{+0.10}_{-0.12}$	MS ●
30Q	HE0056-3622	00:58:37.39	-36:06:05.03	293.72	-80.90		-	$14.34^{+0.02}_{-0.02}$		

Chapter 4

DIFFERENTIAL ACCRETION OF NEUTRAL, WARM, AND WARM-HOT IONIZED GAS AT THE MILKY WAY'S DISK-HALO INTERFACE

The work in this chapter was produced in collaboration with Jessica K. Werk, Joshua E.G. Peek, Yong Zheng, and Mary Putman and will be submitted for publication in the Astrophysical Journal.

Chapter Summary

We measure line of sight velocities of absorption and emission lines along 147 QSO lines of sight in order to study gas accretion and outflow at the disk-halo interface. While previous studies have focused on high- and intermediate-velocity clouds and complexes, we examine predominantly low-velocity material relative to the Local Standard of Rest. We find that gas accretion velocities depend upon the ionization potential energy of the multiphase metal ions we include in our analysis. More highly ionized material traced by C IV, Si IV, and N V is moving toward the disk $10-15$ km s^{-1} faster than low ionization state material traced by S II, C II*, and Ni II. We interpret this dependence as evidence of warm accreting gas cooling as it reaches the disk-halo interface, causing a pileup of cool gas. We constrain accretion timescales and mass flow rates to be XX, [with accretion rates approximately ten times higher than outflow rates]. We find that kinematic modeling cannot rule out exponential density distributions or layers of gas which sandwich the Galactic disk. Our results paint a picture of a complex, dynamic disk-halo interface in which low-velocity material plays an equally important role in fueling the star formation in the Milky Way as the well-studied high- and intermediate-velocity clouds.

4.1 Introduction

The evolution and fate of galaxies is enmeshed with the gas flows that cycle through them. Without a long-term supply of infalling gas, most spiral galaxies would exhaust the available gas in the disk – and thus their fuel for star formation – within a few Gyr (Erb, 2008; Hopkins et al., 2008; Putman et al., 2009; Chomiuk & Povich, 2011; Leroy et al., 2013). The movement of gas through a galaxy is regulated by a chaotic dance of outflowing and inflowing material. In this Galactic fountain scenario, Galactic feedback driven by stellar winds, supernovae, and

active galactic nuclei (AGNs) ejects gas out of the disk, where it may be recycled through re-accretion or escape the galaxy entirely (Bordoloi et al., 2011, 2014c; Rubin et al., 2014; Heckman et al., 2017). At the same time the disk is fed by infalling gas, which may either originate externally from cosmic filaments in the intergalactic medium (Ribaudo et al., 2011; Kacprzak et al., 2012; Bouché et al., 2013), internally from clouds within the Galactic halo, or be stripped from orbiting satellites (). Combined, these mechanisms produce the extended halo of diffuse, multi-phase gas that makes up the circumgalactic medium (CGM) and serves as a reservoir of star-formation fuel.

Any gas flowing into the galaxy must pass through both the CGM and the disk-halo interface, a transitional boundary layer where halo gas is integrated into the disk (Norman & Ikeuchi, 1989; Ford et al., 2010; Putman et al., 2012). The disk-halo interface, also referred to as extraplanar gas, is rich in information about gas in the final stages of accretion as it fragments, mixes with the disk and interacts with outflowing material. Here, hot gas being forcefully ejected from the galaxy collides with gas cooling close to the disk (Joung & Mac Low, 2006; Hill et al., 2012; Putman et al., 2012; Creasey et al., 2013; Li et al., 2017).

The properties of gas at the disk-halo interface are complex and dynamic. Gas moving in and out of the disk experiences changes in density, ionization state, and velocity as it interacts with ambient material. In general the disk-halo interface exhibits decreasing rotational velocity as z-height increases, known as "lag," and shows a clear temperature gradient that changes from cool near the disk to hot in the lower halo (Putman et al., 2012). Gas observed close to the disk of the Milky Way sits mostly in a dense, cold layer of HI, ranging in thickness from < 100 pc near Galactic center, to $\sim$1 kpc near the Galactic warp, to > 6 kpc in the outermost reaches of the disk (Dickey & Lockman, 1990; Levine et al., 2006). At higher z-heights of $\sim$1-2 kpc, this cool ($T \lesssim 10^4$ K) layer gives way to a more diffuse, warm ($T \sim 10^4$ K) component of inhomogeneous ionized gas called the Reynolds Layer, or warm ionized medium (WIM), which has been observed in Hα and a number of other emission and absorption lines (Reynolds, 1993; Haffner et al., 2003; Gaensler et al., 2008; Savage & Wakker, 2009). Above the WIM, even more diffuse, higher temperature warm-hot ($T \sim 10^5$

K) and hot ($T \gtrsim 10^5$ K) gas has been detected in absorption extending into the Galactic halo out to ∼3-5 kpc (Savage & Wakker, 2009; Sembach & Savage, 1992; Shull & Slavin, 1994; Miller & Bregman, 2013; Miller & Bregman, 2015).

It is thought that the cooling of gas observed at the disk-halo interface may be an important mechanism for delivering star-formation fuel to galactic disks. Warm/hot gas is too diffuse to be incorporated directly into galaxy disks, but the satellites and HI clouds found in the Milky Way's halo do not contain enough cold gas to sustain star formation in the Milky Way through direct accretion alone (Putman et al., 2012). This implies that cool accreting gas is being replenished from somewhere, and gradually cooling WIM gas is a likely source. In both the North and South Galactic hemispheres, WIM gas is observed to be infalling at 10 $\mathrm{km\,s^{-1}}$ in a manner consistent with a layer of gas accreting material at a rate of 1 $M_\odot$/yr, although it is not certain whether this is a global phenomenon or local only to the Solar neighborhood. (Haffner et al., 2003; Reynolds, 2004; Putman et al., 2012)

Evidence of the cooling process undergone by halo gas can be seen in the form of high- and intermediate-velocity clouds (HVCs and IVCs) which populate the CGM. Both HVCs and IVCs are well-studied, and have been defined and grouped into complexes using HI 21-cm emission data (Wakker & van Woerden, 1991; Wakker et al., 2007; Wakker et al., 2008; Westmeier, 2018). Neutral, weakly- and highly-ionized gas associated with these clouds has also been detected in absorption along sightlines to quasars (Murphy et al., 1995; Sembach et al., 2003; Shull et al., 2009; Ben Bekhti et al., 2012; Lehner et al., 2012; Richter, 2017; Clark et al., 2022) and halo stars (Lehner & Howk, 2010; Lehner & Howk, 2011; Bish et al., 2019; Werk et al., 2019; Lehner et al., 2022).

HVCs and IVCs are typically studied as two separate populations. High-velocity clouds ($|v| > 90$ $\mathrm{km\,s^{-1}}$) are found farthest from the disk, with typical distances of 5-15 kpc and z-heights of 3-9 kpc (Wakker & van Woerden, 1997; Thom et al., 2006, 2008; Wakker et al., 2007; Wakker et al., 2008; Putman et al., 2012; Lehner et al., 2022). These complexes of neutral and ionized gas extend across 65-90% of the sky (Fox et al., 2006; Collins et al., 2009; Shull et al., 2009; Lehner et al., 2012; Richter, 2017), but likely constitute only a

small fraction of the Milky Way's total halo mass (Putman et al., 2012). The largest HVCs include the Magellanic System, Complex C, and Complex A. Intermediate-velocity clouds ($25 < |v| < 90$ km s^{-1}) are found closer to the disk at z-heights of $\sim 0.5 - 3$ kpc (Kuntz & Danly, 1996; Wakker, 2001; Smoker et al., 2011). IVCs are predominantly moving toward the disk at negative velocities (Wakker, 2001), and because their metallicities are consistent with that of ISM gas they are thought to contain material that was once in the Galaxy's disk. In contrast, HVCs have lower metallicities of 0.1–1.0 $Z_\odot$ and velocities inconsistent with Galactic rotation, and are therefore often assumed to have an origin external to the disk (Putman et al., 2012). Some evidence suggests they may form from cooling CGM gas (Thom et al., 2006; Peek et al., 2007).

More recently, a large population of cold HI clouds embedded in the warm ambient gas of the disk-halo interface has been identified as further evidence of gas cooling closer to the disk (Lockman et al., 2002; Stanimirović et al., 2006; Ford et al., 2008; Ford et al., 2010; Peek et al., 2011; Saul et al., 2012). These small, discrete clouds move in a manner consistent with Galactic rotation at z-heights of 1-2 kpc (). Although they are moving at intermediate velocities, they may represent a population distinct from the larger classical IVCs. With the GALFA-HI survey, Saul et al. (2012) classified these compact clouds into two types: colder ($T < 5,000$ K), roughly uniformly-distributed clouds with motion similar to the disk, and warmer ($T > 5,000$ K) clouds with a patchier distribution that are predominantly moving toward the disk (Saul et al., 2012; Putman et al., 2012).

A range of models have been put forward to explain how these clouds might cool and condense out of the surrounding medium (Bregman, 1980; Norman & Ikeuchi, 1989; Houck & Bregman, 1990; Fraternali & Binney, 2008; Marasco et al., 2012; Joung et al., 2012a). In some models, thermal instabilities prompt the formation of warm clouds in the Galactic corona, which then rain onto the disk as HVCs (Maller & Bullock, 2004; Sommer-Larsen, 2006; Peek et al., 2008). There is still debate about the extent to which thermal instabilities can drive cooling in such hot, low-metallicity gas (Binney et al., 2009), but this may be possible with "feedback-induced cooling," where metal-rich material ejected from the disk

mixes with hot coronal material and stimulates enhanced cooling (Marinacci et al., 2010, 2012; Fraternali, 2017; Howk et al., 2018). One picture that has begun to emerge from such models is one in which HVCs sink towards the disk, where they decelerate and fragment as they interact with outflowing material and begin to mix with the WIM at the disk-halo interface (Lehner & Howk, 2011; Cornuault et al., 2018; Melso et al., 2019). The degree of mixing largely determines how much the cloud is decelerated, but in any case these accreting clouds generally retain most of their material (Melso et al., 2019). At this stage they have slowed enough to become intermediate- or low-velocity clouds (Howk et al., 2018), and become heated as the fragmented cloud interacts with the warm gas layer. As the fragments continue to sink toward the disk where the ambient medium is more dense and the pressure is higher, they become buoyant and once again begin to cool and grow (Heitsch & Putman, 2009; Putman et al., 2012). The result is a string of smaller clouds embedded in the WIM and rotating with the Galaxy.

Less is known about the lower-velocity ($v < 150\ \mathrm{km\,s^{-1}}$) material accreting onto galaxies, as it is difficult to disentangle the signals of low-velocity halo gas from the low-velocity disk gas in the foreground. Recently the QuaStar survey (Bish et al., 2021) used a spectral differencing technique to show that the bulk of low-velocity ionized gas in the Galactic halo must sit close to the disk ($z \lesssim 5$ kpc). Such low-velocity gas has been observed in other galaxies too. Some of the strongest evidence comes from Zheng et al. (2017), who found a disk-wide ionized layer of warm extraplanar gas accreting onto M33 at an estimated height of $z = 1.5$ kpc above the disk. Similar absorption component structure from a range of metal ions (e.g. SiII, SiIV, CIV) indicate that this gas is likely multiphase.

In order to obtain a full picture of what this multiphase, extraplanar material is doing, and how it might provide fuel necessary to sustain star formation, we must observe it over a wide range of temperatures and phases. Studies in the UV are most efficient for this work since the absorption features of ions in a number of different ionization states fall in this wavelength regime. Furthermore, our vantage point within the Milky Way, which offers an abundance of halo-probing sightlines across the sky, means we are in a unique position to study Milky Way accretion in detail.

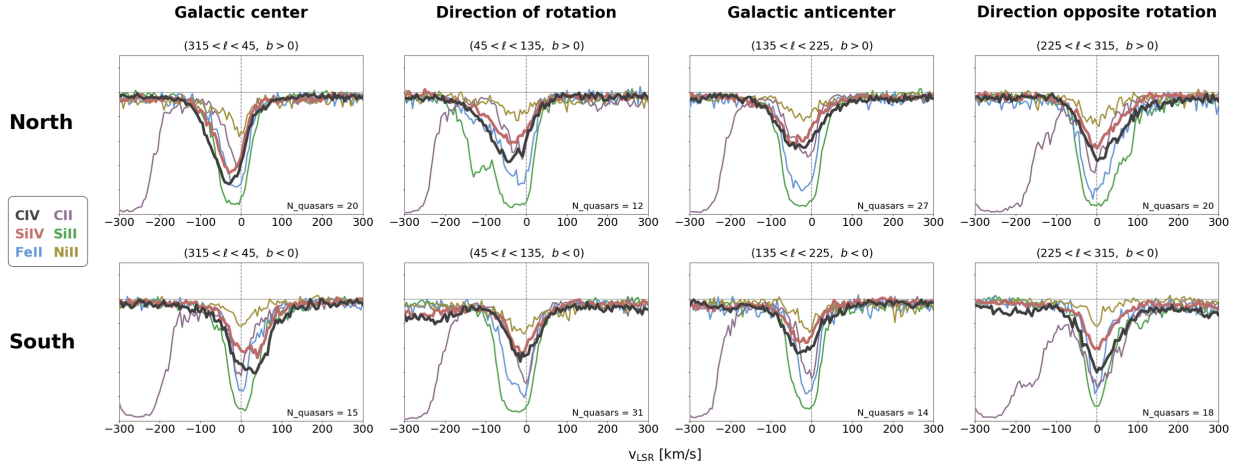

Figure 4.1.1: STACKED SPECTRA. Stacked spectra for each ion in eight regions of the sky. In the top row, Northern Galactic hemisphere lines of sight are stacked in directions (from left) toward Galactic center, toward the direction of Galactic rotation, away from Galactic center (aka Galactic anticenter), and in the direction opposite Galactic rotation. The bottom row shows the same directions for sightlines in the South Galactic hemisphere. Each colored line traces a different metal ion, and all transitions are centered at $v_{\rm LSR}= 0$ for each sightline. The strong absorption feature at $v < 150 {\rm km\,s^{-1}}$ in C II* is a different CII transition that falls near C II*, and is not an indication of absorption at those velocities.

In this paper we analyze absorption from a wide range of metal ions and emission from hydrogen over the full sky to examine how the kinematics and distribution of gas in the Milky Way's disk-halo interface differs as a function of gas phase and temperature. Previous studies have focused on IVC and HVC absorption ((e.g. Richter, 2017; Fox et al., 2019)) but have largely ignored the low-velocity material in the disk-halo interface that is difficult to separate from interstellar gas. Here, we focus primarily on the low-velocity gas. This paper is organized as follows: §4.2 describes the data and sample selection process in detail. §4.3 describes our methods for reducing spectra, measuring velocities of absorption features, and decontaminating the sample from known IVC and HVC absorption. §4.4 presents the results showing the differential infall rates of ions tracing gas at different temperatures, and §4.5 describes a kinematic model against which we compare our results. §4.6 considers the implications of our findings, and §4.7 summarizes the findings of this work.

4.2 Data and Sample

Our sample consists of 147 quasars observed with *HST*/COS, and complementary 21-cm and Hα emission-line data in the same direction as those sightlines. The high sensitivity of COS relative to other UV spectrographs makes these spectra ideal for detecting and accurately measuring absorption features for a range of ions. The emission-line data allow us to track both neutral and ionized Hydrogen at high spectral resolution to supplement our kinematic analysis. The sample includes sightlines at all Galactic latitudes where data were available. For our analysis of inflows and outflows in section 4.3 and 4.4.2, we use only the 46 sightlines at $|b| > 60°$, since high-latitude sightlines best capture the motion of gas toward and away from the disk. For our kinematic modeling of disk gas, described in section 4.5, we use only the 101 sightlines at $|b| > 60°$, since low-latitude sightlines provide the best global constraints on the motion of gas close to the disk.

4.2.1 HST/COS Spectra

The archival quasar spectra used in this work were observed with the G160M and G130M gratings on the Cosmic Origins Spectrograph (COS; Froning & Green, 2009; Green et al., 2012) as part of many different observing programs with a range of science goals. The total wavelength coverage of the two gratings is roughly 1132-1804 Å, but the coverage of each spectrum varies depending on the grating and the central wavelength used. Specifically, we select sightlines which allow us to measure absorption features of a number of ions including C IV, Si IV, C II*, Si II, S II, Fe II, N V, and Ni II. The velocity resolution ranges from 15−20 km/s. The median S/N of the COS spectra in this sample is $\gtrsim$ XX for the G160M grating and $\gtrsim$ XX for the G130M grating.

We used data products from the COS-Gal (Zheng et al., 2019), a catalog of quasars in the Hubble Spectroscopic Legacy Archive (HSLA; Peeples et al. 2017), when available. Otherwise we retrieved processed spectra directly from the HSLA or raw spectra from the HST archives. 143 COS-Gal sightlines make up the bulk of our sample.

We measured UV metal line transitions for the following ions: C IV $\lambda\lambda$1548, 1550 Å, Si IV $\lambda\lambda$1393, 1402 Å, C II* λ1335 Å, Si II λ1190, 1193, 1260, 1304, 1526 Å, S II $\lambda\lambda$1250, 1253, 1259 Å, Fe II λ1144, 1608, 1611 Å, N V $\lambda\lambda$1238, 1242 Å, and Ni II λ1317 Å, λ1370 Å. Because S II λ1259 is blended with a $v_{\rm LSR} \sim -350 {\rm km\,s^{-1}}$ component of Si II λ1260, we do not include S II λ1259 in our analysis.Furthermore, Fe II and Si II were excluded from analysis because of data quality issues described below in §4.2.1.

No co-adding was required for spectra obtained from the HSLA. We performed a co-added flux comparison among `COADD_X1D` and HSLA data for a set of bright UV targets to confirm that the spectral co-addition routines from HSLA and `COADD_X1D` produce comparable line profiles and co-added flux levels. After co-adding, continuum fitting was performed by eye with the `linetools` package[1], an open-source code for analysis of 1D spectra. Finally, for consistency spectra were rebinned using SpectRes, a spectral resampling tool (Carnall, 2017).

In Figure 4.1.1, examples of the stacked spectra can be seen for each ion in eight regions of the sky. In the top row, Northern Galactic hemisphere lines of sight are stacked in directions (from left) toward Galactic center, toward the direction of Galactic rotation, away from Galactic center (aka Galactic anticenter), and in the direction opposite Galactic rotation. The bottom row shows the same directions for sightlines in the South Galactic hemisphere. Each colored line traces a different metal ion, and all transitions are centered at $v_{\rm LSR} = 0$ for each sightline. These stacked spectra show how the absorption features of the ions in our sample differ relative to one another.

Data Quality Issues

The HSLA does not make any corrections to reconcile the independently-determined wavelength solutions of the G160M and G130M gratings. As a result, we find that ions with multiple transitions that fall on different gratings occasionally have a significant offset on the order of $\sim$5 $\rm km\,s^{-1}$ in line centroids. This effect is most significant for FeII, which has

[1]https://github.com/linetools/linetools

transitions at 1144 Å and 1526 Å– one on each edge of the G130M and G160M gratings, respectively. The magnitude of the offset for FeII ranges from $1 - 7\mathrm{km\,s^{-1}}$, where approximately YY%of FeII measurements are unable to be jointly fit by self-consistent Voigt profiles because the offset is $> 5\mathrm{km\,s^{-1}}$, which is too large for the fitting algorithm. The offset does not happen systematically in one direction or another, and is not something that can be easily corrected. We also note that its magnitude is within the accuracy of the COS wavelength solution, which is 7.5 $\mathrm{km\,s^{-1}}$, or half of a resolution element for the FUV M gratings we used in this study.

This offset also affects Si II (λ1190, 1193, 1260, 1304, 1526 Å), though the shift is less significant and the greater number of available transitions allow for more consistent velocity centroid fitting (described in §3). However, the vast majority of Si II lines were badly saturated, dealing another blow to the accuracy of our velocity centroid measurements. For this reason we have chosen to exclude the Fe II and Si II measurements from our analysis.

4.2.2 HI and Hα Survey Data

Neutral hydrogen gas can be observed in 21-cm emission and has been extensively mapped in the Milky Way by various surveys (Kalberla et al., 2005; Kalberla & Haud, 2015; Winkel et al., 2016; HI4PI Collaboration et al., 2016), so its distribution is much better constrained than that of warm gas, which can only be measured in absorption in the direction of bright background sources. We use HI4PI Survey data (HI4PI Collaboration et al., 2016) to obtain velocities and column densities of HI gas at $|v| < 150$ $\mathrm{km\,s^{-1}}$ in the direction of each COS sightline. Column densities are measured within a radius of $16'$ from the sightline coordinates to match the beam size for the HI4PI survey.

To supplement the HI data, we also measure velocities and column densities of Hα emission mapped by the Wisconsin H-Alpha Mapper (WHAM) Survey (Haffner et al., 2003, 2010). WHAM covers Galactic Hα emission at roughly $|v_{LSR}| <$100 $\mathrm{km\,s^{-1}}$ with a velocity resolution of 12 $\mathrm{km\,s^{-1}}$. This emission traces ionized hydrogen at higher temperatures, providing the opportunity to measure well-mapped hydrogen gas in two different ionization states for each absorption sightline in our sample.

4.3 Analysis

4.3.1 Voigt Profile Fitting

After data reduction was complete, we identified absorption lines of interest and performed Voigt profile fitting to determine column density N, radial velocity v, and Doppler parameter $b_{\rm D}$ for each component. This process was carried out in two stages. First, we used the `PyIGM IGMGUESSES` GUI[2] to identify absorption features by eye and obtain initial guesses for the parameters of the Voigt profile fit. Absorption line systems at higher redshifts often produce absorption features that overlap with rest-wavelength features of interest, resulting in contamination. Such contaminating lines can be easily identified when they fall near a multiplet transition because unlike rest-frame absorption features they do not repeat for all lines in the group. If any contamination was found near ions of interest (C IV, Si IV, C II*, Si II, S II, N V, Ni II, Fe II), we systematically fit all absorption originating from higher redshifts to identify the contaminating features. In each spectrum, all absorption features within ± 400 km s^{-1} of transitions on the "Strong" ISM line list were examined and fit using the GUI.

Next, the best-fit line profile parameters were determined using the initial guesses from `PyIGM` as input for veeper[3] (Burchett et al., 2015), a Python-based Voigt profile fitter for CGM absorption lines. The veeper Voigt profile fitting algorithm is based on a Levenberg–Marquardt optimization algorithm, and corrects for the unique COS Line Spread Function (Ghavamian et al., 2009). We first attempt to fit a single component to absorption lines, but often have to add additional components for the fits to converge. Generally, our line profile fits use the minimum number of components to account for the optical depth in each profile. By design, the Veeper fits multiple transitions simultaneously.

The resulting best-fit line profiles determined by the Veeper were checked by eye for quality to identify any absorption components that the algorithm could not properly fit.

[2]https://github.com/pyigm/pyigm

[3]https://github.com/mattcwilde/veeper

When this issue occurred it was typically for one of a few reasons: the S/N of the spectrum was too low, absorption features were extremely saturated, or the initial guesses simply did not lead to an acceptable fit. Additionally, spectral regions near the edge of a chip often suffer from noise and large flux errors. Particularly low S/N regions such as these are rejected by the Veeper algorithm and any lines in those regions are not fit. In some other cases a reliable fit could not be obtained because the absorption features were badly saturated. As discussed in 4.2.1, line saturation was most common for Si II. If an ion has even one unsaturated line, however, it is usually possible to obtain a fit. Lastly, sometimes a poor fit was obtained because the initial guesses input to the algorithm were not close enough to parameter values which resulted in an acceptable fit. In these cases the spectra were re-examined to determine if any contaminating high-redshift absorption was interfering with the fit, and initial guesses for parameter values were adjusted. To improve the quality of fits, some single-component absorbers were manually split into multiple components.

Our final analysis focuses on absorption components that are well-fit by Voigt profiles using the above methods. In total, we fit Voigt profiles to XX/YY (ZZ%) components of C IV, XX/YY (ZZ%) of Si IV, XX/YY (ZZ%) of C II*, XX/YY (ZZ%) of Si II, XX/YY (ZZ%) of S II, XX/YY (ZZ%) of N V, and XX/YY (ZZ%) of Ni II. These well-fit absorption lines are present in the spectra of 143 total QSOs observed with COS. Because unresolved saturation affects the vast majority of these lines, we generally do not analyze the fitted column densities, but instead focus on the absorption line velocity distributions in the v_{LSR} restframe. Absorption line velocity centroids are generally well constrained to within a few $km\,s^{-1}$.

In many cases, the individual metal ion transitions along a sightline have more than one absorption component and fitting multiple Voigt profiles is required. In our analysis of global CGM gas kinematics, we use a single weighted velocity for each metal ion. We weight the sightlines by column density N rather than $\log N$. Weighting by N is more conservative than $\log N$, since it doesn't give disproportionate weight to fast-moving material over the main lower-velocity component (which generally has higher column density). That said, we

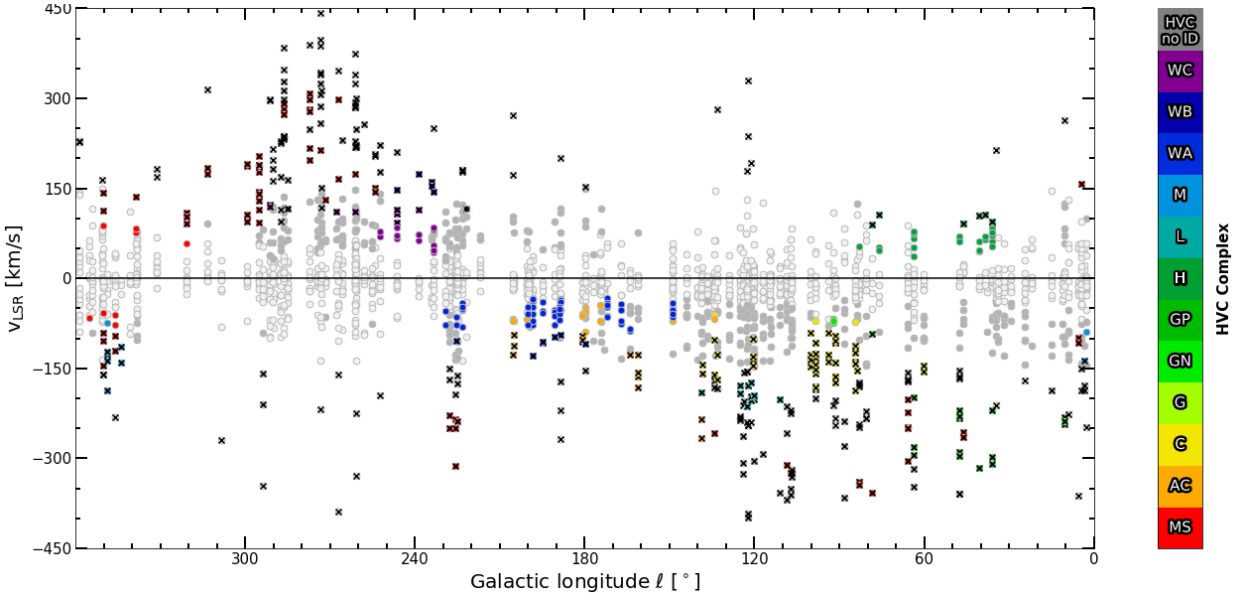

Figure 4.3.1: Absorption components associated with HVCs. All measured absorption components in position-velocity space. Filled circles are components that are associated with HVCs in the Wakker & van Woerden catalog (Wakker & van Woerden, 1991) using criteria established by Peek et al. (2008) (see §4.3.3). Color indicates the name of the associated HVC complex, if any. Open circles are not associated with any HVC. An 'x' marks HVC components which have been excluded from the sample.

examined several different methods of weighting the fitted absorption velocity centroids of multiple components, and found that the impact on the results is insignificant.

Because our aim is to constrain velocities of extraplanar material, we consider only sightlines at Galactic latitudes of $|b|$ >30, which place the most robust constraints on infall and outflow velocities along the lines of sight. For the purposes of this analysis, we use the term 'infall velocity" to describe the lower limit on motion in the z-direction given by v_{obs}sinb. Throughout this work, all data are shifted to the local standard of rest frame.

4.3.2 HI and Hα Brightness Temperature Profiles

Brightness temperature profiles from the HI4PI and WHAM surveys were used to measure total column density and centroid velocity of HI and Hα in the direction of each sightline in the sample. Reduced data cubes for both surveys are publicly available[4,5]. HI 21-cm emission line data included emission within our full velocity range of $|v| < 150$ km s^{-1} , and Hα data included velocities of $|v| \lesssim 100$ km s^{-1} . Gaussian components were fit by eye to the HI profiles so that components corresponding to HVCs could be identified and excluded from analysis (see §4.3.3). For these data we are mainly interested in the velocity distribution in the v_{LSR} rest frame, and so the total line fluxes are generally not used. In every case, the emission-lines are well-detected and well-fit by Gaussian components.

4.3.3 HVC and LVHC Contamination

While HVCs are important for understanding the origin and fate of a galaxy's halo gas, they are too distant and obey a pattern too random and complex to be an informative component of global kinematic models of the disk & disk-halo interface. For that reason they are generally excluded from such models.

---

[4]https://www.astro.uni-bonn.de/hisurvey/AllSky_gauss/

[5]http://www.astro.wisc.edu/wham-site/wham-sky-survey/wham-ss

If we wish to make accurate comparisons to global kinematic models that describe the motion of gas in the Milky Way's disk and disk-halo interface, and these models do not account for HVCs, any absorption features originating from HVCs should be excluded from our data. To determine which components are associated with HVCs, we take the approach of Saul et al. (2012), which measures the distance in position-velocity space between observed gas and catalogued HVCs to determine whether the two are associated. Following Saul et al. (2012), we use the Wakker & van Woerden catalog of HVCs (Wakker & van Woerden, 1991), which includes coordinates and velocities of 616 HVCs across the sky and identifies their membership in known HVC complexes. For each HVC, we then calculate a distance parameter for each measured absorption component, as defined by Peek et al. (2008):

$$D = \sqrt{\Theta^2 + f^2(\delta v)^2}, \tag{4.1}$$

where Θ is the angular distance between the measured gas and the catalog HVC, δv is the difference in velocity between the two, and f is a conversion factor which Peek et al. (2008) set equal to $0°.5\ (\mathrm{km\,s^{-1}})^{-1}$. Using a clustering algorithm with simulated HVCs, Peek et al. (2008) determined that clouds within a complex typically have $D < 25°$.

Figure 4.3.1 places all measured absorption components in position-velocity space. Filled circles are components with $D < 25°$, meaning they are associated with a HVC complex in the Wakker & van Woerden catalog. The color of the circle indicates which complex the component is most strongly associated with, if any. HVC components excluded from the sample are marked with an 'x'. Our criteria for excluding HVC components from the sample are as follows: exclude (1) all components with $|v| > 150\ \mathrm{km\,s^{-1}}$, (2) all components with $|v| > 90\ \mathrm{km\,s^{-1}}$ and $D < 25°$, unless they are associated with Complexes G (green) or AC (orange) or not associated with a known complex (grey), and (3) all components associated with the low-velocity halo clouds L5 and L6 identified in Peek et al. (2009).

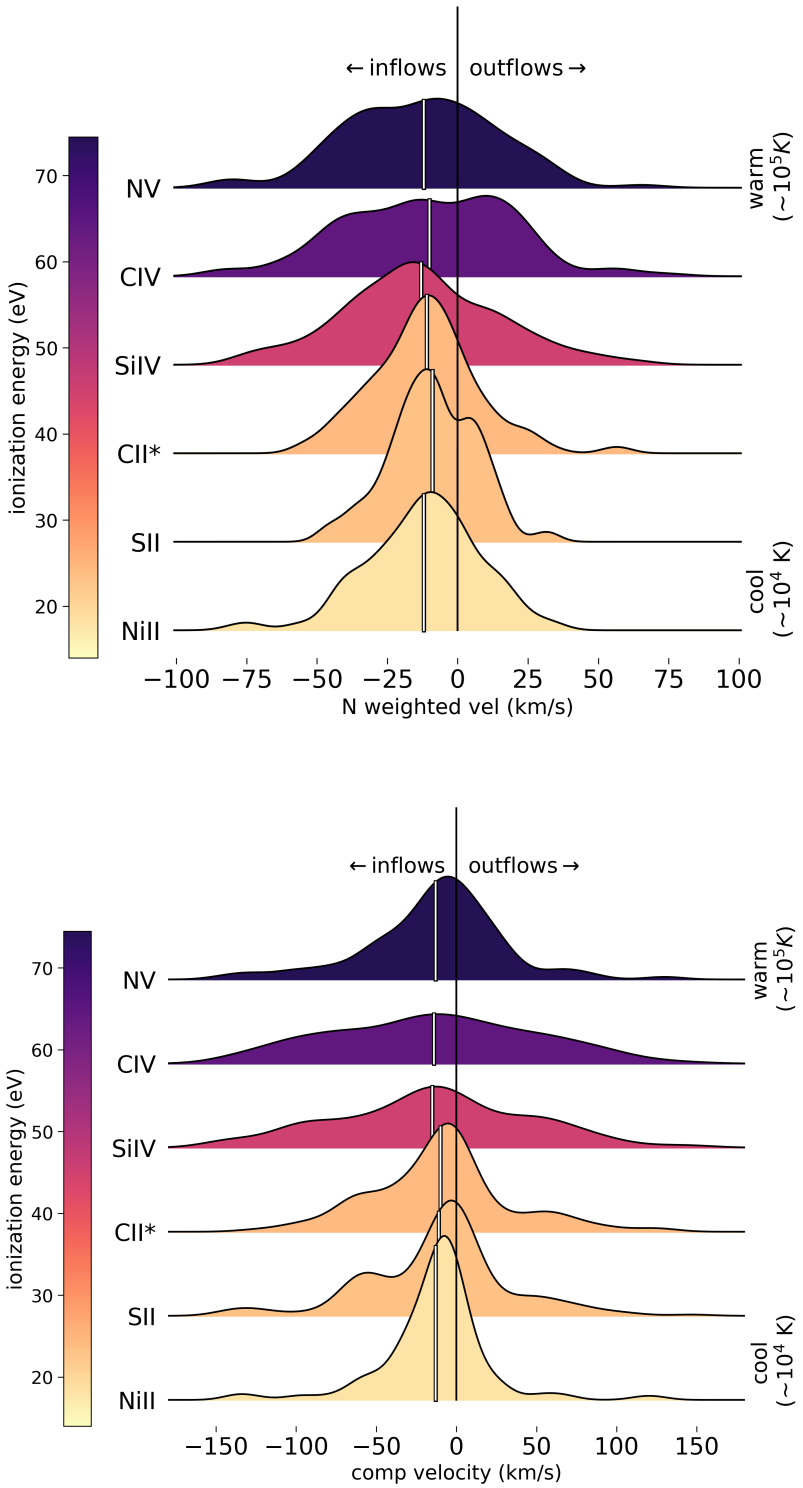

Figure 4.3.2: VELOCITY DISTRIBUTIONS BY ION. Normalized column density-weighted (top) and individual component (bottom) velocity distributions for each measured ion. Colors represent the ionization energy of the ions, with ionization energies corresponding to higher temperature at the top. The vertical solid lines indicate the mean value of each distribution. As a point of reference, dashed lines in every panel pass through $v_{LSR} = 0$. Note that the velocity range on the x-axis is different for the two panels.

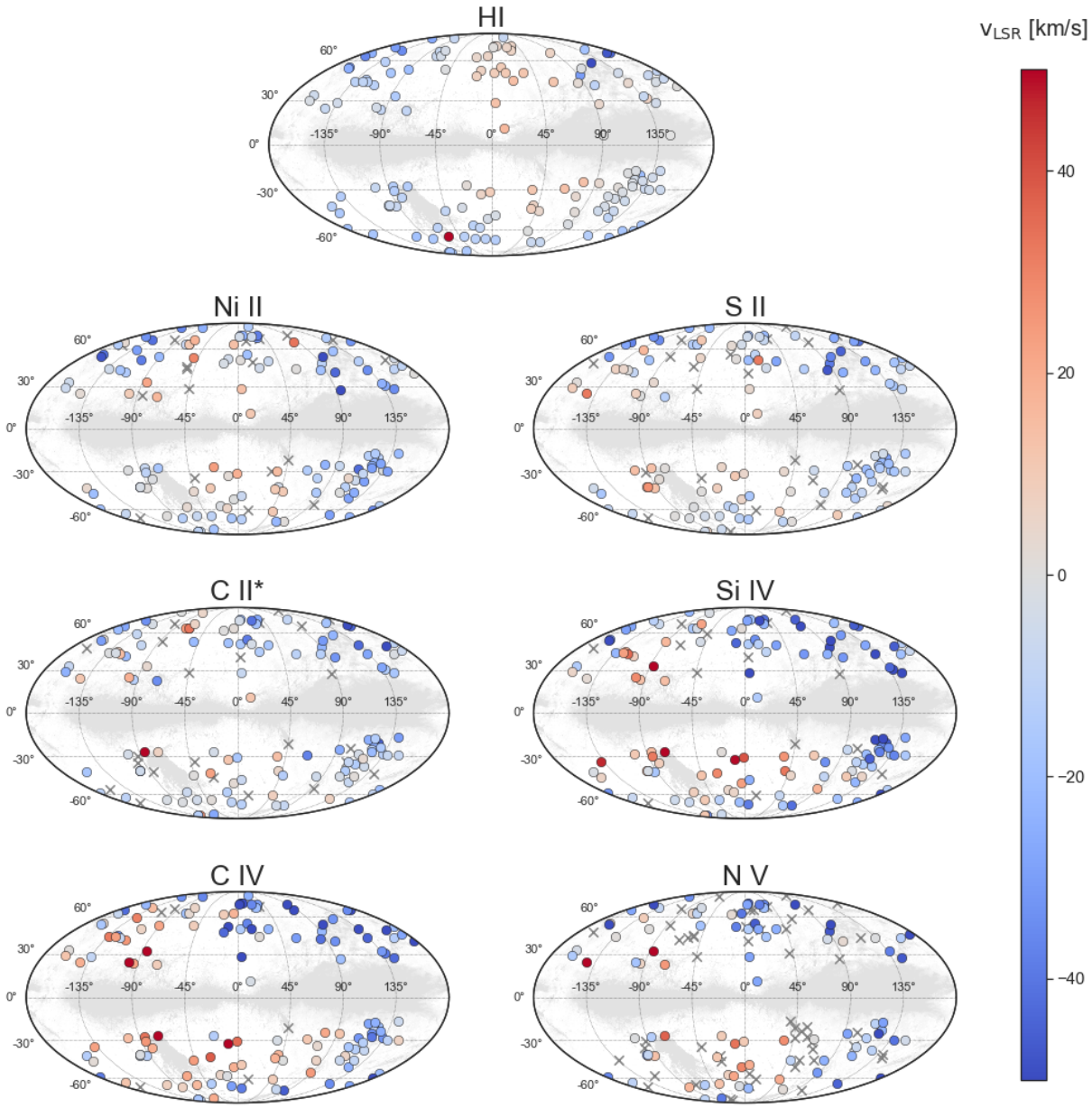

Figure 4.3.3: Velocity Skymaps. Skymaps showing the N-weighted velocity of each sightline for all ions. In each ion map, an 'x' marks the location of sightlines for which there is no low-velocity absorption data, either because no absorption features above the detection threshold were present, or because the spectrum for the sightline did not cover the wavelength of that transition. HI velocities and column densities are measured using brightness temperature profiles from the HI4PI survey as described in §4.2.2 (HI4PI Collaboration et al., 2016). For all other ions, velocities are measured as described in section §4.3.1. The grey shading shows the distribution of HI gas in the Milky Way.

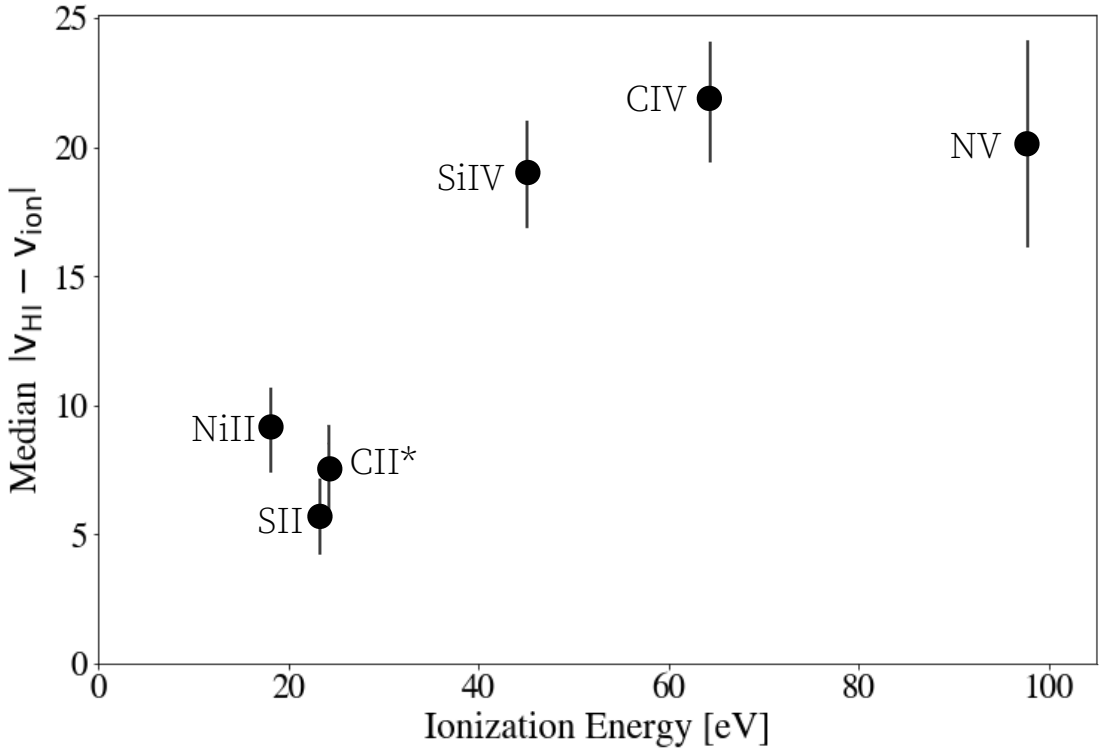

Figure 4.3.4: Differential infall rates of cool and warm-hot ions. Difference in median infall rate between neutral hydrogen and a range of ions which trace cool ($T \lesssim 10^4$ K) and warm-hot ($10^4 \lesssim T \lesssim 10^5$ K) gas. These results indicate that warmer gas is infalling towards the disk with greater velocity.

4.4 Results

Table 4.1 provides a summary of results for all ions. Figure 4.3.2 shows the velocity distributions for each ion by sightline and by component. Lower ions exhibit inflow and outflow components which become less defined and more extended in velocity space with increasing ionization energy. This is expected if higher ions are tracing higher-temperature gas that is more diffuse and well-mixed. In general, most of the distributions have three blended components: the strongest a central peak at small negative velocities, with two weaker components at larger negative velocities and small positive velocities. The presence of components at both positive and negative velocities suggests that inflow and outflow are occurring simultaneously, if not cospatially.

The column density-weighted velocities for each sightline are mapped on the sky over HI column density maps in Figure 4.3.3. It is apparent from these maps that the regions where outflowing H I can be seen ($\ell \sim 0$) do not match the regions where higher ions like Si IV, C IV, and N V are outflowing ($\ell \sim -90$). In H I, the region of outflowing gas coincides roughly with the location of the Fermi bubbles (Su et al., 2010; Dobler et al., 2010).

4.4.1 Differential Infall and the Multiphase Nature of Accreting Gas

Absorption line studies have demonstrated that the scale height of gas varies at different temperatures (Bowen et al., 2008; Savage & Wakker, 2009). Cooler gas (traced by Ni II, S II, and C II* in absorption) has higher filling factors close to the disk, while warm-hot "transition-temperature" gas (traced by Si IV and C IV) sits in puffier layers with filling factors that increase with scale height (Savage & Wakker, 2009; Bowen et al., 2008; Gaensler et al., 2008). For the purposes of this work, we will refer to Ni II, S II, and C II* as the low ions, and Si IV, C IV, and N V as the high ions. This distinction is motivated by the distinct behavior of the two groups discussed below.

In Figure 4.3.4, the difference between the median infall rates for H I and the other ions are plotted as a function of ionization energy to show how infall velocities differ for gas at

varying temperatures. The differential velocities cluster at two values of Δv: the cooler ions Ni II, S II, and C II* (E_i <40 eV) have velocities that differ from H I by 5-10 km s^{-1}, and warmer ions Si IV, C IV, and N V (E_i >40 eV) have velocities that systematically differ from H I by 15-20 km s^{-1}. In the classic two-phase picture for halo clouds in pressure equilibrium with a diffuse, hot, ambient medium (Wolfire et al., 1995), there is no reason to expect that low and high ions move with different velocities relative to each other. We return to this point in the discussion and comment on physical, multi-phase models of the disk-halo interface that may accommodate such behavior.

This trend is broken down further in Figures 4.5.1 and 4.5.2. In Figure 4.5.1, median infall velocities are shown as a function of ionization energy for sightlines in the Northern Galactic hemisphere in red and the Southern hemisphere in blue, with the standard error on the median shaded. It is immediately apparent that the behavior of gas in the North and the South is very different. In the South, gas at all temperatures is accreting at low velocities around -5 km s^{-1}. In the North, however, infall velocities are slightly faster for low ions, and dramatically faster for high ions. We discuss potential reasons for this in §4.6, but the asymmetry of accreting gas in the North and South has been well-documented ().

In Figure 4.5.2, the infall velocities for the North (upper panel) and South (lower panel) are divided once again, into four longitude ranges on the sky: toward Galactic center in green, away from Galactic center in yellow, toward the direction of Galactic rotation in cyan, and away from the direction of Galactic rotation in purple. In the South, infall velocities are relatively small for all ions and roughly the same in all directions, although there is more scatter in these values for the higher ions. In the North, this is not the case, and looking at the infall velocities in different directions tells a more complicated story than is evident in Figure 4.5.1. In the directions toward and away from Galactic center, the high ions are infalling faster than the low ions, with a stronger trend toward Galactic anticenter. Conversely, infall velocities in the direction toward and away from Galactic rotation remain relatively constant across all ions. The velocities are consistent with zero toward antirotation, and $-20 < v < -30$ km s^{-1} in the direction of rotation.

Ion	E_i [eV]	Inflow Detection Rate	Outflow Detection Rate	In+Out Detection Rate	Inflow Column Density [cm^{-2}]	Outflow Column Density [cm^{-2}]	Inflow Velocity [km/s]	Outflow Velocity [km/s]	Accretion Timescale [Myr]	Outflow Timescale [Myr]	Accretion Rate [10^{-6} $M_\odot$ yr^{-1}]	Outflow Rate [10^{-6} $M_\odot$ yr^{-1}]
		f_{North}	f_{North}	f_{North}	$logN_{North}$	$logN_{North}$	v_{North}	v_{North}	t_{North}	t_{North}	$\dot{M}_{in,North}$	$\dot{M}_{out,North}$
		f_{South}	f_{South}	f_{South}	$logN_{South}$	$logN_{South}$	v_{South}	v_{South}	t_{South}	t_{North}	$\dot{M}_{in,South}$	$\dot{M}_{out,South}$
		f_{allsky}	f_{allsky}	f_{allsky}	$logN_{allsky}$	$logN_{allsky}$	v_{allsky}	v_{allsky}	t_{allsky}	t_{allsky}	$\dot{M}_{in,allsky}$	$\dot{M}_{out,allsky}$
Ni II	18.2	0.48	0.19	0.04	13.7	13.2	-29.5	16.9	30	52	5.3	1.0
		0.58	0.05	0.00	13.5	12.3	-15.1	9.6	58	92	1.9	0.1
		0.52	*0.13*	*0.02*	*13.6*	*13.0*	*-20.9*	*14.6*	*42*	*60*	*3.1*	*0.6*
S II	23.3	0.67	0.26	0.19	15.0	13.9	-43.0	34.3	20	26	96.3	5.6
		0.42	0.32	0.21	14.9	14.0	-12.5	20.8	71	42	20.7	4.9
		0.57	*0.28*	*0.20*	*14.9*	*13.9*	*-34.5*	*25.6*	*26*	*34*	*65.4*	*4.6*
C II*	24.4	0.67	0.26	0.26	13.8	13.1	-31.2	28.7	28	31	1.8	0.3
		0.47	0.16	0.05	13.6	13.2	-11.4	25.9	77	34	0.4	0.4
		0.59	*0.22*	*0.17*	*13.8*	*13.2*	*-26.4*	*27.3*	*33*	*32*	*1.3*	*0.4*
Si IV	45.1	0.85	0.41	0.37	13.6	12.5	-40.5	43.9	77	71	10.8	1.0
		0.68	0.68	0.58	13.3	12.8	-43.6	41.2	72	76	6.0	1.8
		0.78	*0.52*	*0.46*	*13.5*	*12.7*	*-40.9*	*42.2*	*77*	*74*	*8.5*	*1.3*
C IV	64.5	0.89	0.67	0.67	14.1	13.2	-45.9	46.1	77	76	20.7	2.6
		0.84	0.74	0.68	13.9	13.8	-52.9	26.9	67	131	15.1	5.6
		0.87	*0.70*	*0.67*	*14.1*	*13.3*	*-46.6*	*36.1*	*76*	*98*	*18.4*	*2.4*
N V	97.9	0.52	0.04	0.04	13.4	11.6	-34.8	8.8	109	431	3.4	0.01
		0.37	0.16	0.00	12.9	12.5	-19.8	15.9	193	239	0.7	0.2
		0.46	*0.09*	*0.02*	*13.2*	*12.2*	*-33.8*	*14.0*	*113*	*273*	*2.4*	*0.1*

Table 4.1: Summary of results for each ion: (1) ionization energy of the ion, (2) covering fraction of the ion, (3) median infall velocity, (4) median accretion timescale, (5) median accretion rate, (6) median outflow velocity, (7) median outflow timescale, (8) median outflow rate.

4.4.2 Timescales and Mass Flow Rates

The gas velocities discussed in previous sections are only one part of the accretion story. If we wish to understand the accretion and outflow timescales, along with the corresponding mass flow rates, we must constrain the distances to the extraplanar material. The absorption lines analyzed in the archival QSO spectra do not on their own constrain the distances the gaseous material must traverse in order to reach the Milky Way disk. Fortunately, previous work using both stellar and QSO sightlines to constrain the scale heights of ionized material at the disk-halo interface makes the calculation of timescales and mass flow rates possible.

Our timescale calculation is based upon the work of Savage & Wakker (2009), who analyzed the scale heights of various metal ions in different ionization states. Of interest here are the relative values of the different scale heights for warm-hot "transitional" temperature gas traced by C IV (a high-ion), with $h \approx 3.6 \pm 1$ kpc, and the warm ionized medium tracer, Al III (a low-ion), with $h \approx 0.90 \pm 0.5$ kpc. Thus, the high-ion to low-ion scale height ratio ranges from $3-5:1$. Previous work has shown that singly and doubly-ionized low-ionization species observed in absorption in the CGM tend to track each other in both column density and kinematics (e.g. Werk et al., 2013). Thus, it is reasonable to assume that the Al III analyzed by Savage & Wakker (2009) and the singly-ionized metal species we analyze here (S II , C II*, and Ni II) track the same WIM material as Al III. Under these simplifying assumptions, we calculate accretion and outflow timescales as

$$t_{acc} = h_{\rm acc}/v \tag{4.2}$$

where $h_{\rm acc}$ is the height of the gas layer, and v is the median velocity for all absorption components moving at a velocity greater than the COS wavelength calibration error, or $|v| > 7.5 {\rm km\,s^{-1}}$ [6]. Excluding components at velocities smaller than the wavelength error

[6] See COS Instrument Science Report 2018-25 https://www.stsci.edu/files/live/sites/www/files/home/hst/instrumentation/cos/documentation/instrument-science-reports-isrs/_documents/ISR2018_25.pdf

yields a very conservative lower limit on the covering fractions and gas flow timescales we report. Following the examples of other gas flow studies (e.g., Fox et al., 2019; Clark et al., 2022), we calculate accretion and outflow separately.

Within the errors, the gas scale height ratio for high to low ions found by Savage & Wakker (2009) is similar to the accretion velocity ratio we measure for high to low ions, where $v_{acc,CIV}$ / $v_{acc,CII\star} \approx 3 - 4$, as seen in Figure 4.3.4. Thus, the timescales for these two disparate ionization-state gas phases to reach the disk are similar since the difference in scale heights cancels out the difference in velocities. This similarity may imply a physical connection between gas phases, not unlike the turbulent and conductive interfaces that have been proposed to explain the multiphase nature of both IVCs and HVCs (e.g. Kwak et al., 2015; Armillotta et al., 2017). The absolute values of these accretion and outflow timescales are less certain. Following the example of Fox et al. (2019), we calculate timescales and gas flow rates separately for accreting and outflowing gas. These timescales in Myr are listed in Table 4.1. For example, taking the Savage & Wakker (2009) scale heights at face value, and using the average infall velocities listed in Table 4.1, we obtain an accretion timescale of approximately 75 Myr for the low-velocity material to reach the disk.

The approach to calculating the mass flow rates of predominantly low-velocity material in the disk-halo interface builds upon the kinematic and ionization modeling approach of Zheng et al. (2017). Using O-star sightlines spread across the face of M33, Zheng et al. (2017) are able to model the absorption from intermediate ionization state gas traced by Si IV that is redshifted relative to the ISM of M33 as an accreting layer of gas at the disk-halo interface. If we assume that the Northern sightlines in our sample are intersecting a similar layer at the Milky Way disk-halo interface, we can make a similar cylindrical geometry calculation for the total mass of the layer traced by our detected Si IV . Because the Southern Galactic lines of sight do not show a similar accretion pattern, we exclude them from this calculation.

Assuming a cylindrical geometry for the accreting/outflowing layers with height $z_{\rm ion}$ and radius $R_{\rm ion}$, the total mass of the detected accreting/outflowing layer is,

$$M_{\rm ion} = (\pi R_{\rm ion}^2) N_{\rm ion} m_{\rm ion} f_{\rm ion} \tag{4.3}$$

where $R_{\rm ion,acc}^2$ is the radius of the accreting layer, $N_{\rm ion}$ is the median column density of the ion for all sightlines, $m_{\rm ion}$ is the mass of the ion, and $f_{\rm ion}$ is the covering fraction of the ion. For $R_{\rm ion,acc}$, we adopt the minimum possible radius of the accreting layer given that our quasar sightlines probe latitudes $|b| > 60°$, $R_{\rm ion,acc}$ ~tan(60°) kpc, assuming the accreting layer covers the whole star-forming disk. We derive the accretion/outflow rates for each ion using the mass and timescale calculations above:

$$\begin{aligned} \dot{M}_{ion} &= M_{\rm ion}/t_{\rm ion} \\ &= v(\pi R_{\rm ion}^2) N_{\rm ion} m_{\rm ion}/z_{\rm ion} \end{aligned} \tag{4.4}$$

The accretion rates for each ion are listed in Table 4.1. To estimate the total gas accretion rate, we use C IV measurements, since the C IV absorption feature is typically strong and unsaturated, and therefore the most reliable. We assume a conservative range of 0.05-0.3 for the fraction of carbon in C IV , and 0.1-1$Z_\odot$ based on the abundances in Asplund et al. 2009. The total gas accretion/outflow rate is given by

$$\dot{M}_{total} = \dot{M}_{ion} \left(\frac{0.1 - 1\, Z_\odot}{Z} \right) \left(\frac{0.05 - 3}{f_{\rm C\,IV}} \right) \tag{4.5}$$

In the North, this yields an estimated total low-velocity gas accretion rate of 0.02-1.8 $M_\odot$/yr and outflow rate of 0.003-0.2 $M_\odot$/yr. In the South, the accretion rate is 0.01-1.3 $M_\odot$/yr and the outflow rate is 0.005-0.5 $M_\odot$/yr. It is interesting to compare these low-velocity gas accretion rates to the estimated accretion rates of HVCs in the literature, which fall in the range 0.08-0.4 $M_\odot$/yr (Putman et al., 2012; Fox et al., 2019). The fact that low-velocity gas accretion rates are roughly similar to HVC accretion rates suggests that

low- and high-velocity gas may accrete as part of the same process – or at the very least, that accreting low-velocity gas is a significant and often overlooked component of gas flows feeding the Milky Way's disk.

4.5 Kinematic Model

Having now measured the kinematics of gas over a range of temperatures at the disk-halo interface, it is informative to examine whether this gas is kinematically consistent with various models of rotating Milky Way disk gas. It is not realistic to attempt to constrain properties on the scale of individual clouds, as this would require either complex assumptions or detailed knowledge of the state of the gas and its environment that are not available to us. For this reason, we focus on constraining the large-scale kinematic properties of the gas.

To do this, we developed a model that predicts the observed velocities along each of our sightlines given a set of parameters that defines the density distribution and motion of the gas. The gas density is modeled as an axisymmetric smooth distribution with density ρ defined in a cylindrical coordinate system as a function of Galactocentric radius R and height z above the Galactic disk. The kinematic properties of the gas in the model are defined by the following parameters: rotational velocity v_{rot} (assuming a flat rotation curve), vertical rotational lag dv/dz, infall velocity v_z, radial scale height R_0, vertical height or scale height h_0, and layer thickness σ.

First, we assume a form for the density distribution. We modeled three distributions for comparison with our data: (1) a 'vertical exponential' model $\rho = \rho_0\, e^{-|z|/h_0}$, where density is constant in R and drops off exponentially in z; (2) a 'radial-vertical exponential' model $\rho = \rho_0\, e^{-R/R_0}\, e^{-|z|/h_0}$, where density drops off exponentially in both R and z; and (3) a 'sandwich' model $\rho = \rho_0\, e^{-(z-z_0)^2/2\sigma^2} + e^{-(z+z_0)^2/2\sigma^2}$, in which two layers of gas sit above and below the disk. The sandwich model is motivated by the behavior of gas in TIGRESS, a high-resolution box simulation of the local interstellar medium, which predicts layers of warm extraplanar gas sitting roughly 1-2 kpc from the disk (Kim & Ostriker, 2017; Kim & Ostriker, 2018).

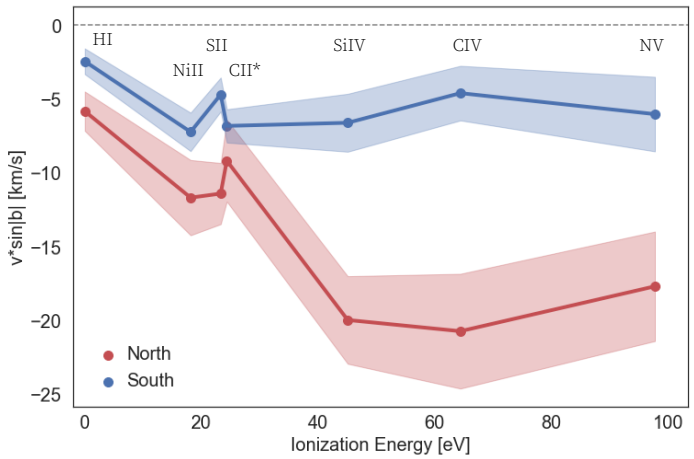

Figure 4.5.1: INFALL VELOCITIES IN THE NORTH VS THE SOUTH. Mean column density-weighted infall velocity ($v_{observed}sinb$) for sightlines at $b > 60°$ as a function of the ionization energy corresponding to each ion. Shaded regions represent the standard error on the mean. Measurements in the Northern Galactic hemisphere are shown in red, and the Southern hemisphere is shown in blue. In the North, warm and warm-hot ions (Si IV, C IV, and N V) in comparison to ions tracing gas at cooler temperatures (H I, Ni II, S II, and C II*).

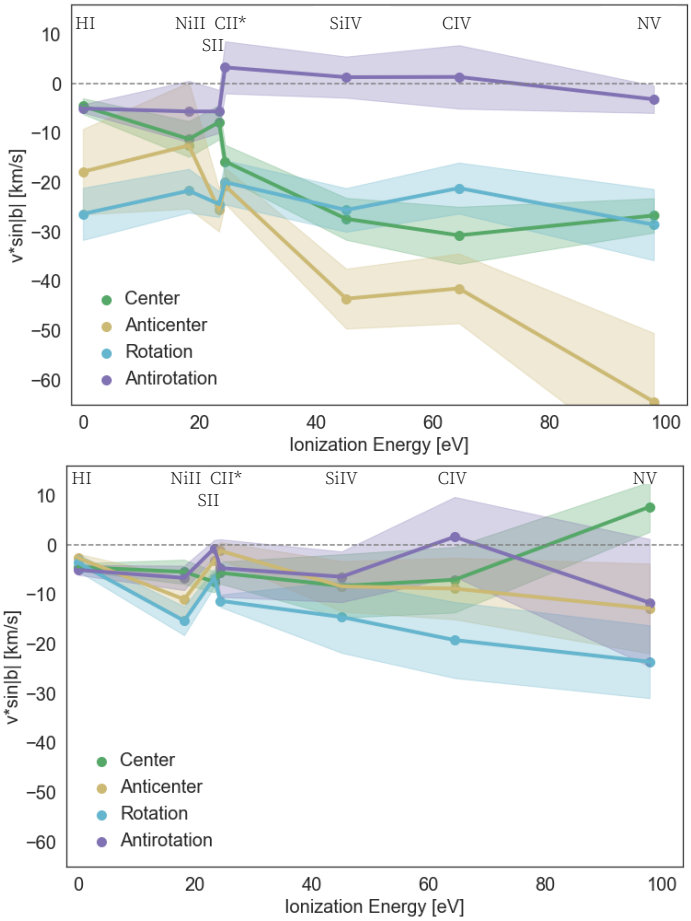

Figure 4.5.2: INFALL VELOCITIES IN FOUR LONGITUDE QUADRANTS. The same as Figure 4.5.1, except Northern (upper panel) and Southern (lower panel) sightlines are further broken down into four longitude quadrants: toward Galactic center in green, Galactic anticenter in yellow, the direction of Galactic rotation in blue, and opposite rotation in purple. Sightlines at $b > 45°$ are shown to increase sample size in each quadrant. In the North, infall velocities are greater for higher ions toward Galactic center and anticenter, but remain roughly constant across all ions toward and away from the direction of rotation.

To determine the optimal density and velocity parameters, the model defines a density field and a velocity field. The distance along each sightline is divided into ~ 0.01 kpc bins out to 50 kpc. The density field is not used directly in parameter fitting, only to weight the velocities in each distance bin. Parameter space is then sampled by a Markov Chain Monte Carlo (MCMC) algorithm[7] assuming Gaussian priors, to determine which parameter values provide the best fit with the measured velocities along each sightline. Because the rotational kinematics of gas close to the disk are poorly constrained by high-latitude sightlines, we use only sightlines at $|b| < 60^\circ$ for fitting.

The best-fit parameters for each ion are shown in Figure 4.5.3. In almost all cases the three models predict the same values for rotational velocity, gas layer thickness, vertical lag, and infall velocity, and no one density distribution is preferred by the model. Rotational velocities range from $214 - 240$ km s^{-1}, with a clear trend of slower rotation for higher ions. Thickness/scale height does not appear to be correlated with ionization state, but it is noteworthy that these values are quite small, at < 400 pc, as compared with the 1-2 kpc range predicted by TIGRESS. Vertical lag is roughly -10 km/s/kpc for all ions and density distributions, and infall velocities range from -17 km s^{-1} to 0 km s^{-1}.

The best-fit infall velocities of the models match what we observe in the South, but don't predict the higher velocities of higher ions in the North (see Figure 4.5.1). This could be a reflection of the fact that the North has more disk-halo interface material that is not kinematically aligned with the gas in the disk. If models are run for Northern sightlines only, the predicted infall velocities become larger, ranging from -30 km s^{-1} to -10 km s^{-1}, better matching what is observed in the North. However, we do not see trend of higher ions having faster infall velocities that is observed in the North (compare the bottom panel of Figure 4.5.3 with Figure 4.5.1). Instead, the kinematic model prefers a physical scenario in which the ionized gas scale heights are very small, <400 pc, but with rather large differential rotation velocities between low and high ionization state material.

[7]This algorithm makes use of the `emcee` package developed by Foreman-Mackey et al. (2013).

Our model follows the examples of previous studies. Marasco & Fraternali (2011) were among the first to study the global kinematics of extraplanar gas by developing a parametric model of the thick disk using HI 21-cm data from the LAB Survey (Kalberla et al., 2005). Qu et al. (2020) developed a model of warm Milky Way gas by fitting measurements of Si IV absorption to a global CGM component and a disk component with exponential dropoff in R and z, using a cloud model rather than a smooth density distribution. Zheng et al. (2017) modeled inflows in M33 as an accreting layer perpendicular to the disk, and found that both Gaussian and exponential models could reproduce the data.

In general, these models predict that infalling disk-halo interface gas sits significantly farther from the disk, in the range $1.6 < h_0 < 6.3$ kpc, and comparable or greater infall velocities, up to -69 $\mathrm{km\,s^{-1}}$ in the North and -110 $\mathrm{km\,s^{-1}}$ for M33. The lag values we find are in general agreement with other models, which predict values of $-8 < v_{lag} < -15$km/s/kpc (Marasco & Fraternali, 2011; Zheng et al., 2017; Qu et al., 2020).

Kinematic models such as these inevitably have limitations that may explain the discrepancies between models, and in comparison to observations. The model described above is axisymmetric and cannot capture behavior that varies as a function of Galactic longitude. It therefore cannot recover the large difference in infall velocities toward Galactic anticenter versus antirotation, for example. It seems likely that the gas kinematics at the disk-halo interface are probably very complex, and models of global kinematic properties are simply too course to capture what is going on. Ultimately, we find that modeling the gas at this level is uninformative to some degree. Empirical analyses, however, are sound and worth pursuing.

4.6 Discussion

It has been well-documented that the Northern and Southern Galactic hemispheres display an overall asymmetry (Putman et al., 2012). This asymmetry is seen in the Galactic warp, which rises higher above the Galactic plane in the North (e.g., Levine et al., 2006); in the distribution of highly-ionized gas, which is much more prevalent in the North (e.g., Danly,

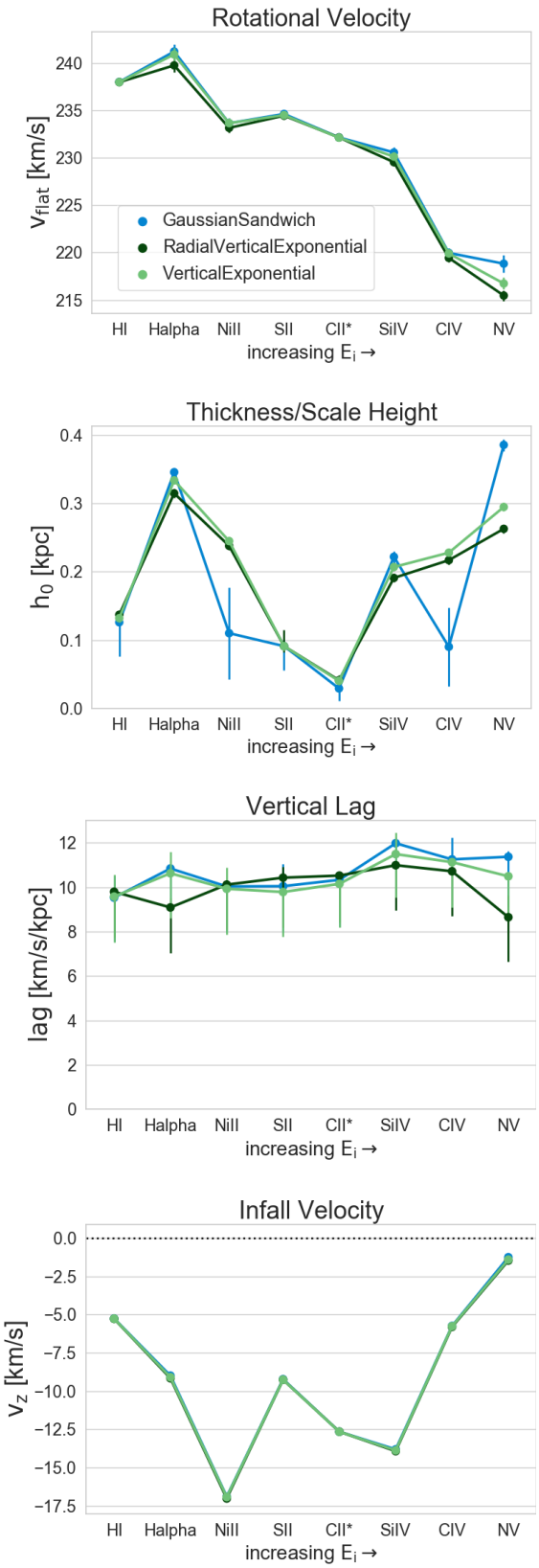

Figure 4.5.3: KINEMATIC MODEL PARAMETERS. Best-fit values of the kinematic models for each ion, assuming three different density distributions: two layers of gas 'sandwiching' the disk above and below the plane, exponential dropoff in both the R and z, and exponential dropoff in z only. The best-fit parameter values are consistent within errors regardless of the density distribution, and the data do not clearly favor any density model over the others.

1986; Savage et al., 2003), the Magellanic System, which dominates infalling material in the South; and the larger number of IVCs and HVCs populating the inner halo in the North (e.g., Nakanishi & Sofue, 2003). These observations indicate that more accretion events are occurring close to the disk in the Northern Galactic hemisphere. In this context, the North-South asymmetry we observe makes sense: the velocity of cooler ions is most likely dominated by material in the ISM, and if there is more warm accreting material in the North, then we expect the median velocities of the higher ions to deviate more from $v_{LSR} = 0$ in the North. Figure 4.5.2 clearly shows that the Northern lines of sight, especially in directions toward Galactic center, anticenter, and antirotation, trace faster-moving material than the lines of sight in the Southern Galactic directions.

Likewise, the differential accretion velocities we find for low and high ionization state gas are considerably more pronounced in the North. Melso et al. (2019) introduces a model of coexisting accretion and outflow at the disk-halo interface that may explain the gas velocities we observe. In their model, generated by tall-box, hydrodynamic ENZO simulations with 2 pc spatial resolution centered on a galaxy disk within ±2.5kpc, injected or accreting cool gas piles up and decelerates at the disk-halo interface as it encounters outflowing material from ongoing supernovae in the disk. In contrast, the lower-density material (in our case, more highly ionized gas) continues on its accretion trajectory, unimpeded. A similar physical picture that has been proposed for gas accretion is the so-called "conveyor belt hypothesis" in which warmer material (more ionized) accretes unimpeded until it slows down, cools, and piles up close to the disk. This picture may help explain our differential velocity results. Specifically, warm infalling clouds that are large enough to reach the DH interface slow down due to drag, and then become a slower-moving overdensity in the surrounding medium that is able to cool (dependent on cloud size, metallicity, cloud cooling/crushing time). This causes a pileup of cooler gas close to the disk, since cooling occurs after the gas has slowed down. Cool, dense gas piling up close to the disk may explain the differential accretion velocities we observe in the inner disk-halo interface. This scenario also naturally explains how different gas phases with different infall velocities can be spatially correlated yet exhibit similar mass accretion rates.

In the HST data, the presence of absorption components at both positive and negative velocities suggests that inflow and outflow are occurring simultaneously, if not co-spatially. Several recent, high-resolution, box simulations predict multiphase thermal wind components, and the coexistence of both inflows and outflows within several kpc of a star-forming galaxy's disk (e.g. Kim & Ostriker, 2018; Gronke & Oh, 2020). In the TIGRESS simulations, the vast majority of the warm-ionized Galactic fountain gas is moving at typical velocities of $\sim 60\ \mathrm{km\,s^{-1}}$, which is somewhat larger than our measurements, although it is not clear if they would predict the warm and cool material to be moving at different velocities in outflows/inflows. We do note however, that the hot, outflowing material is moving considerably faster than the material they call fountain gas. Thus, it is not implausible the cool and warm phases would show different behaviors in accretion and outflow velocities; line-of-sight synthetic spectroscopy in these box simulations would make a very interesting comparison with our observational findings.

One limitation of the small-box simulations is that they do not capture the evolution of Galactic fountain material within a dynamic and realistic galactic potential. Unfortunately, neither larger-box, global galaxy simulations nor cosmological zoom-in simulations are run at high enough resolution to capture inflow at the disk-halo interface on the scales we are probing. Nonetheless, recent results from zoom-in simulations do show that the circumgalactic medium contains contributions from both outflows and inflows, and that low-velocity material makes up a significant fraction of the mass of these gas flows (e.g. Zheng et al., 2015; Muratov et al., 2017; Zheng et al., 2020).

While the multiphase nature of the CGM and disk-halo interface is well-characterized, our understanding of the physical origin of the phases and their interrelation remains unresolved. The literature is dense with examples of processes of varying levels of complexity that can create and maintain a multiphase, ionized medium: CIE and non-CIE static radiative cooling models (Edgar & Chevalier, 1986; Gnat & Sternberg, 2007); radiative cooling models that include gas dynamics (Shapiro & Benjamin, 1991; Wakker et al., 2012); shock ionization models (Dopita & Sutherland, 1996); conductive interfaces between cool clouds and a hot

medium Borkowski et al. (1990); and non-equilibrium turbulent mixing layer models (Begelman & Fabian, 1990; Slavin et al., 1993; Kwak & Shelton, 2010). The gas kinematics of both the low and high-ions are an important observational constraint on each of these models. Specifically, quantifying the degree to which different phases are co-moving can reveal or rule out certain physical origins.

The differential accretion velocities at the disk halo interface exhibited by low and high ions cannot be explained by a single-phase medium in photoionization equilibrium. This conclusion is not particularly strong, but it is worth noting because most photoionization modeling of the CGM assumes full thermal photoionization equilibrium in which photoheating balances line cooling (Werk et al., 2014). Specifically, our finding indicates that low- and high-ions (e.g., S II and C IV) trace gas of either different temperatures or densities, or perhaps both. Analogously, absorption-line work in the more extended CGM often finds misalignment of the high and low-ion absorption profiles in velocity space (e.g. Tripp et al., 2008; Fox et al., 2013). None of the aforementioned models naturally captures velocity offsets between low and high ions better than the shock ionization models, which generally consider collisionally-ionized gas behind a high speed radiative shock (e.g. Dopita & Sutherland, 1996; Allen et al., 2008; Gnat & Sternberg, 2009). The model presented by Melso et al. (2019), discussed earlier, provides a detailed explanation of how shocks might fit into the context of the disk-halo interface.

Conductive Interface and Turbulent Mixing Layer (TML) models, often invoked in the context of HVCs and IVCs, are also worth considering, although gas velocities are not part of the predictions of these ionization models. Nonetheless, they put forward a physical picture that links multiple phases and is often the best explanation of the column density ratios of the different ionization states (e.g. Sembach et al., 2003; Fox et al., 2004; Lehner et al., 2011; Wakker et al., 2012; Savage et al., 2014). In the TML model, cool ($\sim 10^4$ K) clouds moving through a hot ($\sim 10^6$ K) medium possess a shell of gas at their boundary in which Kelvin-Helmholtz instabilities are mixing the hot and cool gas. Turbulence-driven mixing produces gas in the layer with an intermediate temperature, characterized by highly ionized species.

A cool cloud moving through a hot medium can also produce a surface layer in which cool gas is evaporating and hot gas is condensing because electron collisions are conducting heat between the two media (Borkowski et al., 1990; Gnat et al., 2010). Referred to as conductive interfaces, these models predict how the column densities of transition temperature ions change as a function of time and the angle between the magnetic field and the conduction layer orientation. While the amount of turbulence and strength of magnetic fields are difficult to observationally constrain at the disk-halo interface, it is likely they are playing some role in determining the multiphase structure of the gas in this region.

Perhaps the most puzzling aspects of our data are the differences in gas infall velocities for lines of sight toward/away from rotation and toward/away from Galactic center in the North. In particular, gas velocities along lines of sight looking away from Galactic rotation (labeled antirotation in Figure 4.5.2) seem to coincide with HI velocities in all phases, at $v_{LSR} \approx 0$. Similarly, the trends of infall velocity with ionization potential energy are not readily apparent unless you are looking toward or away from Galactic center. A radial inflow of ionized gas toward Galactic center could partially explain this result (Joung et al., 2012a). However, this scenario does not easily explain why the velocities for both warm and cool ions are higher toward rotation than antirotation. The most likely explanation is that differential accretion, and possibly accretion in general, is a local rather than a global process, so we do not necessarily expect to see uniform accretion in all directions. Furthermore, there are likely multiple modes of accretion and outflow happening simultaneously in this dynamic region referred to as the disk-halo interface.

4.7 Conclusions

In this work we have performed an analysis of low-velocity ($|v| < 150 \mathrm{km\,s^{-1}}$) gas flowing in and out of the Milky Way at the disk-halo interface. We measure Ni II, S II, C II*, Si IV, C IV, and N V absorption features along 147 quasar sightlines across the full sky, as well as HI and Hα in emission along those same sightlines, to examine the kinematics of gas at a

range of temperatures ($10^4 \lesssim T \lesssim 10.5$K). These data allow us to contrast the dynamics of accreting and outflowing extraplanar gas in cool, warm, and warm-hot phases to shed light on our currently murky understanding of the mechanisms driving baryon cycling in galaxies. Our main results are as follows:

1. Overall, we detect low-velocity gas at rates of 93% for H I, 100% for Hα, 63% for Ni II, 65% for S II, 63% for C II*, 85% for Si IV, 89% for C IV, and 52% for N V, with median column density-weighted velocities of -2.9, -3.1, -15.1, -14.8, -12.9, -25.7, -25.8, and -26.1 km s^{-1}, respectively. (§4.4 and §4.4.1; Figures 4.3.2, 4.3.3, and 4.3.4; Table 4.1)

2. Although the bulk of the gas is predominantly inflowing, inflowing and outflowing components are detected together along a single sightline in 2-67% of sightlines, depending on the ion, indicating that inflows and outflows may be occurring simultaneously in close proximity to one another. (§4.6; Figure 4.3.2; Table 4.1)

3. In the Northern Galactic hemisphere, 'low ions' (Ni II, S II, and C II*) are inflowing at median velocities approximately 10 km s^{-1} faster than hydrogen, and 'high ions' (Si IV, C IV, and N V) are inflowing at median velocities approximately 20-25 km s^{-1} faster than hydrogen. This differential infall is not found in the South, a finding in line with with the Milky Way's well-documented dearth of inflowing material in the South. Differential infall may be evidence of warm accreting gas cooling as it reaches the disk-halo interface, causing a pileup of cool gas. We note that this differential infall is only found in sightlines toward and away from Galactic center in the North. In the directions toward and away from the direction of Galactic rotation, gas absorption is kinematically aligned at all temperatures. We speculate that this is either evidence of radially-oriented inflows or simply a result of spatially patchy accretion. (§4.4.1, §4.6; Figures 4.3.4, 4.5.1, and 4.5.2; Table 4.1)

4. We develop a kinematic model of rotating disk-halo interface gas and compare its predictions to our measured velocities, assuming three different density distributions for the gas. We find that no particular density distribution fits the data better than the others. The best-fit parameters of the models predict a vertical lag of $v \sim 10$km/s/kpc, rotational velocities ranging from 215-240 $\mathrm{km\,s^{-1}}$ with smaller velocities for higher ions, infall velocities of $\sim -10\mathrm{km\,s^{-1}}$, and scale heights of 50-400 pc. The model consistently predicts scale heights significantly smaller than what is reported in the literature, and does not recover the differential infall we observe. We discuss potential issues with such models and conclude that the modeling results have limited utility in this context. (§4.5; Figure 4.5.3)

5. We calculate accretion/outflow timescales and mass flow rates. As expected given the North-South asymmetry, we find that accretion rates are higher in the North. In general the detection rate of inflows is higher than that of outflows, and the inflow rate is a factor of ∼10 greater than the outflow rate. For low ions, we find timescales ranging from $t_{in} = 20 - 30$ Myr and $t_{out} = 26 - 52$ Myr in the North, and $t_{in} = 58 - 77$ Myr and $t_{out} = 34 - 92$ Myr in the South. For high ions, we find timescales ranging from $t_{in} = 77 - 109$ Myr and $t_{out} = 71 - 431$ Myr in the North, and $t_{in} = 67 - 193$ Myr and $t_{out} = 76 - 239$ Myr in the South. For low ions, we find accretion rates ranging from $\dot{M}_{in} = 1.8 - 96.3 \times 10^{-6}$ $M_\odot$/yr and $\dot{M}_{out} = 0.3 - 5.6 \times 10^{-6}$ $M_\odot$/yr in the North, and $\dot{M}_{in} = 0.4 - 20.7 \times 10^{-6}$ $M_\odot$/yr and $\dot{M}_{out} = 0.1 - 4.9 \times 10^{-6}$ $M_\odot$/yr in the South. For high ions, we find accretion rates ranging from $\dot{M}_{in} = 3.4 - 20.7 \times 10^{-6}$ $M_\odot$/yr and $\dot{M}_{out} = 0.01 - 2.6 \times 10^{-6}$ $M_\odot$/yr in the North, and $M_{in} = 0.7 - 15.1 \times 10^{-6}$ $M_\odot$/yr and $\dot{M}_{out} = 0.2 - 5.6 \times 10^{-6}$ $M_\odot$/yr in the South. (§4.4.2; Table 4.1)

6. Higher-resolution simulations of the disk-halo interface will be an instrumental part of bringing into focus the big picture that these data are pointing to. In particular, predictions from simulations regarding the kinematics of low versus high ions will be helpful for constraining the mechanisms driving this phenomenon. (§4.6)

Chapter 5

SUMMARY

Much of the material that forms stars in galaxies was once in the circumgalactic medium – the massive, diffuse halo of gas extending out to the virial radius of galaxies and beyond. Recent advances in high-resolution spectroscopy have enabled observers to firmly establish the key role played by the CGM in the life cycle of galaxies: it is the hiding place of approximately half of all galactic baryons, acting as a massive reservoir that regulates the supply of fuel for star formation (Peeples et al., 2014; Werk et al., 2014; Tumlinson et al., 2017). Gas from stellar winds, supernovae, and the Milky Way's central black hole eject material into the CGM where it cools and re-accretes, being continuously recycled in the so-called galactic fountain. Gas flowing in and out of galaxies through the CGM is closely tied to the star-formation in those galaxies, and thus our understanding of CGM gas flows is a critical piece in the larger puzzle of galaxy evolution.

To this end, the research presented in this dissertation has made use of high-resolution spectroscopy to characterize, map and model gas flows in the Milky Way's halo. In most cases, such diffuse gas can only be be detected in absorption along lines of sight to bright background sources like quasars or halo stars. The Milky Way is our best laboratory for measuring the CGM because of the abundance of such sightlines available, and because of the proximity of the gas to us. I have therefore focused my efforts on measurements of gas within the Milky Way.

In chapter 2, I made densely-sampled observations of cool gas at the Milky Way's local disk-halo interface, using halo stars at varying distances, to obtain a 3-dimensional picture of the spatial and kinematic properties of the gas. These cooler ions behave much like HI observed in emission, and sit close to the disk in clouds with a characteristic size of $<$500 pc. At the local disk-halo interface, the gas is almost exclusively inflowing and exhibits a velocity gradient across the disk that is consistent with the galactic fountain model. The ion covering fractions support a multi-phase picture in which small clumps or droplets of cool gas are suspended within larger clouds or streams of hotter, more diffuse gas.

In chapter 3, I employed a novel spectroscopic differencing technique to make the first isolated measurements of the extended low-velocity Galactic CGM. Using paired star-quasar

sightlines across the sky, I measured the foreground gas absorption in the stellar spectra, and subtracted that foreground signal from absorption features in the paired quasar spectra to measure the absorption originating from gas beyond the halo star. The median covering fraction of warm low-velocity gas in the Milky Way's CGM is below the detection limit, and markedly lower than in simulations and observations of other L* galaxies. Although it is possible the Milky Way represents an anomaly among star-forming galaxies, the differing geometric viewing effects of the Milky Way and external galaxies also allow for the possibility that the warm, low-velocity CGM of L* galaxies exhibits a flared-disk morphology.

In chapter 4, I built upon the results of chapter 3 to further investigate low-velocity gas flows and the morphology of the Milky Way's warm CGM. Given that my earlier results rule out a spherical morphology, I developed kinematic models to test various other morphologies. I ultimately found that these models are too simple to account for the complex distribution and kinematics of accreting gas, and that to constrain gas so close to the disk would require additional sightlines at low Galactic latitude, where extinction is high and quasar sightlines are scarce. In this work, I also measured low-velocity gas absorption tracing a wide range of temperatures and discovered that the accretion velocities of these ions differ as a function of ionization energy, with higher ions accreting at faster velocities. This result likely has implications for how gas is transferred from the CGM to the disk, suggesting that accreting material cools as it approaches the disk-halo interface, causing a pileup of cooler gas that accretes more slowly. The mass accretion rate of these inflows is roughly comparable to that of HVCs, indicating that a significant fraction of star-formation fuel may be accreted onto the disk at low velocities.

By placing new constraints on the kinematics, ionization state, and morphology of CGM gas flows in the Milky Way, my dissertation research has contributed to our progress in developing a complete understanding of the CGM and galaxy evolution. However, more high-resolution observations and simulations are still needed to test competing theories and propel the science forward.

BIBLIOGRAPHY

Albert, C. E., & Danly, L. 2004, in Astrophysics and Space Science Library, Vol. 312, High Velocity Clouds, ed. H. van Woerden, B. P. Wakker, U. J. Schwarz, & K. S. de Boer, 73

Allen, M. G., Groves, B. A., Dopita, M. A., Sutherland, R. S., & Kewley, L. J. 2008, ApJS, 178, 20

André, M. K., Le Petit, F., Sonnentrucker, P., et al. 2004, A&A, 422, 483

Armillotta, L., Fraternali, F., & Marinacci, F. 2016, MNRAS, 462, 4157

Armillotta, L., Fraternali, F., Werk, J. K., Prochaska, J. X., & Marinacci, F. 2017, MNRAS, 470, 114

Asplund, M., Grevesse, N., Sauval, A. J., & Scott, P. 2009, Annual Review of Astronomy and Astrophysics, 47, 481

Bahcall, J. N., & Spitzer, Jr., L. 1969, ApJ, 156, L63

Begelman, M. C., & Fabian, A. C. 1990, MNRAS, 244, 26P

Bell, E. F., Papovich, C., Wolf, C., et al. 2005, ApJ, 625, 23

Ben Bekhti, N., Richter, P., & Westmeier, T. 2007, in EAS Publications Series, Vol. 24, EAS Publications Series, ed. E. Emsellem, H. Wozniak, G. Massacrier, J. F. Gonzalez, J. Devriendt, & N. Champavert, 281–282

Ben Bekhti, N., Richter, P., Winkel, B., Kenn, F., & Westmeier, T. 2009, \aap, 503, 483

Ben Bekhti, N., Winkel, B., Richter, P., et al. 2012, A&A, 542, A110

Benjamin, R. A., & Danly, L. 1997, ApJ, 481, 764

Bergeron, J. 1986, A&A, 155, L8

Bianchi, L., Shiao, B., & Thilker, D. 2017, \apjs, 230, 24

Binney, J., Nipoti, C., & Fraternali, F. 2009, MNRAS, 397, 1804

Bish, H., Werk, J., Prochaska, J., et al. 2019, Astrophysical Journal, 882, doi:10.3847/1538-4357/ab3414

Bish, H. V., Werk, J. K., Peek, J., Zheng, Y., & Putman, M. 2021, \apj, 912, 8

Bland-Hawthorn, J., & Gerhard, O. 2016, ARA&A, 54, 529

Boettcher, E., Gallagher, III, J. S., & Zweibel, E. G. 2017, ApJ, 845, 155

Boomsma, R., Oosterloo, T. A., Fraternali, F., van der Hulst, J. M., & Sancisi, R. 2008, A&A, 490, 555

Bordoloi, R., Lilly, S. J., Kacprzak, G. G., & Churchill, C. W. 2014a, ApJ, 784, 108

Bordoloi, R., Lilly, S., Knobel, C., et al. 2011, ApJ, 743, 10

Bordoloi, R., Tumlinson, J., Werk, J. K., et al. 2014b, The Astrophysical Journal, 796, 136

Bordoloi, R., Lilly, S., Hardmeier, E., et al. 2014c, ApJ, 794, 130

Bordoloi, R., Fox, A. J., Lockman, F. J., et al. 2017, ApJ, 834, 191

Borkowski, K. J., Balbus, S. A., & Fristrom, C. C. 1990, ApJ, 355, 501

Borthakur, S., Heckman, T., Tumlinson, J., et al. 2015, ApJ, 813, 46

Bouché, N., Murphy, M., Kacprzak, G., et al. 2013, Science, 341, 50

Bowen, D. V., Jenkins, E. B., Tripp, T. M., et al. 2008, ApJS, 176, 59

Bregman, J. N. 1980, ApJ, 236, 577

Bregman, J. N., Anderson, M. E., Miller, M. J., et al. 2018, ApJ, 862, 3

Briggs, F. H. 1990, ApJ, 352, 15

Brooks, A. M., Governato, F., Quinn, T., Brook, C. B., & Wadsley, J. 2009, ApJ, 694, 396

Burchett, J. N., Tripp, T. M., Wang, Q. D., et al. 2018, MNRAS, 475, 2067

Burchett, J. N., Tripp, T. M., Prochaska, J. X., et al. 2015, \apj, 815, 91

Burchett, J. N., Tripp, T. M., Bordoloi, R., et al. 2016, The Astrophysical Journal, 832, 124

Carnall, A. 2017, arXiv e-prints, arXiv:1705.05165

Cautun, M., Deason, A. J., Frenk, C. S., & McAlpine, S. 2019, MNRAS, 483, 2185

Chen, H.-W., Lanzetta, K. M., Webb, J. K., & Barcons, X. 1998, The Astrophysical Journal, 498, 77

Chen, Y.-M., Tremonti, C. A., Heckman, T. M., et al. 2010, AJ, 140, 445

Chomiuk, L., & Povich, M. S. 2011, AJ, 142, 197

Clark, S., Bordoloi, R., & Fox, A. J. 2022, MNRAS, 512, 811

Clewley, L., & Jarvis, M. J. 2006, Monthly Notices of the Royal Astronomical Society, 368, 310

Coc, A. 2016, Journal of Physics: Conference Series, 665, 12001

Collins, J., Shull, J., & Giroux, M. 2009, ApJ, 705, 962

Cornuault, N., Lehnert, M. D., Boulanger, F., & Guillard, P. 2018, A&A, 610, A75

Creasey, P., Theuns, T., & Bower, R. G. 2013, MNRAS, 429, 1922

Crighton, N. H. M., Hennawi, J. F., Simcoe, R. A., et al. 2015, MNRAS, 446, 18

Danforth, C. W., Keeney, B. A., Tilton, E. M., et al. 2016, The Astrophysical Journal, 817, arXiv:1402.2655

Danly, L. 1986, in Interstellar Processes: Abstracts of Contributed Papers, ed. D. J. Hollenbach & J. Thronson, H. A., 95–96

de Avillez, M. A. 2000, Ap&SS, 272, 23

Deason, A. J., Belokurov, V., & Evans, N. W. 2011, MNRAS, 416, 2903

Dehnen, W., McLaughlin, D. E., & Sachania, J. 2006, Monthly Notices of the Royal Astronomical Society, 369, 1688

Dickey, J. M., & Lockman, F. J. 1990, ARA&A, 28, 215

Dobler, G., Finkbeiner, D. P., Cholis, I., Slatyer, T., & Weiner, N. 2010, \apj, 717, 825

Dopita, M. A., & Sutherland, R. S. 1996, ApJS, 102, 161

Edgar, R. J., & Chevalier, R. A. 1986, ApJ, 310, L27

Emerick, A., Bryan, G. L., Mac Low, M.-M., et al. 2018, ApJ, 869, 94

Erb, D. K. 2008, ApJ, 674, 151

Ferland, G. J., Chatzikos, M., Guzmán, F., et al. 2017, Revista Mexicana de Astronomia y Astrofisica, 53, 385

Fielding, D., Quataert, E., McCourt, M., & Thompson, T. A. 2017, MNRAS, 466, 3810

Forbes, J. C., & Lin, D. N. C. 2018, arXiv e-prints, arXiv:1810.12925

Ford, H. A., Lockman, F. J., & McClure-Griffiths, N. M. 2010, ApJ, 722, 367

Ford, H. A., McClure-Griffiths, N., Lockman, F. J., et al. 2008, ApJ, 688, 290

Foreman-Mackey, D., Hogg, D. W., Lang, D., & Goodman, J. 2013, Publications of the Astronomical Society of the Pacific, 125, 306

Fox, A. J., Richter, P., Ashley, T., et al. 2019, ApJ, 884, 53

Fox, A. J., Savage, B. D., & Wakker, B. P. 2006, ApJS, 165, 229

Fox, A. J., Savage, B. D., Wakker, B. P., et al. 2004, ApJ, 602, 738

Fox, A. J., Lehner, N., Tumlinson, J., et al. 2013, ApJ, 778, 187

Fox, A. J., Wakker, B. P., Barger, K. A., et al. 2014, ApJ, 787, 147

Fox, A. J., Lehner, N., Lockman, F. J., et al. 2015a, ApJ, 816, L11

Fox, A. J., Bordoloi, R., Savage, B. D., et al. 2015b, ApJ, 799, L7

Fraternali, F. 2017, in Astrophysics and Space Science Library, Vol. 430, Gas Accretion onto Galaxies (Springer International Publishing), 323–353

Fraternali, F., & Binney, J. J. 2006, MNRAS, 366, 449

—. 2008, MNRAS, 386, 935

Fraternali, F., Oosterloo, T., Sancisi, R., & van Moorsel, G. 2001, ApJ, 562, L47

Fraternali, F., van Moorsel, G., Sancisi, R., & Oosterloo, T. 2002, AJ, 123, 3124

Froning, C. S., & Green, J. C. 2009, Ap&SS, 320, 181

Fukui, Y., Koga, M., Maruyama, S., et al. 2018, Publications of the ASJ, 132

Gaensler, B., Madsen, G., Chatterjee, S., & Mao, S. 2008, \pasa, 25, 184

Gaia Collaboration, Prusti, T., de Bruijne, J., et al. 2016, \aap, 595, A1

Gaia Collaboration, Brown, A., Vallenari, A., et al. 2018, \aap, 616, A1

García-Ruiz, I., Sancisi, R., & Kuijken, K. 2002, Astronomy & Astrophysics, 394, 769

Geha, M., Wechsler, R. H., Mao, Y.-Y., et al. 2017, ApJ, 847, 4

Ghavamian, P., Aloisi, A., Lennon, D., et al. 2009, Preliminary Characterization of the Post-Launch Line Spread Function of COS, Tech. rep., Space Telescope Science Institute

Gnat, O., & Sternberg, A. 2007, ApJS, 168, 213

—. 2009, ApJ, 693, 1514

Gnat, O., Sternberg, A., & McKee, C. F. 2010, ApJ, 718, 1315

Grcevich, J., & Putman, M. E. 2009, ApJ, 696, 385

Green, J. C., Froning, C. S., Osterman, S., et al. 2012, ApJ, 744, 60

Gronke, M., & Oh, S. P. 2020, MNRAS, 492, 1970

Gronke, M., & Peng Oh, S. 2018, Monthly Notices of the Royal Astronomical Society: Letters, 480, arXiv:1806.02728

Haffner, L. M., Reynolds, R. J., Tufte, S. L., et al. 2003, ApJS, 149, 405

Haffner, L. M., Reynolds, R. J., Madsen, G. J., et al. 2010, in Astronomical Society of the Pacific Conference Series, Vol. 438, The Dynamic Interstellar Medium: A Celebration of the Canadian Galactic Plane Survey, ed. R. Kothes, T. L. Landecker, & A. G. Willis, 388

Heald, G., Józsa, G., Serra, P., et al. 2011, A&A, 526, A118

Heckman, T., Borthakur, S., Wild, V., Schiminovich, D., & Bordoloi, R. 2017, ApJ, 846, 151

Heckman, T. M., Alexandroff, R. M., Borthakur, S., Overzier, R., & Leitherer, C. 2015, ApJ, 809, 147

Heckman, T. M., Lehnert, M. D., Strickland, D. K., & Armus, L. 2000, ApJS, 129, 493

Heitsch, F., & Putman, M. E. 2009, ApJ, 698, 1485

Helmi, A., Navarro, J. F., Meza, A., Steinmetz, M., & Eke, V. R. 2003, ApJ, 592, L25

Hernquist, L., & Quinn, P. J. 1988, ApJ, 331, 682

HI4PI Collaboration, Ben Bekhti, N., Flöer, L., et al. 2016, \aap, 594, A116

Hill, A. S., Joung, M. R., Mac Low, M.-M., et al. 2012, ApJ, 750, 104

Ho, S. H., Martin, C. L., Kacprzak, G. G., & Churchill, C. W. 2017, ApJ, 835, 267

Hodges-Kluck, E. J., Miller, M. J., & Bregman, J. N. 2016, ApJ, 822, 21

Hogg, D. W., Eilers, A.-C., & Rix, H.-W. 2019, AJ, 158, 147

Hopkins, A., McClure-Griffiths, N., & Gaensler, B. 2008, ApJ, 682, L13

Houck, J. C., & Bregman, J. N. 1990, ApJ, 352, 506

Howk, J. C., Rueff, K. M., Lehner, N., et al. 2018, ApJ, 856, 166

Howk, J. C., Savage, B. D., Sembach, K. R., & Hoopes, C. G. 2002, \apj, 572, 264

Hsu, W. H., Putman, M. E., Heitsch, F., et al. 2011, AJ, 141, 57

Hummels, C. B., Smith, B. D., Hopkins, P. F., et al. 2018, arXiv e-prints, arXiv:1811.12410

James, P. A., & Ivory, C. F. 2011, MNRAS, 411, 495

Johnson, S. D., Chen, H.-W., Mulchaey, J. S., Schaye, J., & Straka, L. A. 2017, ApJ, 850, L10

Joung, M. R., Bryan, G. L., & Putman, M. E. 2012a, ApJ, 745, 148

Joung, M. R., & Mac Low, M.-M. 2006, ApJ, 653, 1266

Joung, M. R., Putman, M. E., Bryan, G. L., Fernández, X., & Peek, J. E. G. 2012b, ApJ, 759, 137

Kacprzak, G. G., Churchill, C. W., Steidel, C. C., Spitler, L. R., & Holtzman, J. A. 2012, MNRAS, 427, 3029

Kalberla, P. M. W., Burton, W. B., Hartmann, D., et al. 2005, A&A, 440, 775

Kalberla, P. M. W., & Haud, U. 2015, A&A, 578, A78

Karim, M. T., Fox, A. J., Jenkins, E. B., et al. 2018, ApJ, 860, 98

Katz, D., Antoja, T., Romero-Gómez, M., et al. 2018, Astronomy & Astrophysics, 616, A11

Kaufmann, T., Mayer, L., Wadsley, J., Stadel, J., & Moore, B. 2006, MNRAS, 370, 1612

Keeney, B. A., Stocke, J. T., Rosenberg, J. L., et al. 2013, ApJ, 765, 27

Kennicutt, R. C., & Evans, N. J. 2012, Annual Review of Astronomy and Astrophysics, 50, 531

Kerscher, M., Szapudi, I., & Szalay, A. S. 2000, ApJ, 535, L13

Kim, C.-G., & Ostriker, E. C. 2017, \apj, 846, 133

Kim, C.-G., & Ostriker, E. C. 2018, ApJ, 853, 173

Kinman, T. D., Suntzeff, N. B., & Kraft, R. P. 1994, AJ, 108, 1722

Kirby, E. N. 2011, in EAS Publications Series, Vol. 48, EAS Publications Series, ed. M. Koleva, P. Prugniel, & I. Vauglin, 19–25

Krumholz, M. R., & Ting, Y.-S. 2018, MNRAS, 475, 2236

Kuntz, K. D., & Danly, L. 1993, in Star Formation, Galaxies and the Interstellar Medium, ed. J. Franco, F. Ferrini, & G. Tenorio-Tagle, 99–104

Kuntz, K. D., & Danly, L. 1996, ApJ, 457, 703

Kwak, K., Henley, D. B., & Shelton, R. L. 2011, ApJ, 739, 30

Kwak, K., & Shelton, R. L. 2010, ApJ, 719, 523

Kwak, K., Shelton, R. L., & Henley, D. B. 2015, ApJ, 812, 111

Lancaster, L., Koposov, S. E., Belokurov, V., Evans, N. W., & Deason, A. J. 2018, arXiv e-prints, arXiv:1807.04290

Landy, S., & Szalay, A. 1993, ApJ, 412, 64

Lanzetta, K. M., Bowen, D. V., Tytler, D., & Webb, J. K. 1995, ApJ, 442, 538

Lehner, N., Howk, J., Marasco, A., & Fraternali, F. 2022, arXiv e-prints, arXiv:2202.05848

Lehner, N., & Howk, J. C. 2010, ApJ, 709, L138

Lehner, N., & Howk, J. C. 2011, Science, 334, 955

Lehner, N., Howk, J. C., Thom, C., et al. 2012, MNRAS, 424, 2896

Lehner, N., Howk, J. C., & Wakker, B. P. 2015, ApJ, 804, 79

Lehner, N., Zech, W. F., Howk, J. C., & Savage, B. D. 2011, ApJ, 727, 46

Lehner, N., Berek, S. C., Howk, J. C., et al. 2020, arXiv e-prints, arXiv:2002.07818

Leroy, A. K., Walter, F., Sandstrom, K., et al. 2013, AJ, 146, 19

Levine, E., Blitz, L., & Heiles, C. 2006, ApJ, 643, 881

Li, F., Rahman, M., Murray, N., et al. 2021, MNRAS, 500, 1038

Li, M., Bryan, G. L., & Ostriker, J. P. 2017, ApJ, 841, 101

Li, M., & Tonnesen, S. 2020, ApJ, 898, 148

Liang, C. J., & Chen, H.-W. 2014, MNRAS, 445, 2061

Liang, C. J., & Remming, I. S. 2018, arXiv e-prints, arXiv:1806.10688

Licquia, T. C. 2016, PhD thesis, University of Pittsburgh

Licquia, T. C., Newman, J. A., & Brinchmann, J. 2015, ApJ, 809, 96

Liu, L., Gerke, B. F., Wechsler, R. H., Behroozi, P. S., & Busha, M. T. 2011, ApJ, 733, 62

Lochhaas, C., Bryan, G. L., Li, Y., Li, M., & Fielding, D. 2020, MNRAS, 493, 1461

Lockman, F. J., Murphy, E. M., Petty-Powell, S., & Urick, V. J. 2002, ApJS, 140, 331

Luri, X., Brown, A. G. A., Sarro, L. M., et al. 2018, A&A, 616, A9

Maio, U., Dolag, K., Ciardi, B., & Tornatore, L. 2007, Monthly Notices of the Royal Astronomical Society, 379, 963

Maller, A. H., & Bullock, J. S. 2004, Monthly Notices of the Royal Astronomical Society, 355, 694

Mao, Y.-Y., Geha, M., Wechsler, R. H., et al. 2021, ApJ, 907, 85

Marasco, A., & Fraternali, F. 2011, A&A, 525, A134

Marasco, A., & Fraternali, F. 2011, Astronomy & Astrophysics, 525, A134

Marasco, A., Fraternali, F., & Binney, J. J. 2012, Monthly Notices of the Royal Astronomical Society, 419, 1107

Marasco, A., Marinacci, F., & Fraternali, F. 2013, Monthly Notices of the Royal Astronomical Society, 433, 1634

Marinacci, F., Binney, J., Fraternali, F., et al. 2010, MNRAS, 404, 1464

Marinacci, F., Fraternali, F., Binney, J., et al. 2012, in European Physical Journal Web of Conferences, Vol. 19, European Physical Journal Web of Conferences, 08008

Marinacci, F., Fraternali, F., Nipoti, C., et al. 2011, MNRAS, 415, 1534

Martin, C. L. 2005, ApJ, 621, 227

Martin, C. L., Ho, S. H., Kacprzak, G. G., & Churchill, C. W. 2019, ApJ, 878, 84

McCourt, M., Oh, S. P., O'Leary, R., & Madigan, A.-M. 2018, Monthly Notices of the Royal Astronomical Society, 473, 5407

McCourt, M., O'Leary, R. M., Madigan, A.-M., & Quataert, E. 2015, MNRAS, 449, 2

McCourt, M., Sharma, P., Quataert, E., & Parrish, I. J. 2012, MNRAS, 419, 3319

McQuinn, M., & Werk, J. K. 2018, ApJ, 852, 33

Melso, N., Bryan, G. L., & Li, M. 2019, The Astrophysical Journal, 872, 47

Miller, M. J., & Bregman, J. N. 2013, ApJ, 770, 118

Miller, M. J., & Bregman, J. N. 2015, ApJ, 800, 14

Millman, K. J., & Aivazis, M. 2011, Computing in Science & Engineering, 13, 9

Moisés, A., Damineli, A., Figuerêdo, E., et al. 2011, MNRAS, 411, 705

Muller, C. A., Oort, J. H., & Raimond, E. 1963, Academie des Sciences Paris Comptes Rendus, 257, 1661

Münch, G. 1957, The Astrophysical Journal, 125, 42

Münch, G., & Zirin, H. 1961, ApJ, 133, 11

Muratov, A. L., Kereš, D., Faucher-Giguère, C.-A., et al. 2017, MNRAS, 468, 4170

Murga, M., Zhu, G., Ménard, B., & Lan, T.-W. 2015, MNRAS, 452, 511

Murphy, E., Lockman, F., & Savage, B. 1995, ApJ, 447, 642

Mutch, S. J., Croton, D. J., & Poole, G. B. 2011, ApJ, 736, 84

Myeong, G. C., Evans, N. W., Belokurov, V., Amorisco, N. C., & Koposov, S. E. 2018, Monthly Notices of the Royal Astronomical Society, 475, 1537

Nakanishi, H., & Sofue, Y. 2003, PASJ, 55, 191

Nasoudi-Shoar, S., Richter, P., de Boer, K. S., & Wakker, B. P. 2010, A&A, 520, A26

Newberg, H. J., Yanny, B., Rockosi, C., et al. 2002, ApJ, 569, 245

Nidever, D. L., Majewski, S. R., & Burton, W. B. 2008, Astrophysics and Space Science Proceedings, 5, 243

Norman, C. A., & Ikeuchi, S. 1989, ApJ, 345, 372

O'Meara, J. M., Lehner, N., Howk, J. C., et al. 2015, AJ, 150, 111

Oosterloo, T., Fraternali, F., & Sancisi, R. 2007a, AJ, 134, 1019

Oosterloo, T. A., Morganti, R., Sadler, E. M., van der Hulst, T., & Serra, P. 2007b, A&A, 465, 787

Oppenheimer, B. D. 2018, MNRAS, 480, 2963

Oppenheimer, B. D., & Davé, R. 2008, Monthly Notices of the Royal Astronomical Society, 387, 577

Oppenheimer, B. D., Schaye, J., Crain, R. A., Werk, J. K., & Richings, A. J. 2018a, MNRAS, 481, 835

Oppenheimer, B. D., Segers, M., Schaye, J., Richings, A. J., & Crain, R. A. 2018b, MNRAS, 474, 4740

Oppenheimer, B. D., Crain, R. A., Schaye, J., et al. 2016, MNRAS, 460, 2157

Oppenheimer, B. D., Davies, J. J., Crain, R. A., et al. 2020, MNRAS, 491, 2939

Osterman, S., Green, J., Froning, C., et al. 2010, in American Astronomical Society Meeting Abstracts, Vol. 215, American Astronomical Society Meeting Abstracts #215, 464.22

Pacifici, C., Kassin, S. A., Weiner, B. J., et al. 2016, ApJ, 832, 79

Peek, J., Putman, M., McKee, C. F., Heiles, C., & Stanimirović, S. 2007, ApJ, 656, 907

Peek, J., Heiles, C., Douglas, K. A., et al. 2011, ApJS, 194, 20

Peek, J. E., Heiles, C., Putman, M. E., & Douglas, K. 2009, Astrophysical Journal, 692, 827

Peek, J. E. G., Putman, M. E., & Sommer-Larsen, J. 2008, ApJ, 674, 227

Peeples, M., Tumlinson, J., Fox, A., et al. 2017, The Hubble Spectroscopic Legacy Archive, Instrument Science Report COS 2017-4

Peeples, M. S., Werk, J. K., Tumlinson, J., et al. 2014, ApJ, 786, 54

Peeples, M. S., Corlies, L., Tumlinson, J., et al. 2019, ApJ, 873, 129

Planck Collaboration, Ade, P., Aghanim, N., et al. 2014, \aap, 571, A16

Poggio, E., Drimmel, R., Lattanzi, M. G., et al. 2018, MNRAS, 5, 1

Pointon, S. K., Nielsen, N. M., Kacprzak, G. G., et al. 2017, ApJ, 844, 23

Posti, L., & Helmi, A. 2019, \aap, 621, A56

Prochaska, J. X., Weiner, B., Chen, H. W., Cooksey, K. L., & Mulchaey, J. S. 2011, ApJS, 193, 28

Prochaska, J. X., Werk, J. K., Worseck, G., et al. 2017, ApJ, 837, 169

Puspitarini, L., & Lallement, R. 2012, A&A, 545, A21

Putman, M., Peek, J., & Joung, M. 2012, Annual Review of Astronomy and Astrophysics, 50, 491

Putman, M., Henning, P., Bolatto, A., et al. 2009, in astro2010: The Astronomy and Astrophysics Decadal Survey, Vol. 2010, 241

Putman, M. E., Peek, J. E. G., & Heitsch, F. 2012, in EAS Publications Series, Vol. 56, EAS Publications Series, ed. M. A. de Avillez, 267–274

Putman, M. E., de Heij, V., Staveley-Smith, L., et al. 2002, AJ, 123, 873

Qu, Z., & Bregman, J. N. 2019, ApJ, 880, arXiv:1906.12259

Qu, Z., Bregman, J. N., Hodges-Kluck, E., Li, J.-T., & Lindley, R. 2020, ApJ, 894, 142

Rahmani, H., Péroux, C., Augustin, R., et al. 2018, Monthly Notices of the Royal Astronomical Society, 474, 254

Reynolds, R. 1993, in American Institute of Physics Conference Series, Vol. 278, Back to the Galaxy, ed. S. S. Holt & F. Verter, 156–165

Reynolds, R. J. 2004, Advances in Space Research, 34, 27

Ribaudo, J., Lehner, N., Howk, J. C., et al. 2011, ApJ, 743, 207

Richter, P. 2017, in Astrophysics and Space Science Library, Vol. 430, Gas Accretion onto Galaxies, ed. A. Fox & R. Davé, 15

Richter, P., Savage, B. D., Wakker, B. P., Sembach, K. R., & Kalberla, P. M. W. 2001a, ApJ, 549, 281

Richter, P., Sembach, K. R., Wakker, B. P., et al. 2001b, ApJ, 559, 318

Rubin, K. H. R., Diamond-Stanic, A. M., Coil, A. L., Crighton, N. H. M., & Stewart, K. R. 2018a, Astrophysical Journal, arXiv:1806.08801

Rubin, K. H. R., Prochaska, J. X., Koo, D. C., & Phillips, A. C. 2012, ApJ, 747, L26

Rubin, K. H. R., Prochaska, J. X., Koo, D. C., et al. 2014, ApJ, 794, 156

Rubin, K. H. R., O'Meara, J. M., Cooksey, K. L., et al. 2018b, ApJ, 859, 146

Rupke, D. S., Veilleux, S., & Sanders, D. B. 2005, ApJS, 160, 115

Ryans, R. S. I., Keenan, F. R., Sembach, K. R., & Davies, R. D. 1997, Monthly Notices of the Royal Astronomical Society, 289, 83

S. Sutherland, R., & Dopita, M. 1993, Astrophysical Journal Supplement Series (ISSN 0067-0049), 88, 253

Sancisi, R., Fraternali, F., Oosterloo, T., & van der Hulst, T. 2008, A&A Rev., 15, 189

Saul, D. R., Peek, J. E. G., Grcevich, J., et al. 2012, ApJ, 758, 44

Savage, B. D., Kim, T.-S., Wakker, B. P., et al. 2014, ApJS, 212, 8

Savage, B. D., & Sembach, K. R. 1994, ApJ, 434, 145

Savage, B. D., Sembach, K. R., & Lu, L. 1997, AJ, 113, 2158

Savage, B. D., & Wakker, B. P. 2009, ApJ, 702, 1472

Savage, B. D., Sembach, K. R., Wakker, B. P., et al. 2003, ApJS, 146, 125

Schneider, E. E., Robertson, B. E., & Thompson, T. A. 2018, ApJ, 862, 56

Schönrich, R., & Dehnen, W. 2018, Monthly Notices of the Royal Astronomical Society, 478, 3809

Sembach, K. R., & Savage, B. D. 1992, ApJS, 83, 147

Sembach, K. R., Wakker, B. P., Savage, B. D., et al. 2003, ApJS, 146, 165

Shapiro, P. R., & Benjamin, R. A. 1991, PASP, 103, 923

Shapiro, P. R., & Field, G. B. 1976, ApJ, 205, 762

Shull, J., Jones, J., Danforth, C., & Collins, J. 2009, ApJ, 699, 754

Shull, J. M., & Slavin, J. D. 1994, ApJ, 427, 784

Sirko, E., Goodman, J., Knapp, G. R., et al. 2004, AJ, 127, 899

Slavin, J. D., Shull, J. M., & Begelman, M. C. 1993, ApJ, 407, 83

Smith, K., Bailer-Jones, C., Klement, R., & Xue, X. 2010, \aap, 522, A88

Smoker, J. V., Fox, A. J., & Keenan, F. P. 2011, Monthly Notices of the Royal Astronomical Society, 415, 1105

Smoker, J. V., Haffner, L. M., Keenan, F. P., Davies, R. D., & Pollacco, D. 2002, MNRAS, 337, 385

Snaith, O., Haywood, M., Di Matteo, P., et al. 2015, A&A, 578, A87

Snaith, O. N., Haywood, M., Di Matteo, P., et al. 2014, ApJ, 781, L31

Sommer-Larsen, J. 2006, ApJ, 644, L1

Sparre, M., Pfrommer, C., & Vogelsberger, M. 2019, MNRAS, 482, 5401

Spitzer, L. J. 1956, ApJ, 124, 20

Stanimirović, S., Hoffman, S., Heiles, C., et al. 2008, ApJ, 680, 276

Stanimirović, S., Putman, M., Heiles, C., et al. 2006, ApJ, 653, 1210

Steidel, C. C., & Sargent, W. L. W. 1992, ApJS, 80, 1

Stern, J., Hennawi, J. F., Prochaska, J. X., & Werk, J. K. 2016, ApJ, 830, 87

Stewart, K. R., Kaufmann, T., Bullock, J. S., et al. 2011, ApJ, 738, 39

Stocke, J. T., Keeney, B. A., Danforth, C. W., et al. 2017, ApJ, 838, 37

—. 2019, ApJS, 240, 15

Stocke, J. T., Keeney, B. A., Danforth, C. W., et al. 2013, ApJ, 763, 148

Stocke, J. T., Keeney, B. A., Danforth, C. W., et al. 2014, ApJ, 791, 128

Su, M., Slatyer, T. R., & Finkbeiner, D. P. 2010, ApJ, 724, 1044

Thom, C., Peek, J. E. G., Putman, M. E., et al. 2008, ApJ, 684, 364

Thom, C., Putman, M. E., Gibson, B. K., et al. 2006, ApJ, 638, L97

Tollerud, E. J., Boylan-Kolchin, M., Barton, E. J., Bullock, J. S., & Trinh, C. Q. 2011, ApJ, 738, 102

Tripp, T. M., Sembach, K. R., Bowen, D. V., et al. 2008, ApJS, 177, 39

Tumlinson, J., Peeples, M. S., & Werk, J. K. 2017, Annual Review of Astronomy and Astrophysics, 55, 389

Tumlinson, J., Thom, C., Werk, J., et al. 2011, Science, 334, 948

Tumlinson, J., Thom, C., Werk, J. K., et al. 2013, ApJ, 777, 59

Vallée, J. P. 2016, AJ, 151, 55

—. 2017, Astronomical Review, 13, 113

van Loon, J. T., Smith, K. T., McDonald, I., et al. 2009, MNRAS, 399, 195

van Woerden, H., Wakker, B. P., Schwarz, U. J., & de Boer, K. S., eds. 2005, High-Velocity Clouds (Dordrecht: Springer Netherlands), doi:10.1007/1-4020-2579-3

Vargas, C. J., Heald, G., Walterbos, R. A. M., et al. 2017, arXiv e-prints, arXiv:1703.09345

Vogt, S. S., & Donald Penrod, G. 1988, in Instrumentation for Ground-Based Optical Astronomy, ed. L. B. Robinson (Springer New York), 68–103

Vogt, S. S., Allen, S. L., Bigelow, B. C., et al. 1994, in Society of Photo-Optical Instrumentation Engineers (SPIE) Conference Series, Vol. 2198, Instrumentation in Astronomy VIII, ed. D. L. Crawford & E. R. Craine, 362

Voit, G. M. 2018, ApJ, 868, 102

—. 2019, ApJ, 880, 139

Wakker, B., & van Woerden, H. 1997, \araa, 35, 217

Wakker, B. P. 2001, ApJS, 136, 463

Wakker, B. P., Savage, B. D., Fox, A. J., Benjamin, R. A., & Shapiro, P. R. 2012, ApJ, 749, 157

Wakker, B. P., & van Woerden, H. 1991, Astronomy & Astrophysics, 250, 509

Wakker, B. P., York, D. G., Wilhelm, R., et al. 2008, ApJ, 672, 298

Wakker, B. P., York, D. G., Howk, J. C., et al. 2007, ApJ, 670, L113

Werk, J. K., Prochaska, J. X., Thom, C., et al. 2013, ApJS, 204, 17

Werk, J. K., Prochaska, J. X., Tumlinson, J., et al. 2014, ApJ, 792, 8

Werk, J. K., Prochaska, J. X., Cantalupo, S., et al. 2016, ApJ, 833, 54

Werk, J. K., Rubin, K. H., Bish, H. V., et al. 2019, arXiv e-prints, arXiv:1904.11014

Westmeier, T. 2018, \mnras, 474, 289

Wilde, M. C., Werk, J. K., Burchett, J. N., et al. 2021, ApJ, 912, 9

Winkel, B., Kerp, J., Flöer, L., et al. 2016, A&A, 585, A41

Wolf, C., Onken, C. A., Luvaul, L. C., et al. 2018, \pasa, 35, e010

Wolfire, M. G., McKee, C. F., Hollenbach, D., & Tielens, A. G. G. M. 1995, ApJ, 453, 673

Xue, X. X., Rix, H. W., Zhao, G., et al. 2008, ApJ, 684, 1143

Xue, X.-X., Rix, H.-W., Yanny, B., et al. 2011, ApJ, 738, 79

Yoon, J. H., & Putman, M. E. 2013, ApJ, 772, L29

Zabl, J., Bouché, N. F., Schroetter, I., et al. 2019, MNRAS, 485, 1961

Zhang, H., Zaritsky, D., Behroozi, P., & Werk, J. 2019, ApJ, 880, 28

Zheng, Y., Peek, J. E. G., Putman, M. E., & Werk, J. K. 2019, ApJ, 871, 35

Zheng, Y., Peek, J. E. G., Werk, J. K., & Putman, M. E. 2017, ApJ, 834, 179

Zheng, Y., Putman, M. E., Peek, J. E. G., & Joung, M. R. 2015, ApJ, 807, 103

Zheng, Y., Peeples, M. S., O'Shea, B. W., et al. 2020, ApJ, 896, 143